STUDIES OF SILICON PN JUNCTION SOLAR CELLS

By

A. Neugroschel and F. A. Lindholm
Principal Investigators
Department of Electrical Engineering
University of Florida
Gainesville, Florida 32611

FINAL TECHNICAL REPORT
covering the period September 1977 - December 1979

prepared for

National Aeronautics and Space Administration
NASA Lewis Research Center
NASA Grant NSG-3018

STUDIES OF SILICON PN JUNCTION SOLAR CELLS

By

A. Neugroschel and F. A. Lindholm
Principal Investigators
Department of Electrical Engineering
University of Florida
Gainesville, Florida 32611

FINAL TECHNICAL REPORT
covering the period September 1977 - December 1979

prepared for

National Aeronautics and Space Administration
NASA Lewis Research Center
NASA Grant NSG-3018

FORWARD

This report summarizes the results obtained in the research program at the University of Florida sponsored by NASA Lewis Research Center under Grant No. NSG-3018. The report covers the period of September 1977 - September 1979.

In addition to the senior investigators, graduate students S. C. Pao and M. A. Shibib participated in the research. The technical collaboration with M. P. Godlewski and W. H. Brandhorst, Jr., of NASA Lewis Research Center was very helpful during the research work. Discussions with C. T. Sah and J. G. Fossum also contributed to our research.

TABLE OF CONTENTS

CHAPTER 1

INTRODUCTION

The previous reports covering the period ending September 1977 concentrated on studies of basic mechanisms limiting the power conversion efficiency η, and particularly the open-circuit voltage V_{OC}, of n^+-p junction silicon solar cells. Both theoretical and experimental studies were done to determine which mechanisms are responsible for the discrepancy between the theoretical and experimental efficiencies and open-circuit voltages.

In the classical analysis of silicon p-n junction solar cells, which neglects certain fundamental physical mechanisms [1], the limit value of V_{OC} is calculated to be about 700 mV. The values of V_{OC} observed experimentally fall well below this limit value. The efficiency η of silicon solar cells will be limited by V_{OC}, as first noted by Brandhorst [2]. The conclusion from our experimental work [3,4] was that the factors which most influence V_{OC} are the dark recombination currents in the emitter and base regions of the solar cell. In particular, for cells with base resistivity of about 0.1 Ωcm, the emitter dark recombination current is dominant [3].

One of the possible mechanisms contributing to this dominance is bandgap narrowing ΔE_G [1] in heavily-doped regions of p-n junction solar cells. In our previous report we proposed a new method [5], based on the temperature dependence of the emitter current, for measuring ΔE_G in the emitter quasi neutral region as a function of the emitter doping concentration. Chapter 2 gives a detailed theoretical treatment underlying this method including now the effects of the Fermi-Dirac statistics. Experimental results for the emitter dark current density and ΔE_G for

emitter doping concentrations from 3 x $10^{19}cm^{-3}$ to 2 x $10^{20}cm^{-3}$ are given for n^+-type emitters. These data are the first accurate experimental results covering the range of dopings above $10^{19}cm^{-3}$.

To provide theoretical support for investigating different ways to obtain high open-circuit voltages in p-n junction silicon solar cells, in Chapter 3 an analytical treatment of heavily doped transparent-emitter devices is presented that includes the effects of bandgap narrowing, Fermi-Dirac statistics, a doping concentration gradient, and a finite surface recombination velocity S at the emitter surface [6]. Transparency of the emitter to minority carrier is defined by the condition that the transit time τ_t is much smaller than the minority carrier lifetime in the emitter τ_p, $\tau_t << \tau_p$. As part of the analytical treatment, a self-consistency test is formulated that checks the validity of the assumption of emitter transparency for any given device. The transparent-emitter model is applied to calculate the dependence of the open-circuit voltage V_{OC} of n^+-p junction silicon solar cells made on low-resistivity substrates. The calculated V_{OC} agrees with experimental values for high S_p ($\geq$ 5 x 10^4cm/s) provided the effects of bandgap narrowing (modified by Fermi-Dirac statistics) are included in the transparent-emitter model.

As was discussed earlier, the dark emitter recombination current has to be suppressed in order to achieve V_{OC} of about 700 mV. A new structure to achieve that goal, the high-low-emitter (HLE) solar cell was proposed [7,8]. The study of HLE devices was one of the main purposes of the research under this grant. A detailed report of our accomplishments is in Chapter 4. Chapter 4 deals specifically with the cell in which the high-low (H-L) junction is induced by a positive oxide charge in the silicon-dioxide layer covering the emitter surface [9]. The maximum V_{OC} achieved to date is 647 mV (measured by NASA Lewis in May 1979).

About 50 fabrication runs were made using different substrates and fabrication procedures. The most important results are summarized and described in detail. High values of V_{OC} in a range of 640-647 mV were obtained in at least 20 fabrication runs, repeatedly and reproducibly, using base substrate resistivities of 0.1 Ωcm and 0.025 Ωcm. The first devices, fabricated in January 1978, still maintain V_{OC} observed originally two years ago.

Chapter 5 discusses new methods for the determination of lifetimes and recombination currents in p-n junction solar cells and diodes [10]. These methods are particularly applicable to devices in which the minority carrier diffusion length is longer than the width of the region of the interest (HLE, BSF, IBC, FSF, and TJ cells). These methods are then directly applicable to determine the lifetime in the epitaxial emitter of the HLE cells described in Chapter 4. Once the lifetime is determined, this result allows determination of the dark recombination current in the emitter and also leads to the determination of the effective surface recombination velocity S_{eff} at the n^+-n H-L junction in the emitter.

Chapter 6 discusses a new approach for the fabrication of BSF cells [11], in which the heavily doped region in the base of a BSF cell is eliminated. Instead, the desired high concentration of majority carriers at the back surface is obtained by a biased metal-oxide-semiconductor structure (MOS-BSF cell).

Chapter 7 deals with design proposals for high efficiency high-low-emitter solar cells [12]. A first-order analysis of HLE cells is presented for both beginning-of-life (BOL) and end-of-life (EOL) conditions. Based on this analysis and on experimentally observed values for material parameters, we present design approaches for both space and terrestrial cells.

The approaches result in specification of doping levels, junction depths and surface conditions. The proposed structures are projected to have both high V_{OC} and high J_{SC}, and consequently high η.

REFERENCES FOR CHAPTER 1

1. F. A. Lindholm and C. T. Sah, IEEE Trans. Electron Devices, ED-24, 299 (1977).

2. H. W. Brandhorst, Jr., Record of 9th Photovoltaic Specialists Conf., 1 (1972).

3. F. A. Lindholm, A. Neugroschel, C. T. Sah, M. P. Godlewski, and H. W. Brandhorst, Jr., IEEE Trans. Electron Devices, ED-24, 402 (1977).

4. A. Neugroschel, F. A. Lindholm, and C. T. Sah, IEEE Trans. Electron Devices, ED-24, 662 (1977).

5. A. Neugroschel, P. J. Chen, S. C. Pao, and F. A. Lindholm, 13th Photovoltaic Specialists Conf. (1978).

6. M. A. Shibib, F. A. Lindholm, and F. Therez, IEEE Trans. Electron Devices, ED-26, 959 (1979).

7. C. T. Sah, F. A. Lindholm, and J. G. Fossum, IEEE Trans. Electron Devices, ED-25, 66 (1978).

8. F. A. Lindholm, A. Neugroschel, S. C. Pao, and J. G. Fossum, Record of 13th Photovoltaic Specialists Conf., 1300 (1978).

9. A. Neugroschel, S. C. Pao, F. A. Lindholm, and J. G. Fossum, Appl. Phys. Letts., 168 (1978).

10. A. Neugroschel, Record of 14th Photovoltaic Specialists Conf. (1980); submitted for publication in IEEE Trans. Electron Devices.

11. A. Neugroschel, "MOS and oxide-charge-induced (OCI) BSF solar cells", IEEE Trans. Electron Devices (1980).

12. A. Neugroschel and F. A. Lindholm, NASA Solar Cell High Efficiency and Radiation Damage Conf., Cleveland (1979).

CHAPTER 2

EXPERIMENTAL DETERMINATION OF BANDGAP NARROWING IN THE EMITTER REGION OF SILICON P-N JUNCTION DEVICES

2.1 Introduction

Bandgap narrowing in heavily-doped regions of silicon p-n junction devices has been the subject of several publications [2,6-12]. The degradation in open-circuit voltage in low resistivity p-n junction solar cells [2] and the low values of emitter efficiency observed in silicon bipolar transistors [8,9] have been attributed, in part, to the excessive minority carriers stored in the heavily-doped emitter region as a result of bandgap narrowing in that region.

Recently several methods have been proposed to determine the magnitude of bandgap narrowing ΔE_G in the base region of bipolar transistors. These methods employ measurements of the temperature dependence of the transistor emitter-base junction voltage, at a fixed collector current [6], and of the transistor collector current [7,13]. Because the base doping concentration of transistors is limited to about 10^{19} cm^{-3}, these methods do not allow investigation of an entire range of high doping densities up to about 10^{21} cm^{-3}. The higher levels of doping concentration are often present in the emitter region of conventional p-n junction solar cells and bipolar transistors and can significantly influence the device performance.

To determine ΔE_G of the emitter, we propose an alternative method which makes use of the temperature-dependence measurement of the

injected minority-carrier current in the emitter region. This method applies over the entire range of emitter doping concentration present in p-n junction devices and allows, for the first time, determination of ΔE_G as a function of doping concentration up to about 10^{21} cm^{-3}.

In the context of this dissertation, we assume that the classical parabolic quantum density of state description is adequate for both carriers (rigid-band approximation) and that the minority carriers obey the traditional macroscopic flow equation in uniformly-doped regions. Discussions related to these subjects can be found in literature [14-20]. In the interpretations of experimental results, we have taken into account the effects of Fermi-Dirac statistics, which decrease the minority-carrier concentration below the values predicted if Boltzmann statistics are used.

2.2 Theoretical Grounds for the Method

2.2.1 Injected Minority-Carrier Current in Heavily-Doped Emitter Region

We consider the structure shown in Fig. 2.1. For simplicity of discussion, we assume the quasi-neutral emitter region ($0 \leq x \leq W_E$) to be uniformly doped with donor concentration N_{DD}. Devices with an uniformly-doped emitter region allow direct correlation between the measured value of bandgap narrowing and the doping concentration without complications arising from the built-in electric field and quasi-field [18] associated with a position-dependent doping profile. We further assume the emitter to be transparent to the minority holes; that is, the hole transit time τ_t across the n^+ region is assumed to be much shorter than the hole recombination lifetime τ_p in the n^+ region. A

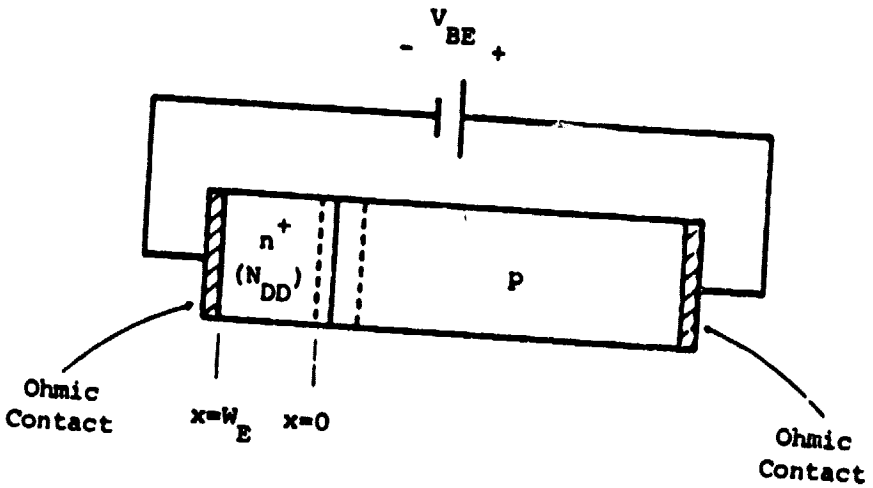

Figure 2.1 A diode structure under external bias V_{BE}.

thin emitter with large surface recombination velocity helps to decrease the hole transit time. Experiments with p^+-n-n^+ back-surface-field solar cells indicate that even some n^+ layers as thick as 1 μm (formed by phosphorous diffusion at 1000°C for 30 min) exhibit transparency properties [21].

Under the above assumptions, the injected hole current density J_p is spatially constant:

$$|J_p| = qD_p \frac{d\Delta P(x)}{dx} = qD_p \, \Delta P(0)/W_E \tag{2.1}$$

where D_p is the hole diffusivity, W_E is the width of the quasi-neutral emitter region, and $\Delta P(0)$ is the excess hole density at the edge of the quasi-neutral emitter, which we next discuss.

2.2.2 Excess Minority-Carrier Concentration in Degenerate Silicon

In thermal equilibrium, for a parabolic quantum density of states, the concentrations of charge carriers in a semiconductor are given by

$$N_0 = N_C \, F_{\frac{1}{2}}(\eta_c) = 2(2\pi m^*_{dn} kT/h^2)^{3/2} \, F_{\frac{1}{2}}(\eta_c) \tag{2.2}$$

$$P_0 = N_V \, F_{\frac{1}{2}}(\eta_v) = 2(2\pi m^*_{dh} kT/h^2)^{3/2} \, F_{\frac{1}{2}}(\eta_v) \tag{2.3}$$

where N_C and N_V are the effective density of states in the conduction and valence bands respectively, m^*_{dn} and m^*_{dh} are the density-of-state effective masses for electrons and holes respectively, $F_{\frac{1}{2}}$ is the Fermi-Dirac integral of order ½, and

$$\eta_c = (E_f - E_c)/kT \tag{2.4}$$

$$\eta_v = (E_v - E_f)/kT \tag{2.5}$$

For an n-type region, independent of the doping concentration, equation (2.3), which describes the minority hole concentration, reduces to the familiar form given by Boltzmann's statistics:

$$P_0 = N_V \exp[(E_V - E_f)/kT] \quad . \tag{2.6}$$

If we use the analytic approximation for $F_{\frac{1}{2}}(\eta)$ [18],

$$F_{\frac{1}{2}}(\eta) \approx \frac{e^{\eta}}{1 + C(\eta)e^{\eta}} \quad , \tag{2.7}$$

where $C(\eta)$ is a function of η given in reference [22], then the thermal equilibrium value of PN product is

$$P_0 N_0 = \frac{N_C N_V \, e^{\eta_c} \, e^{\eta_v}}{1 + C(\eta_c)e^{\eta_c}} \quad . \tag{2.8}$$

When an external bias is applied to the structure shown in Fig. 2.1, the hole quasi-Fermi level in the n^+ region shifts from its equilibrium value. The electron quasi-Fermi level, however, remains fixed relative to the conduction band as given by the relation

$$N_{DD} = N = \frac{N_C \, e^{\eta_c}}{1 + C(\eta_c)e^{\eta_c}} \tag{2.9}$$

where we assume for doping concentrations above 2×10^{18} cm^{-3} all impurity atoms are ionized [23,24]. Thus we have

$$N_{DD}P(x) = \frac{N_C N_V \, e^{-(E_C - E_V)/kT} \, e^{[E_{fn} - E_{fp}(x)]/kT}}{1 + C(\eta_c)e^{\eta_c}} \quad , \tag{2.10}$$

and, at x=0,

$$P(0) = \frac{N_C N_V e^{-E_G/kT} e^{qV_{BE}/kT}}{N_{DD}[1 + C(\eta_c)e^{\eta_c}]} \tag{2.11}$$

where E_{fn} and E_{fp} are the electron and hole quasi-Fermi levels, respectively, V_{BE} is the external voltage bias, and E_G is the energy bandgap, which for lightly doped silicon is [25,26]

$$E_G = E_{G0} - \alpha T$$

$$= 1.206 - 2.8\text{x}10^{-4}\ T \quad \text{eV} \quad \text{for } 300\ \text{K} < T < 400\ \text{K} \quad . \tag{2.12}$$

Here E_{G0} is the extrapolated energy bandgap at 0 K which differs from the actual energy bandgap value of 1.170 eV at 0 K due to the parabolic dependence of the energy bandgap on temperature at lower temperatures [27]. The experimental uncertainty in (2.12) is about ±0.0015 eV [25].

Combining (2.11), (2.12), and using the equilibrium value of P_0 in (2.8), we obtain the excess hole concentration

$$\Delta P(0) = \frac{N_C N_V e^{\alpha/k} e^{-E_{G0}/kT} [e^{qV_{BE}/kT} - 1]}{N_{DD}[1 + C(\eta_c)e^{\eta_c}]}$$

$$\triangleq \frac{n_i^2 [e^{qV_{BE}/kT} - 1]}{N_{DD}[1 + C(\eta_c)e^{\eta_c}]} \tag{2.13}$$

where n_i^2 is defined to be the intrinsic carrier concentration squared corresponding to energy bandgap E_{G0}. The usefulness of the analytic approximation for $F_{\frac{1}{2}}$ is obvious. It allows direct assessment of the effects of

carrier degeneracy on the minority carrier storage and therefore on the recombination current in the heavily-doped region. Specifically, the effect of Fermi-Dirac statistics decreases the minority carrier concentration by a factor of $[1 + C(\eta_c)\exp(\eta_c)]$ below that resulting if Boltzmann statistics were used. In Table 2.1 and also in Figure 2.2, we display numerical results of the reciprocal of this quantity as a function of temperature for several doping concentrations. It is noted that the hole concentration is depressed by as much as 70% at 300 K in an n-type region with $N_{DD}=10^{20}$ cm^{-3} as a result of electron degeneracy. The value of effective density of states in the conduction band [28] used in these calculations is $N_C = 2.88 \times 10^{19} (T/300)^{3/2}$. For $\eta \leq 4$, $F_{\frac{1}{2}}(\eta)$ in (2.7) can be approximated by $\exp(\eta)/[1 + (0.3-0.0413\eta)\exp(\eta)]$ to within 4% [18].

2.2.3 Temperature Dependence of Injected Minority-Carrier Current in Heavily-Doped Emitter Region

The expression for the injected minority-carrier current in a heavily-doped thin region can be obtained by combining (2.1) and (2.13)

$$|J_p| = \frac{qD_p n_i^2 [e^{qV_{BE}/kT} - 1]}{N_{DD}[1 + C(\eta_c)e^{\eta_c}]W_E} \quad . \tag{2.14}$$

If we use Einstein's relation between carrier diffusivity and mobility for the minority holes, $D_p=(kT/q)\mu_p$, and assume the hole mobility to be independent of temperature in the degenerate material [23], the hole saturation current then varies with temperature as

$$|J_{p0}| \propto T^4 \exp(-E_{G0}/kT)/[1+C(\eta_c)\exp(\eta_c)] \quad . \tag{2.15}$$

Table 2.1 Numerical Result of η_c and $[1+C(\eta_c)\exp(\eta_c)]^{-1}$ as a Function of Temperature for Several Donor Doping Concentrations (η_c is obtained by solving eq. 2.9).

	$N_{DD}=3\times10^{19}$ cm^{-3}		$N_{DD}=1\times10^{20}$ cm^{-3}		$N_{DD}=1.5\times10^{20}$ cm^{-3}		$N_{DD}=2.1\times10^{20}$ cm^{-3}	
T(K)	η_c	$f(\eta_c)=[1+C(\eta_c)e^{\eta_c}]^{-1}$	η_c	$f(\eta_c)$	η_c	$f(\eta_c)$	η_c	$f(\eta_c)$
300	0.392	0.704	2.428	0.306	3.417	0.171	4.279	0.101
320	0.263	0.727	2.218	0.343	3.165	0.200	4.034	0.117
340	0.146	0.747	2.030	0.378	2.938	0.229	3.799	0.135
360	0.0372	0.763	1.861	0.411	2.731	0.258	3.576	0.155
380	-0.0650	0.780	1.709	0.441	2.542	0.288	3.366	0.177
400	-0.158	0.792	1.569	0.470	2.370	0.316	3.169	0.199

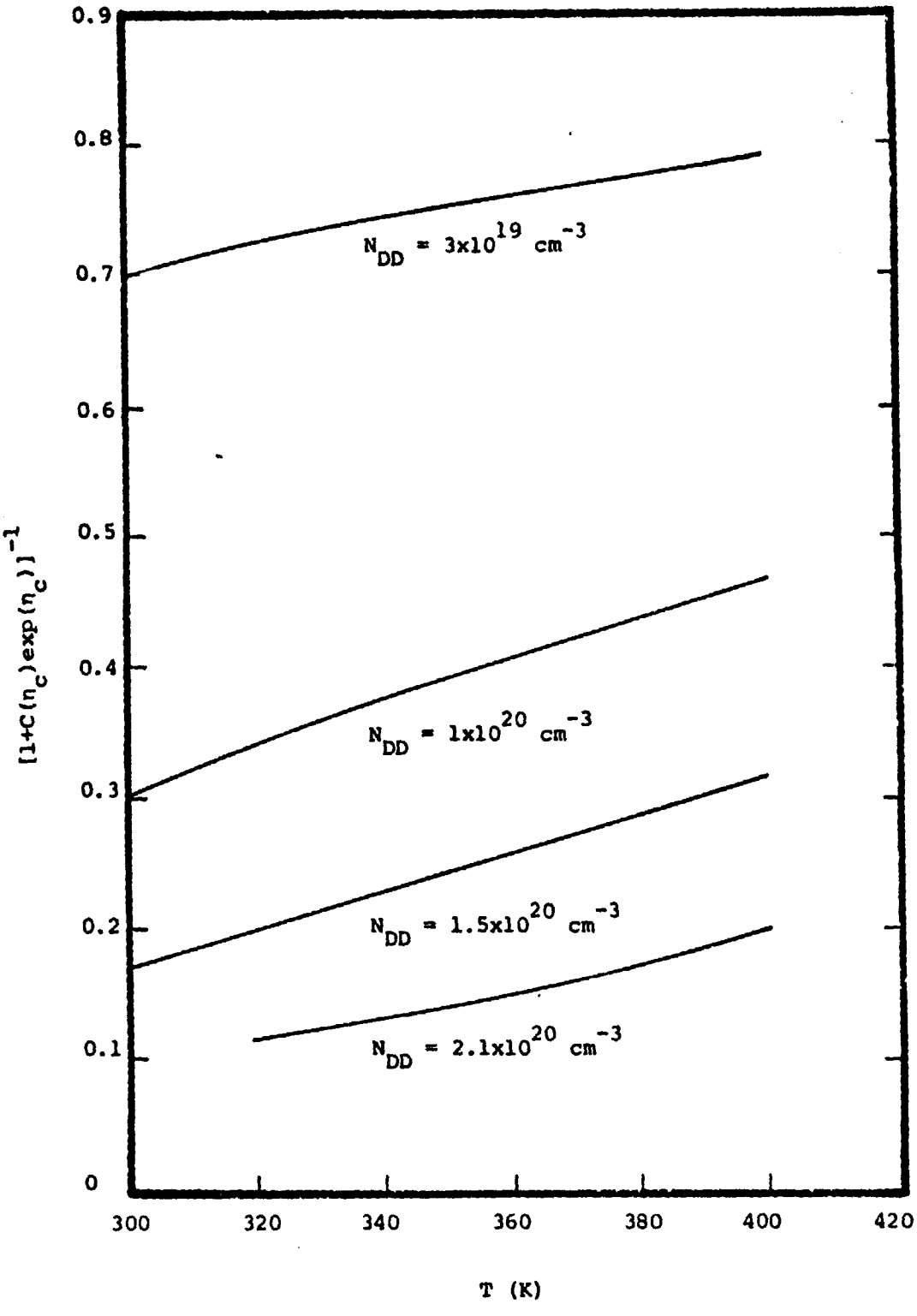

Figure 2.2 Ratio of minority carrier concentration with consideration of Fermi-Dirac statistics to the same quantity without consideration of Fermi-Dirac statistics.

The value of E_{G0} in units of eV is then equal to the slope of the plot $\ln\{J_{P0}[1+C(\eta_c)\exp(\eta_c)/T^4\}$ versus q/kT. Values of E_{G0} smaller than 1.206 eV correspond to an increase of minority-carrier concentration not accountable by traditional theory and we attribute this phenomenon as a consequence of an effective reduction in the energy bandgap. Thus we define

$$\Delta E_G = 1.206 - E_{G0}(\text{measured}) \quad \text{eV} \quad . \tag{2.16}$$

To incorporate the effect of bandgap narrowing, we re-write from (2.14) the expression for the emitter saturation current

$$|J_{P0}| = \frac{qD_P n_{io}^2 \exp(\Delta E_G/kT)}{N_{DD}[1 + C(\eta_c)e^{\eta_c}]W_E} \quad . \tag{2.17}$$

where n_{io}^2 is the intrinsic density squared corresponding to E_{G0} = 1.206 eV.

2.3 Illustration of the Method

In this section we illustrate the above method with two device structures: a transistor structure and a diode structure.

The transistors under study are n-p-n silicon bipolar transistors. There are two transistors studied, which we will designate as SHF 70 and TXA. The n^+ emitter region of transistor SHF 70 is ion-implanted with a uniform arsenic concentration of 1.5×10^{20} cm^{-3}. The depth of the emitter-base junction from the silicon surface is about 0.37 μm. The net impurity profiles obtained by incremental sheet resistance measurement is shown in Fig. 2.3. The n^+ emitter region of transistor TXA is arsenic diffused with a near-uniform dopant concentration of 1.5×10^{20} cm^{-3}. The impurity profile is shown in Fig. 2.4.

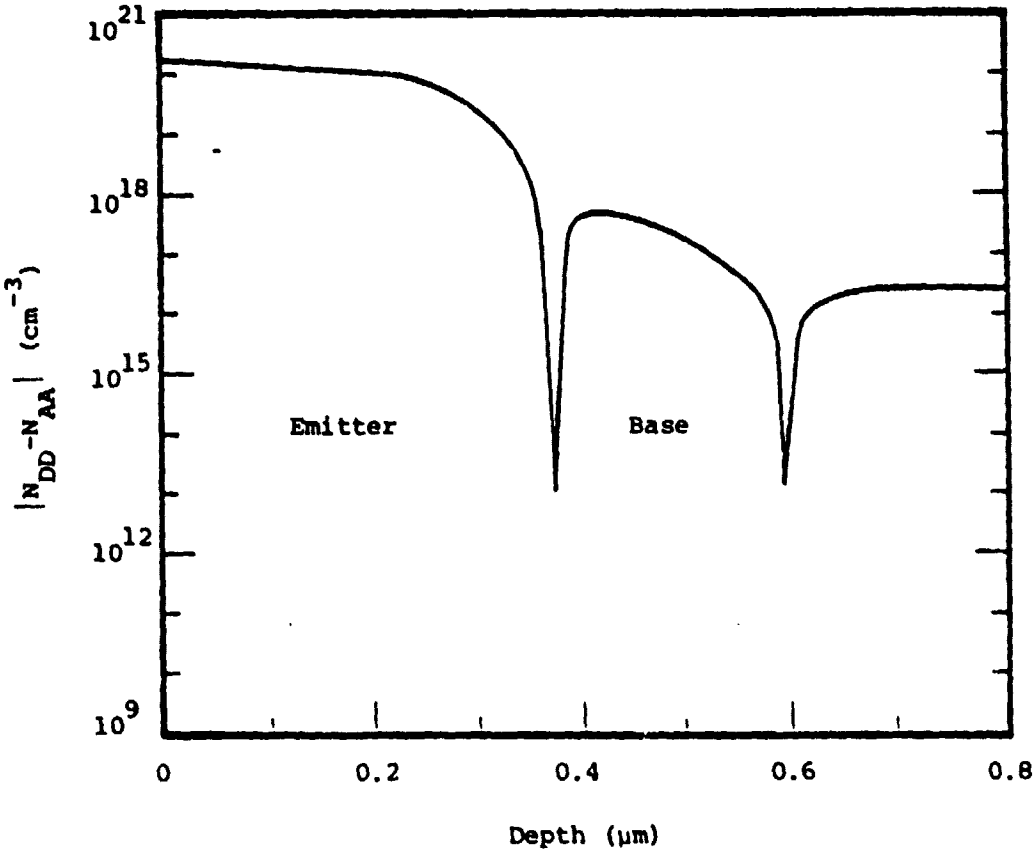

Figure 2.3 Impurity profile of transistor SHF 70 (n-p-n).

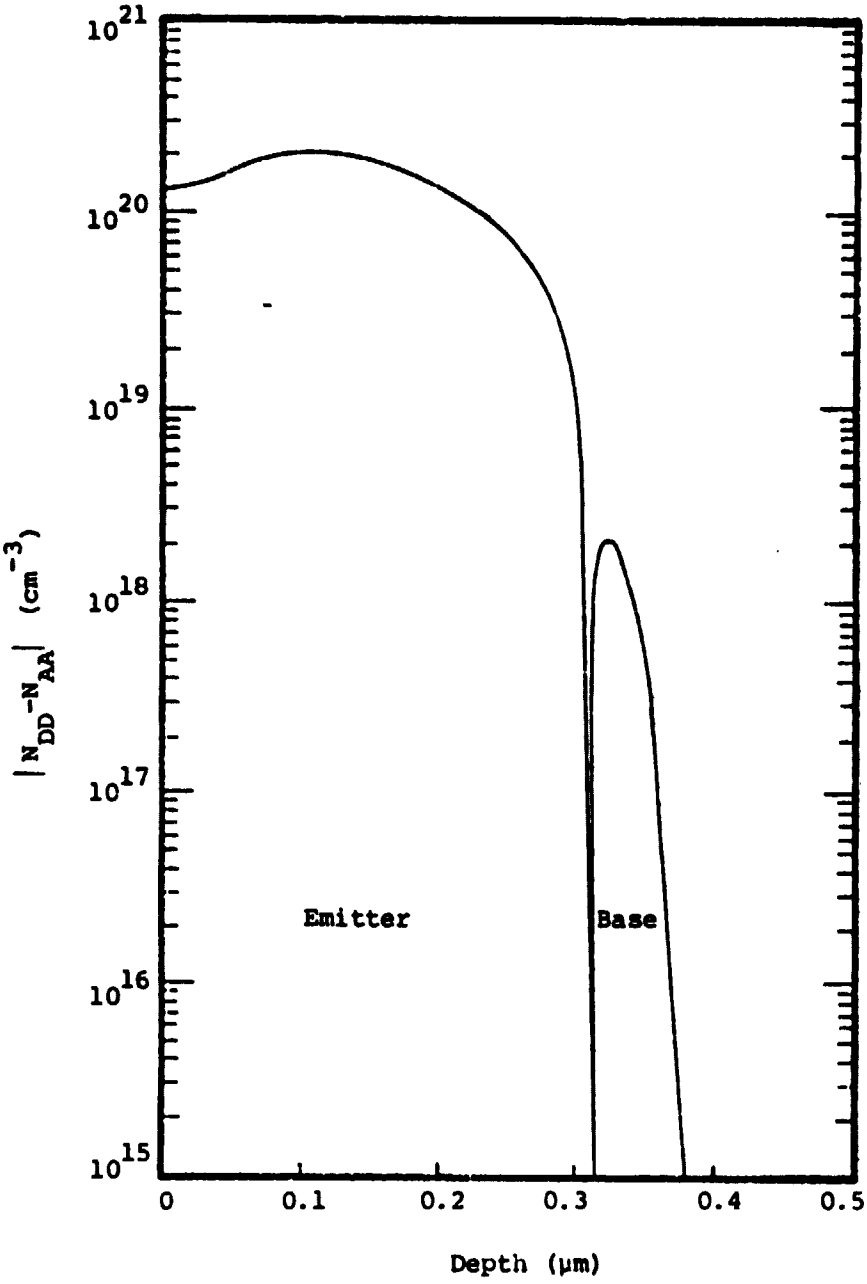

Figure 2.4 Impurity profile of transistor TXA (n-p-n).

A convenient way to study the injected minority-carrier current in the heavily-doped emitter region would be by measuring the transistor base current I_B as a function of the forward biased emitter-base junction voltage V_{BE} as shown in Fig. 2.5. However, the transistor base current consists not only of the injected minority hole current (in a n-p-n transistor) supporting recombination in the quasi-neutral bulk region and the surface of the emitter; it also has a component of current supporting bulk recombination in the quasi-neutral base region and a component of current supporting recombination in the emitter-base junction space-charge region [29]. We have already discussed the recombination current in the thin heavily-doped emitter in Section 2.2.1 and 2.2.2. The bulk recombination current in the base region is often negligible; indeed if this were the only component of the transistor base current, the static common-emitter current gain h_{FE} of conventional silicon bipolar transistors would be several orders of magnitude higher than the values of h_{FE} commonly seen ($\sim 10^2$). The transistors under study have values of h_{FE} less than 100. The component of current due to recombination in the emitter-base junction space-charge region prevails at lower values of V_{BE}. This current component has a characteristic exponential dependence on voltage: $I \propto \exp(qV_{BE}/mkT)$ with $m > 1$ [3,4]. At higher biases, this current component is less significant due to the weaker exponential dependence on voltage but nevertheless still constitutes a portion of the total current. Thus, in order to obtain the emitter recombination current, which has an ideal exponential voltage dependence ($m = 1$), the space-charge region recombination current must be subtracted from the total measured terminal current [4,8]. A computer program written to analyze data resulting from the transistor

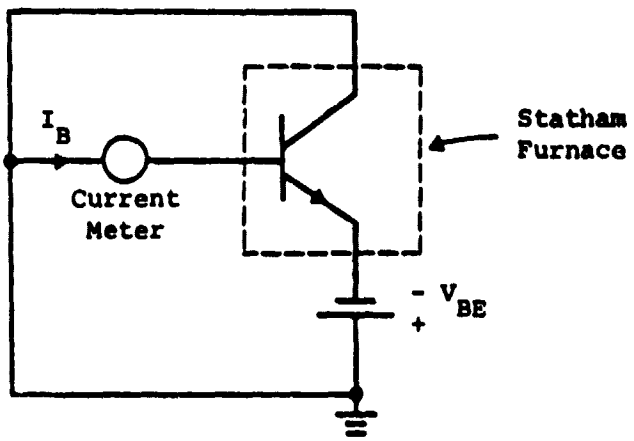

Figure 2.5 Circuit diagram for transistor base current measurement.

base current measurements is listed in Appendix I. A typical I_B versus V_{BE} plot for transistor SHF 70 is shown in Fig. 2.6. In Tables 2.2 and 2.3, we summarize the values of emitter saturation current I_{E0} determined for several temperatures for the two transistors under study. The values of η_c and $I_{E0}[1+C(\eta_c)\exp(\eta_c)]/T^4$ are also tabulated in Tables 2.2 and 2.3. In Fig. 2.7, $\ln\{I_{E0}[1+C(\eta_c)\exp(\eta_c)]/T^4\}$ versus 1000/T is plotted. E_{G0} in units of eV can be obtained by multiplying the magnitude of the slope of the least-square-fitted straight line by 1000k/q. For transistor SHF 70, E_{G0} is found to be 0.981 eV. This corresponds to a bandgap narrowing ΔE_G of 0.225 eV. For transistor TXA, ΔE_G is found to be 0.227 eV.

We have also studied bandgap narrowing in heavily-doped n^+ regions using diode structures. The starting material is boron-doped p-type silicon wafers with doping concentration of 2.0×10^{17} cm^{-3}. The wafers are cleaned and oxidized at 800°C for two hours in dry oxygen to grow 200 Å of silicon dioxide. The wafers are then implanted with different arsenic doses and annealed at 1050°C for 20 min. in dry nitrogen. The thin oxide on both surfaces of the wafers is removed and the wafers are metallized with Ti-Ag on both surfaces. Square chips of 110 mil x 110 mil are scribed from the wafers and circular mesa structures of different areas are made on the chips as shown in Fig. 2.8. The devices are mounted on TO-5 headers with silver epoxy at room temperature and ultrasonically wire-bonded at room temperature.

The measurement circuit for the diode I-V characteristic is shown in Fig. 2.9. The current source used is an EDC-CR 103 current standard. The current is incremented such that the terminal voltages across the diode are 10 mV apart for each reading, starting from 0.1 V to 0.7 V.

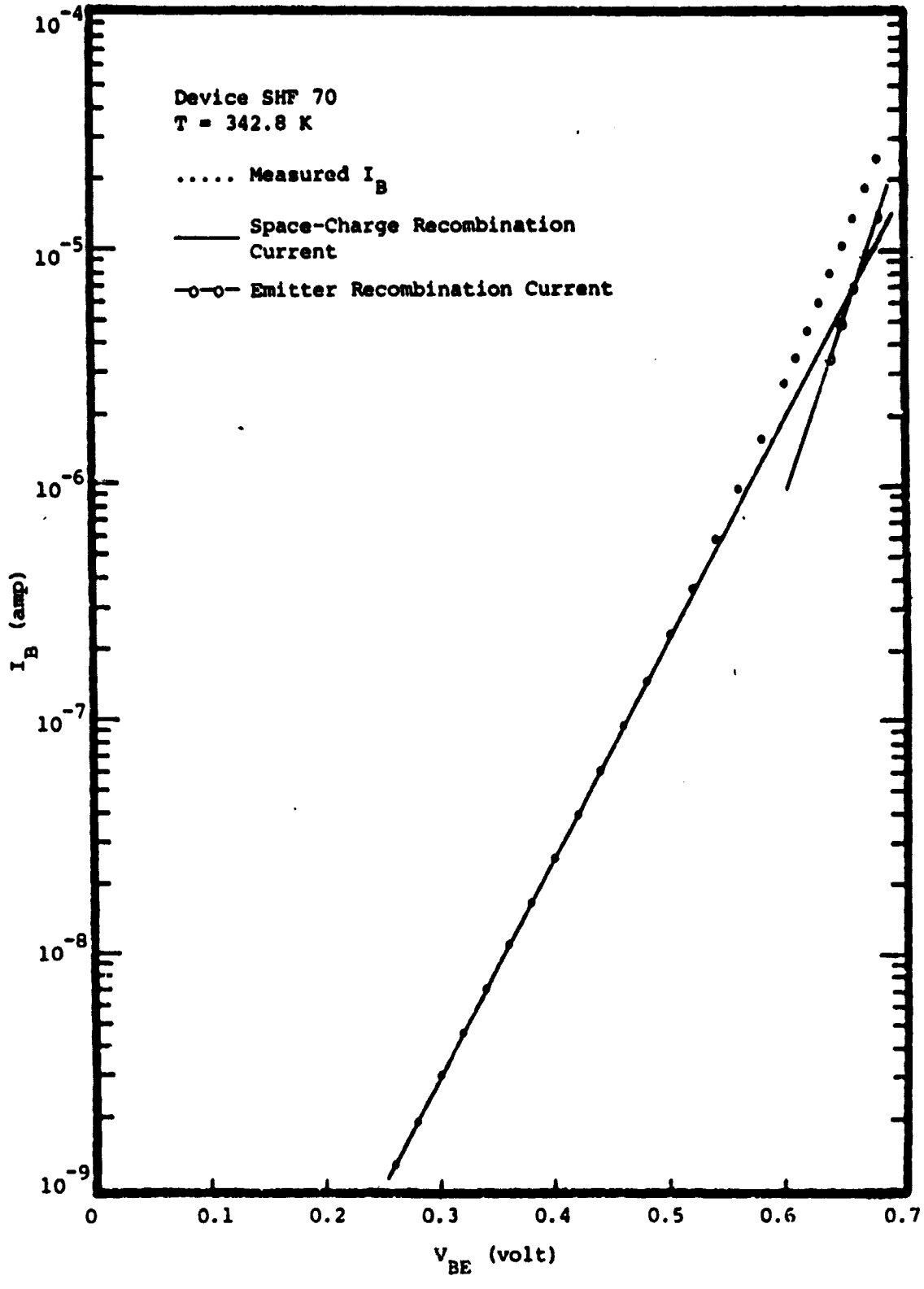

Figure 2.6 I_B vs. V_{BE} plot for transistor SHF 70 at 342.8 K.

Table 2.2 Experimental Values of Emitter Saturation Current I_{E0} and Calculated Values of η_c at Different Temperatures for Transistor SHF 70 ($N_{DD} = 1.5 \times 10^{20}$ cm^{-3}).

T(K)	I_{E0} (amp)	η_c	$I_{E0}[1+C(\eta_c)e^{\eta_c}]/T^4$
317 2	5.67×10^{-17}	3.198	2.86×10^{-26}
322.2	1.11×10^{-16}	3.139	5.08×10^{-26}
327.3	2.12×10^{-16}	3.080	8.79×10^{-26}
332.4	3.93×10^{-16}	3.022	1.48×10^{-25}
337.3	7.17×10^{-16}	2.968	2.47×10^{-25}
342.8	1.36×10^{-15}	2.908	4.23×10^{-25}
348.0	2.44×10^{-15}	2.854	6.93×10^{-25}
353.4	4.51×10^{-15}	2.798	1.17×10^{-24}
358.5	7.66×10^{-15}	2.745	1.81×10^{-24}
363.4	1.26×10^{-14}	2.697	2.74×10^{-24}
368.6	2.09×10^{-14}	2.647	4.18×10^{-24}
373.6	3.61×10^{-14}	2.601	6.66×10^{-24}

Table 2.3 Experimental Values of Emitter Saturation Current I_{E0} and Calculated Values of η_c at Different Temperatures for Transistor TXA ($N_{DD} = 1.5 \times 10^{20}$ cm^{-3}).

T(K)	I_{E0} (amp)	η_c	$I_{E0}[1+C(\eta_c)e^{\eta_c}]/T^4$
318.6	5.23×10^{-16}	3.181	2.57×10^{-25}
327.2	1.56×10^{-15}	3.080	6.48×10^{-25}
337.5	5.55×10^{-15}	2.965	1.90×10^{-24}
348.0	1.83×10^{-14}	2.854	5.20×10^{-24}
358.2	5.57×10^{-14}	2.749	1.32×10^{-23}

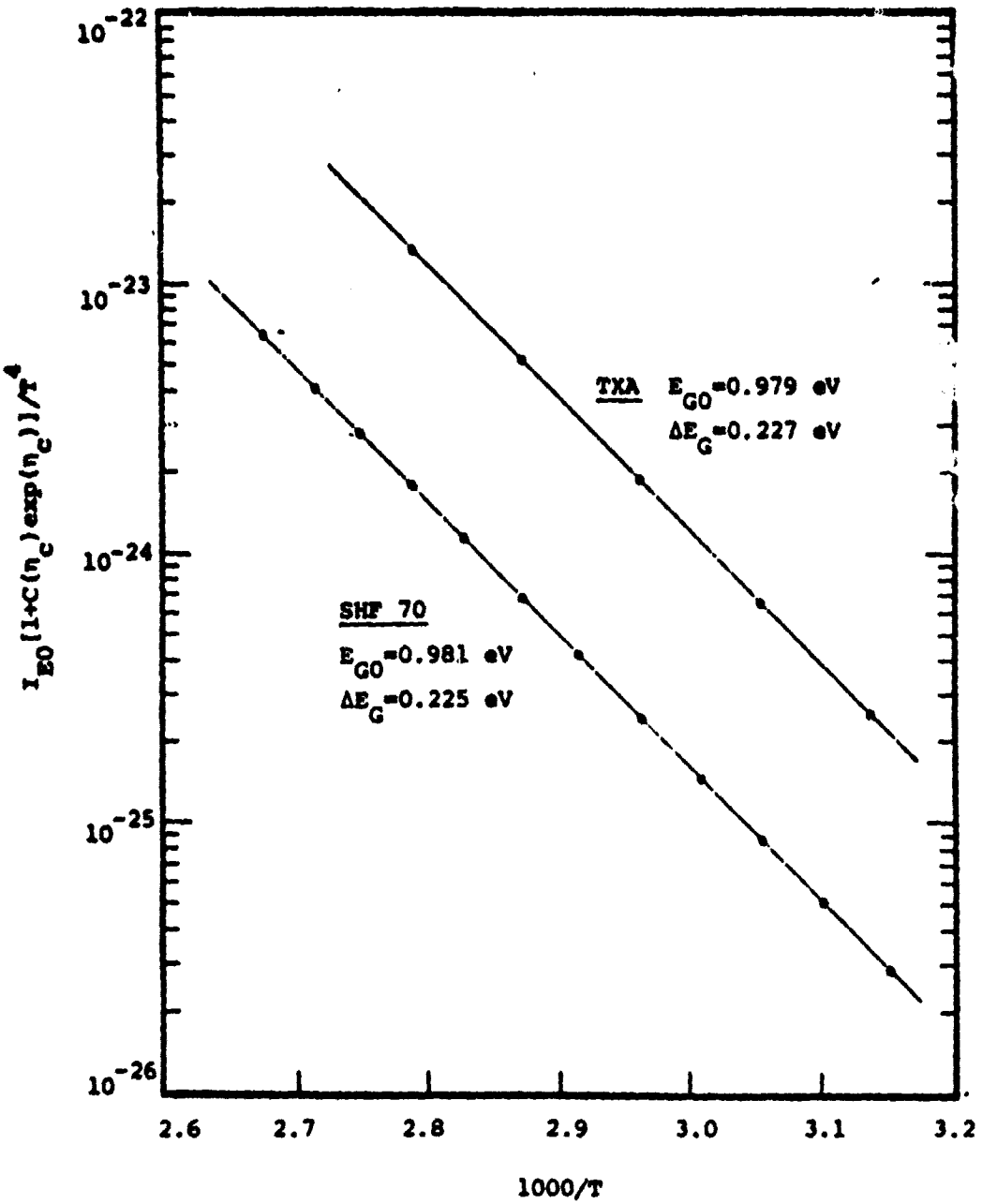

Figure 2.7 Plot of $\ln\{I_{EO}[1+C(n_c)\exp(n_c)]/T^4\}$ vs. 1000/T for transistor SHF 70 and TXA.

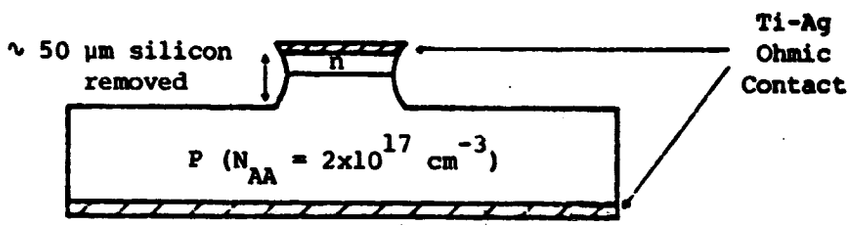

Figure 2.8 Mesa diode structure. The silicon etchant used is 1HF : 1CH_3COOH : 6HNO_3. Etching time is about 1 min.

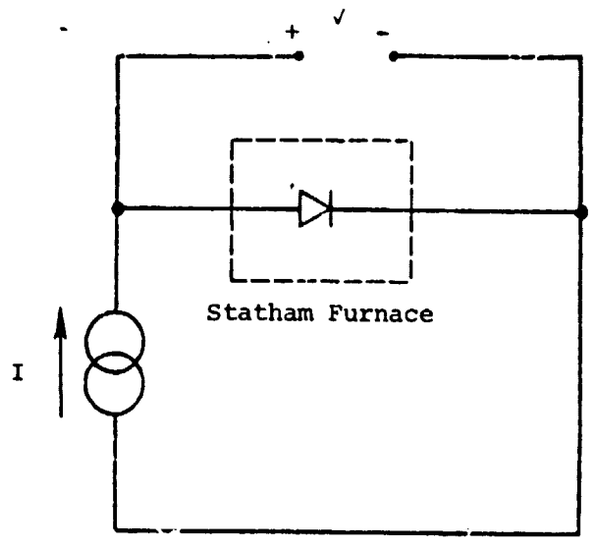

Figure 2.9 Circuit diagram for diode I-V characteristic measurement.

There are several groups of diodes under study, which we designate in Table 2.4. All these devices have shallow n^+ emitters with uniform doping concentrations. The impurity profile in the n^+ emitter region of these devices as measured by a spreading resistance method are shown in Fig. 2.10. A typical I-V characteristic of these devices is displayed in Fig. 2.11. All devices selected for measurements have an easily recognizable space-charge recombination current component at lower biases, that is, $I \propto \exp(qV/mkT)$ with $m > 1$ and m approximately constant for two orders of magnitude range of current. This allows straightforward extraction of the ideal recombination current component ($m = 1$) from the measured terminal current [4]. The computer program used to analyze the transistor current can be also used in this case (Appendix I). The pertinent geometrical and electrical parameters including minority carrier diffusion length in the substrate material measured by an X-ray irradiation method [30] for these devices are summarized in Table 2.4. The extracted values of saturation current I_{QN0} for the ideal recombination current component at different measurement temperatures are tabulated in Table 2.5a-2.5d.

In a diode structure, the ideal recombination current has two components: a component supporting recombination in the bulk region and surface of the emitter and a component supporting recombination in the bulk region and back contact of the base. For diffused p^+-n diodes fabricated on low-resistivity silicon, it has been demonstrated that the recombination current in the emitter region can be significant [4]. For the n^+-p diodes under study we expect the emitter recombination current to be even more significant, partly due to the thin emitter with large surface recombination velocity and partly due to a larger value

Table 2.4 Geometrical and Electrical Parameters of Arsenic-Implanted Diodes Under Study.

Device	Device Area (cm^2)	N_{DD} (cm^{-3})	Emitter-Base Junction Depth (μm)	N_{DD} (cm^{-3})	L_n (μm)
UF 2-2	2.29×10^{-2}	3.0×10^{19}	0.15	2.0×10^{17}	65
UF 3-2	1.06×10^{-2}	2.1×10^{20}	0.32	2.0×10^{17}	67
UF 8-2	9.90×10^{-3}	1.5×10^{20}	0.31	2.0×10^{17}	76
UF 12-2	1.37×10^{-2}	1.0×10^{20}	0.30	2.0×10^{17}	62

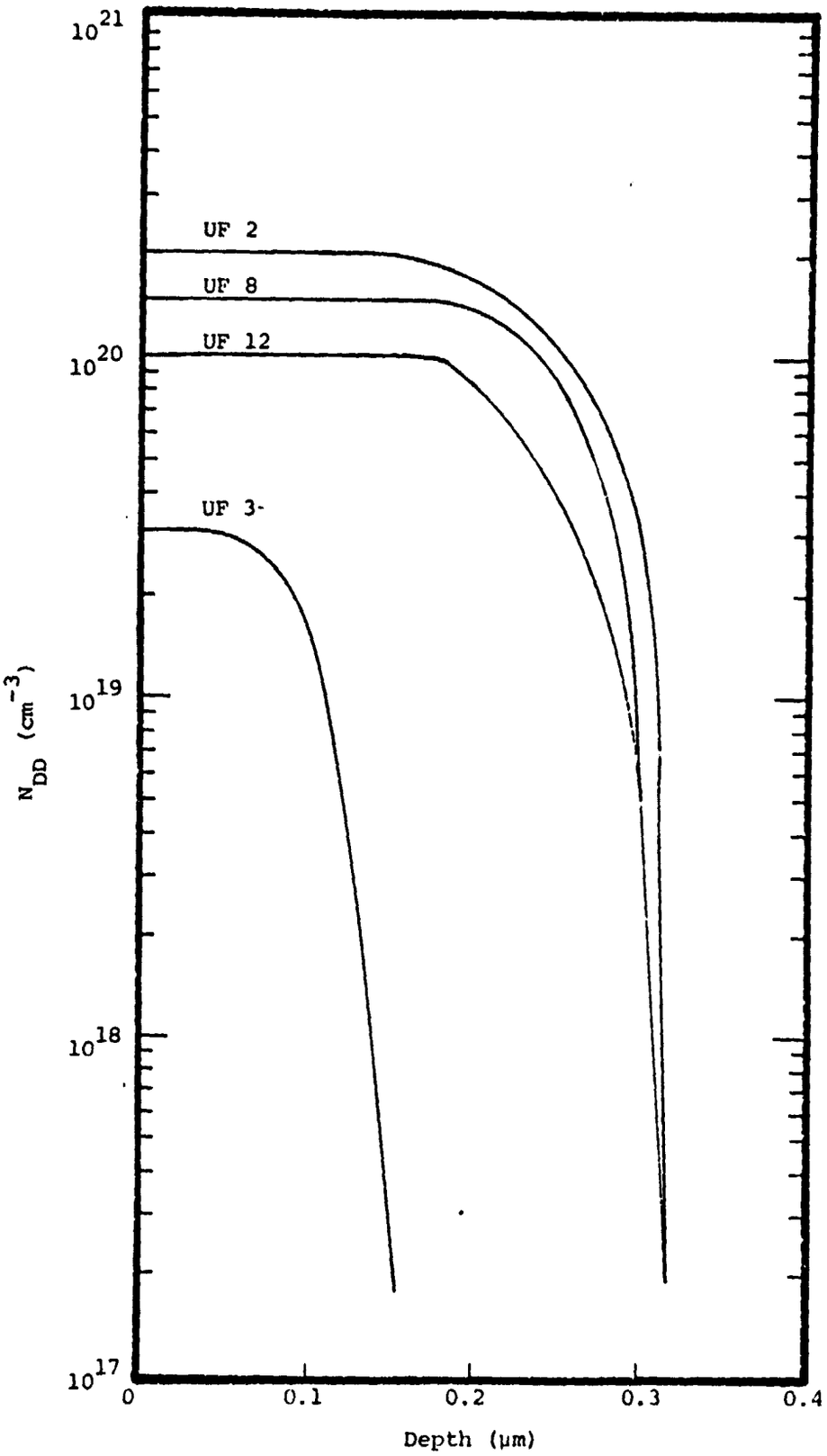

Figure 2.10 Impurity profile of the n^+ emitter region of the ion-implanted diodes under study.

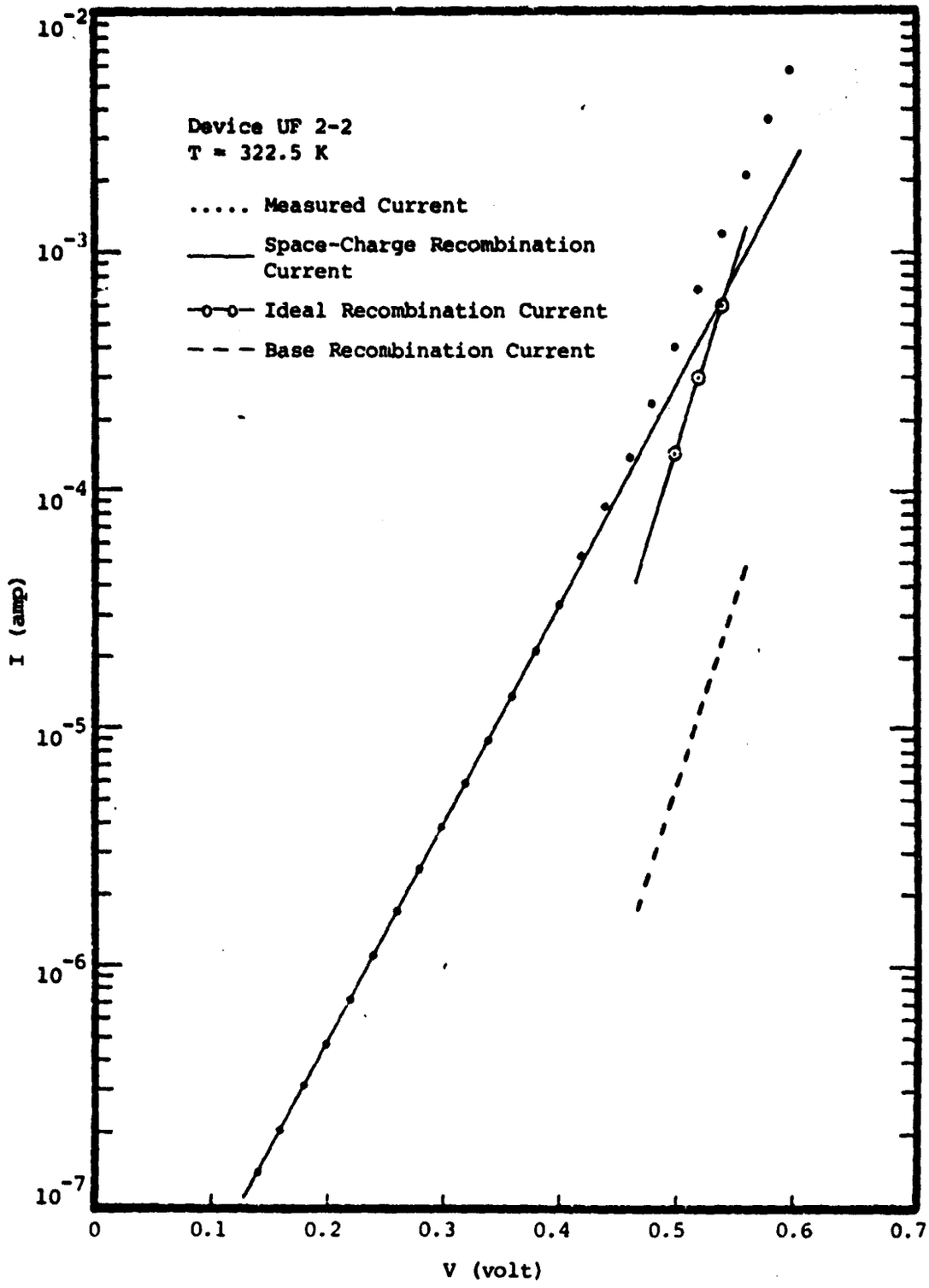

Figure 2.11 Typical I-V characteristic for group UF 2 diode (322.5 K).

Table 2.5a Ideal Saturation Current for Device UF 2-2 (N_{DD} = 3.0 x 10^{19} cm^{-3}).

T (K)	I_{QNO} (amp)	J_{QNO} (amp/cm^2)
322.5	2.23×10^{-12}	9.74×10^{-11}
327.3	4.05×10^{-12}	1.77×10^{-10}
332.3	7.47×10^{-12}	3.26×10^{-10}
337.5	1.42×10^{-11}	6.20×10^{-10}
342.6	2.63×10^{-11}	1.15×10^{-9}
347.8	4.70×10^{-11}	2.05×10^{-9}
353.6	8.60×10^{-11}	3.76×10^{-9}

Table 2.5b Ideal Saturation Current for Device UF 3-2 (N_{DD} = 2.1 x 10^{20} cm^{-3}).

T (K)	I_{QNO} (amp)	J_{QNO} (amp/cm^2)
322.3	3.90×10^{-13}	3.68×10^{-11}
327.3	7.56×10^{-13}	7.13×10^{-11}
337.5	2.57×10^{-12}	2.42×10^{-10}
342.9	4.85×10^{-12}	4.58×10^{-10}
347.9	8.45×10^{-12}	7.97×10^{-10}
358.7	2.58×10^{-11}	2.43×10^{-9}

Table 2.5c Ideal Saturation Current for Device UF 8-2 ($N_{DD} = 1.5 \times 10^{20}$ cm^{-3}).

T (K)	I_{QNO} (amp)	J_{QNO} (amp/cm^2)
322.2	5.66×10^{-13}	5.72×10^{-11}
327.2	1.08×10^{-12}	1.09×10^{-10}
332.3	2.00×10^{-12}	2.02×10^{-10}
337.5	3.67×10^{-12}	3.71×10^{-10}
342.6	6.77×10^{-12}	6.84×10^{-10}
348.1	1.23×10^{-11}	1.24×10^{-9}

Table 2.5d Ideal Saturation Current for Device UF 12-2 ($N_{DD} = 1.0 \times 10^{20}$ cm^{-3}).

T (K)	I_{QNO} (amp)	J_{QNO} (amp/cm^2)
332.5	1.76×10^{-12}	1.28×10^{-10}
337.5	3.11×10^{-12}	2.27×10^{-10}
342.6	5.76×10^{-12}	4.23×10^{-10}
348.1	1.08×10^{-11}	7.88×10^{-10}
353.7	1.99×10^{-11}	1.45×10^{-9}
358.5	3.30×10^{-11}	2.41×10^{-9}

of effective density of states in the conduction band for silicon in comparison with the value of effective density of states in the valence band. This expectation of large I_E is consistent with experimental findings [3] on diffused n^+-p solar cells having a 0.1 Ω-cm base resistivity. We will discuss this effect in the next section.

To illustrate that the emitter recombination current is the dominant current component in these diodes, we measure the minority carrier diffusion lengths in these devices using the X-ray irradiation method [30]. Consider device UF 2-2, for example. The extracted ideal recombination current I_{QNO} is shown in Fig. 2.11. The base recombination current component (dashed line) as calculated from $(qAn_{io}^2 D_n/N_{AA}L_n)$ x $[\exp(qV/kT)-1]$ is only a few percent of the total ideal recombination current. The emitter of the device is designed to be thin and with a large surface recombination velocity so that the dominant recombination process in the emitter is mainly at the emitter surface and therefore (2.15) and (2.17) apply. This requires the hole lifetime in the emitter region to be longer than the hole transit time across the emitter region, which we will discuss in further detail in the next section.

In Fig. 2.12, we display a plot of $\ln\{I_{EO}[1+C(\eta_c)\exp(\eta_c)]/T^4\}$ versus 1000/T for two devices having different values of ΔE_G. The values of ΔE_G determined for different values of arsenic concentration using the diode structure are summarized in Table 2.6. The values of ΔE_G obtained using the transistor structure are also included. In Fig. 2.13, we show the results graphically. The experimental values of ΔE_G as a function of impurity concentration N_{DD} can be fitted by

$$\Delta E_G = 0.037 \ln(N_{DD}/10^{20}) + 0.210 \quad \text{eV} \quad . \qquad (2.18)$$

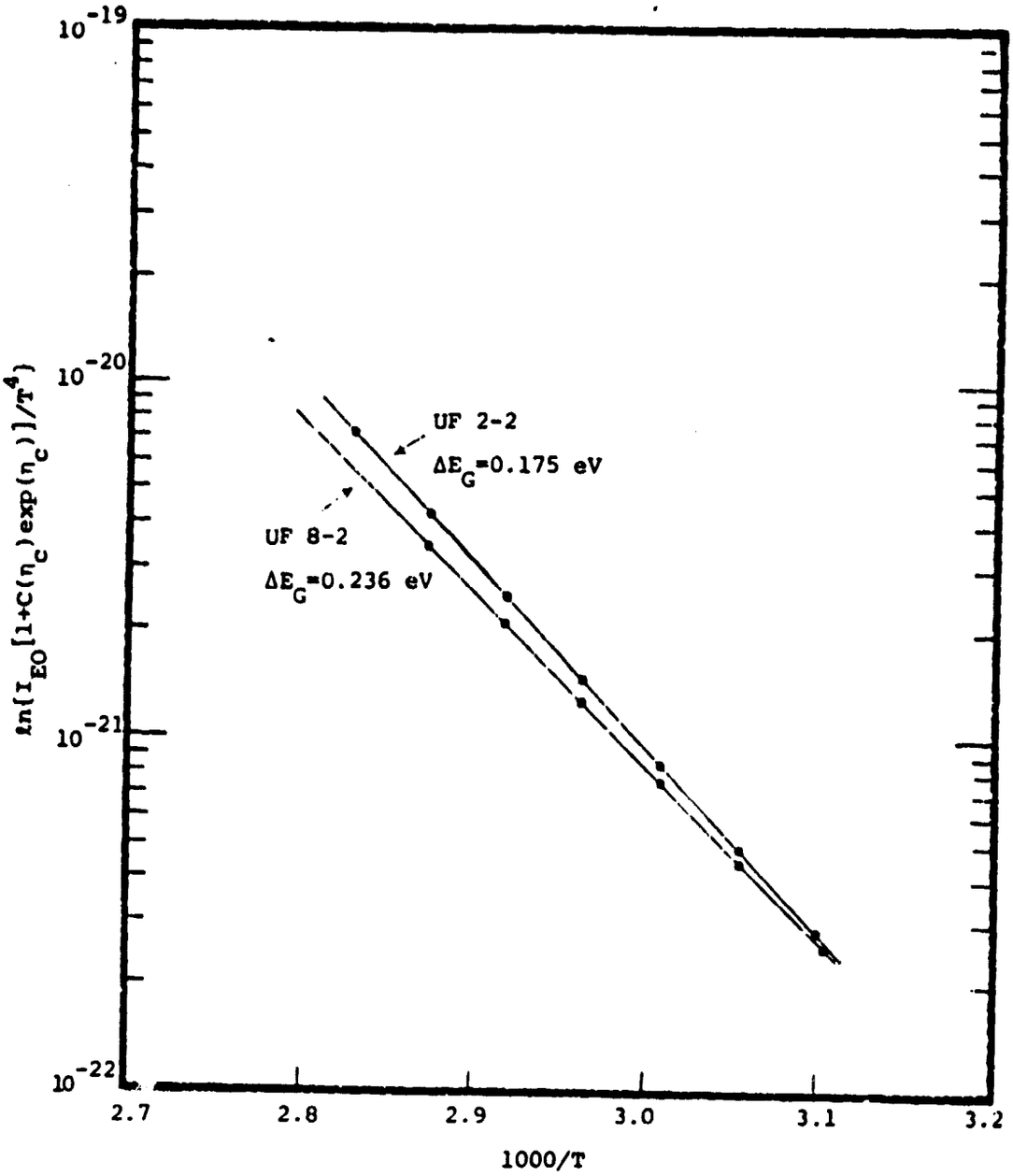

Figure 2.12 $\ln[I_{EO}[1+C(\eta_c)\exp(\eta_c)]/T^4]$ vs. 1000/T for diode UF2-2 and UF 8-2.

Table 2.6 Bandgap Narrowing ΔE_G as a Function of Emitter Doping Concentration.

Device	Emitter Concentration (cm^{-3})	ΔE_G (eV)
UF 2-2 (diode)	3.0×10^{19}	0.175
UF 12-2 (diode)	1.0×10^{20}	0.204
UF 8-2 (diode)	1.5×10^{20}	0.236
SHF 70 (transistor)	1.5×10^{20}	0.225
TXA (transistor)	1.5×10^{20}	0.227
UF 3-2 (diode)	2.1×10^{20}	0.247

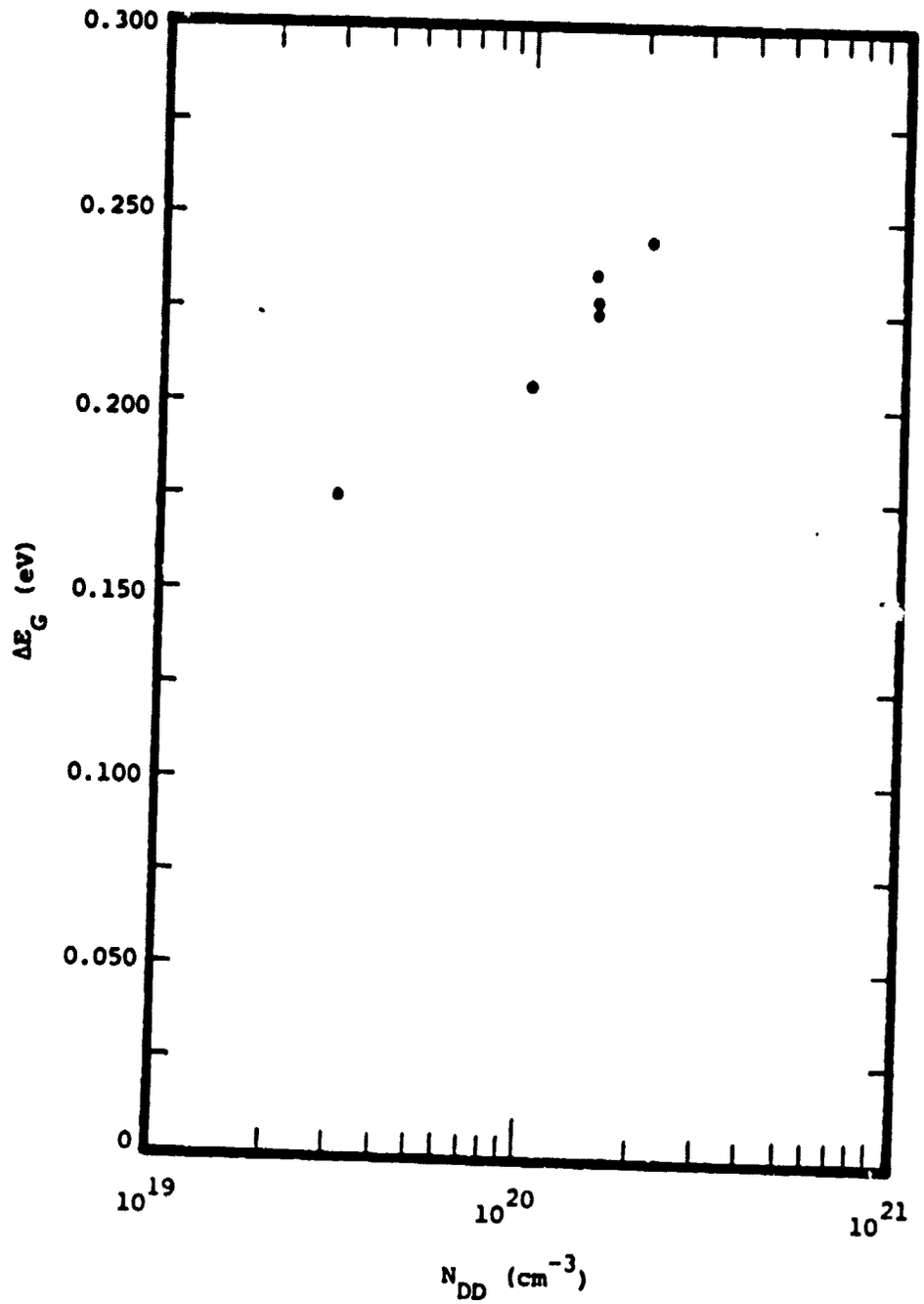

Figure 2.13 Experimentally determined ΔE_G as a function of arsenic doping concentration.

2.4 Discussion

We have demonstrated an experimental method to study energy bandgap narrowing in heavily-doped emitter regions. This method employs the study of temperature dependence of the minority carrier recombination current in a thin transparent emitter. The accuracy in determining ΔE_G relies on an accurate description of the variation of emitter saturation current I_{EO} with temperature and also on the accuracy in obtaining the emitter saturation current from the I-V characteristics.

In deriving (2.15), which describes the temperature variation of the emitter saturation current, we have assumed that the minority-carrier mobility and majority-carrier concentration are temperature independent and that the energy bandgap in intrinsic silicon varies linearly with temperature. At lower temperatures (below 200 K), these assumptions may be questionable [6,25], particularly for emitters with lower doping concentrations (below 10^{19} cm^{-3}). To minimize these possible sources of error, we have selected the measurement temperature range to be between 320 K and 380 K. We note that (2.15) and (2.17) hold only for a transparent emitter. This requires the hole lifetime τ_p in the emitter to be longer than the hole transit time $W_E^2/2D_p$. As an example, for an n^+ emitter with a doping concentration of 10^{20} cm^{-3} and W_E = 0.25 μm, the hole transit time is approximately 0.2 nsec which is smaller than the hole Auger lifetime of 0.6 nsec reported for this doping concentration [31,32]. In this calculation, we assume D_p = 1.5 cm^2/sec at 320 K. At higher temperatures, D_p increases slightly with temperature and therefore the transit time is shorter. For thicker emitters, recombination processes such as Auger recombination and Shockley-Read-Hall recombination can be important in the emitter bulk region and W_E in (2.14) should be replaced

by the corresponding diffusion length L_p. Under this situation, the emitter is defined to be opaque to the minority holes. However, if L_p does not vary significantly with temperature in the range of measurement temperature, (2.15) remains valid. Despite these possible sources of error, it is preferable to use (2.15) to determine ΔE_G rather than determining ΔE_G from a single value of I_{E0} using (2.17). The uncertainty in D_p in the heavily-doped n^+ region may cause large error in ΔE_G.

The experimental accuracy in the I-V measurement is extremely good. The current standard we use has an accuracy about ± 1 nA. Thus the accuracy in determining I_{E0} from the I-V characteristics depends mostly on the device having a well-defined space-charge recombination current component so that the ideal recombination current component can be separated from the measured I-V characteristics accurately. Devices with surface and other leakage current components are not suitable for this measurement. We estimate the error in determining I_{E0} to be less than 3%. Assuming the values of I_{E0} can be obtained sufficiently accurate, the uncertainty in ΔE_G, which is related to the slope of the activation energy plot, can be reduced by taking more values of I_{E0} at closer temperature intervals. The experimental accuracy in determining ΔE_G, as obtained by a least-square-fit to the measured data as shown in Figs. 2.7 and 2.12, is estimated to be ± 5 meV.

We now discuss the experimental result further. Consider device UF 8-2, for example. J_{E0} is found to be 5.72×10^{-11} amp/cm^2 at 322.2 K for this device. The large value of dark saturation current density in this device cannot be explained by an opaque emitter with very short minority-carrier lifetime alone. If we ignore the effect of bandgap

narrowing and relate the saturation current in an opaque emitter, $qn_{io}^2 D_p/N_{DD}L_p[1+C(\eta_c)\exp(\eta_c)]$, to the measured dark saturation current density, a minority-carrier lifetime as low as 10^{-16} sec. is required to account for the dark recombination current measured. These low values for minority-carrier lifetime are not consistent with lifetimes reported in heavily-doped silicon [31,32] and are lower than the mean free time between collisions. Inclusion of the effect of bandgap narrowing provides a model that is consistent with the large observed value of saturation current density.

In this chapter, we have concentrated our study on n^+ emitters. For devices with p^+ emitters we anticipate the effect of Fermi-Dirac statistics to be more significant because $N_V < N_C$. For silicon, the value of N_V is about a factor of three lower than the value of N_C. Thus for an n^+ emitter with doping concentration of 3×10^{19} cm^{-3} ($\approx N_C$), the effect of majority-carrier degeneracy depresses the minority-carrier concentration by about a factor of 0.7 at 300 K, as shown in Fig. 2.2; but, for a p^+ emitter, a doping concentration of 1×10^{19} cm^{-3} ($\approx N_V$) suffices to depress the minority-carrier concentration by the same factor of 0.7. We note here that other workers [7,8,13] have not taken into account the effect of Fermi-Dirac statistics in their studies of energy bandgap narrowing in silicon p-n junction devices. Our results indicate that, for an n^+ region with doping concentration of 3×10^{19} cm^{-3} (device UF 2-2), this neglect underestimates ΔE_G by about 0.015 eV. For an n^+ region with doping concentration of 2.1×10^{20} cm^{-3} (device UF 3-2), the underestimation in ΔE_G is about 0.070 eV. These results can be obtained from the plot of $\ell n[I_{EO}/T^4]$ versus 1000/T. For a p^+ emitter with the same doping concentration, the underestimation in ΔE_G by neglecting the effect of Fermi-Dirac statistics would be even greater.

REFERENCES FOR CHAPTER 2

1. M.B. Prince, "Silicon solar energy converters," J. Appl. Phys., Vol. 26, pp. 534-540, May 1955.

2. F.A. Lindholm and C.T. Sah, "Fundamental electronic mechanisms limiting the performance of solar cells," IEEE Trans. Electron Devices, Vol. ED-24, pp. 299-304, April 1977.

3. F.A. Lindholm, A. Neugroschel, C.T. Sah, M. Godlewski, and H.W. Brandhorst, Jr., "A methdology for experimentally based determination of gap shrinkage and effective lifetimes in the emitter and base of p-n junction solar cells and other p-n junction devices," IEEE Trans. Electron Devices, Vol. ED-24, pp. 402-410, April 1977.

4. A. Neugroschel, F.A. Lindholm, and C.T. Sah, "A method for determining the emitter and base lifetimes in p-n junction diodes," IEEE Trans. Electron Devices, Vol. ED-24, pp. 662-671, June 1977.

5. J.R. Hauser and P.M. Dunbar, "Minority carrier reflecting properties of semiconductor high-low junctions," Solid State Electronics, Vol. 18, pp. 715-716, 1975.

6. J.W. Slotboom and H.C. deGraaff, "Measurements of bandgap narrowing in silicon bipolar transistors," Solid State Electronics, Vol. 19, pp. 857-862, Oct. 1976.

7. R.U. Martinelli, "The temperature dependence of the base and collector currents in silicon bipolar transistors," IEEE Trans. Electron Devices, Vol. ED-23, pp. 1218-1224, Nov. 1976.

8. W.L. Kauffman and A.A. Bergh, "The temperature dependence of ideal gain in double diffused silicon transistors," IEEE Trans. Electron Devices, Vol. ED-15, pp. 732-735, Oct. 1968.

9. H.J.J. DeMan, "The influence of heavy doping on the emitter efficiency of a bipolar transistor," IEEE Trans. Electron Devices, Vol. ED-18, pp. 833-835, Oct. 1971.

10. R. Mertens and R. Van Overstraeten, "Measurement of the minority carrier transport parameters in heavily doped silicon," Tech. Digest 1978 Int. Electron Devices Mtg., pp. 320-323, Dec. 1978.

11. H.P.D. Lanyon, A.K. McCurdy, and R.A. Tuft, "Infrared photoresponse of silicon devices at 1.15 microns," Record of 13th IEEE Photovoltaic Specialist Conference, pp. 60-63, June 1978.

12. A. Neugroschel, C.T. Sah, and F.A. Lindholm, "Experimental determination of the stored charge and effective lifetime in the emitter of junction transistors," IEEE Trans. Electron Devices, Vol. ED-24, pp. 1362-1365, Dec. 1977.

13. R.U. Martinelli, "Comments on bandgap narrowing in silicon bipolar transistors," IEEE Trans. Electron Devices, Vol. ED-24, pp. 1310-1311, Nov. 1977.

14. T.N. Morgan, "Broadening of impurity bands in heavily doped silicon," Physical Review, Vol. 139, pp. 343-348, July 1965.

15. E.O. Kane, "Thomas Fermi approach to impure semiconductor band structure," Physical Review, Vol. 131, pp. 79-88, July 1963.

16. D.D. Kleppinger and F.A. Lindholm, "Impurity concentration dependent density of states and resulting Fermi level for silicon," Solid State Electronics, Vol. 14, pp. 407-416, May 1971.

17. H.P.D. Lanyon and R.A. Tuft, "Bandgap narrowing in heavily doped silicon," Tech. Digest 1978 Int. Electron Devices Mtg., pp. 316-318, Dec. 1978.

18. M.A. Shibib, F.A. Lindholm, and F. Therez, "Heavily doped transparent emitter regions in junction solar cells, diodes, and transistors," IEEE Trans. Electron Devices, Vol. ED-26, pp. 959-965, June 1979.

19. R.J. Van Overstraeten, H.J. DeMan, and R.P. Mertens, "Transport equations in heavy doped silicon," IEEE Trans. Electron Devices, Vol. ED-20, pp. 290-298, March 1973.

20. K.M. van Vliet and A.H. Marshak, "Conduction current and generalized Einstein relations for degenerate semiconductor and metals," Phys. Stat. Sol. (b), Vol. 78, pp. 501-517, 1976.

21. S.C. Pao, Unpublished experimental results. The conclusion is based on the 20-25 mV increase in open-circuit voltage after the titanium-silver ohmic contact at the back surface is removed. The p^+-n-n^+ BSF solar cells are fabricated by Sandia Laboratories.

22. P.T. Landsberg, R.W. Mackay, and A.D. McRonald, "The parameters of simple excess semiconductors," Proc. Phys. Soc. A, p. 476, 1950.

23. G.L. Pearson and J. Bardeen, "Electrical properties of pure silicon and silicon alloys containing boron and phosphorous," Physical Review, Vol. 75, No. 4, pp. 865-883, March 1949.

24. H.M. Rein, H.V. Rohr, and P. Wennekers, "A contribution to the current gain temperature dependence of bipolar transistors," Solid State Electronics, Vol. 21, pp. 439-442, 1978.

25. G.G. McFarlane, J.P. McLean, J.E. Quarrington, and V. Roberts, "Fine structure in the absorption-edge spectrum of Si," Physical Review, Vol. 111, No. 5, pp. 1245-1254, Sept. 1958.

26. H.D. Barbar, "Effective mass and intrinsic concentration in silicon," Solid State Electronics, Vol. 10, pp. 1039-1051, 1967.

27. W. Bludau and A. Onton, "Temperature dependence of the bandgap of silicon," J. Appl. Phys., Vol. 45, pp. 1846-1848, April 1974.

28. R.S. Muller and T.I. Kamins, Device Electronics for Integrated Circuit, John Wiley and Sons, New York, 1977, pp. 32-33.

29. C.T. Sah, "Effec of surface recombination and channel on p-n junction and transistor characteristics," IRE Trans. Electron Devices, Vol. ED-9, pp. 94-108, Jan. 1962.

30. W. Rosenzeweig, "Diffusion length measurement by means of ionizing radiation," Bell System Technical Journal, pp. 1573-1588, Sept. 1962.

31. J. Dziewior and W. Schmid, "Auger coefficients for highly doped and highly excited silicon," Applied Physics Letters, Vol. 31, No. 5, pp. 346-348, Sept. 1977.

32. A.W. Wieder, "Arsenic emitter effects," Tech. Digest 1978 Int. Electron Devices Mtg., pp. 460-462, Dec. 1978.

CHAPTER 3

HEAVILY-DOPED TRANSPARENT EMITTER REGIONS IN JUNCTION SOLAR CELLS, DIODES, AND TRANSISTORS

I. Introduction

Excess minority carrier injected into the emitter of p-n junction devices recombine in the bulk and at the surface of the emitter. If the emitter junction is shallow enough, the minority carriers can cross the quasi-neutral emitter region without appreciable bulk recombination. The minority carriers then recombine at the emitter surface. For this case the emitter is transparent to the injected minority carriers, and an important parameter then is the surface recombination velocity S at the emitter surface.

This parameter is particularly important for p-n junction silicon solar cells in which most of the illuminated surface is not covered by metal. In devices in which thermal SiO_2 covers this nonmetallized portion of the surface, experiments show that S can be less than 10^4 cm/sec for both p-cells (p-type substrate) [1] and n-cells [1]. This value of S is orders of magnitude less than that at an ohmic contact and is consistent with values determined earlier by different experimental methods [2]. Furthermore, recent experiments on p-cells [1] and n-cells [1] demonstrate that the emitter can be completely transparent.

The purpose of this paper is to provide an analytical treatment of transparent emitter devices, particularly solar cells, that is more complete than treatments previously available [3-8]. In this treatment, we include the effects of: (a) bandgap narrowing [9,10], (b) Fermi-Dirac statistics, (c) built-in field due to the impurity profile, and (d) a finite surface recombination velocity S. Detailed numerical studies including these various effects have been done [11-13], but they have not treated the case of the transparent emitter.

A major result of the paper is the demonstration that the transparent-emitter model can predict experimental values of V_{OC} observed on n^+-p thin diffused junction silicon solar cells made on low-resistivity (0.1 Ω-cm) substrates. Thus, the transparent-emitter model is shown to provide an explanation for the discrepancy between the prediction of simple classical theory ($V_{OC} \cong 700$ mV) and the measured maximum value ($V_{OC} \cong 600$ mV). The transparent-emitter model gives $V_{OC} \cong 600$ mV for high values of S_p ($S_p > 10^4$ cm/sec) provided the effects of bandgap narrowing (modified by Fermi-Dirac statistics) are included. This result suggests that V_{OC} can be increased toward the classical value of 700 mV if S_p is decreased and the effects of bandgap narrowing are reduced. This is accomplished in the HLE solar cells, early versions of which have shown increases in V_{OC} to the 640-650 mV range [14].

In addition to the development of the theory for the transparent-emitter device, and its application to solar cells, the paper will include a test for the self-consistent validity of the transparent-emitter model. This test compares the calculated transit time of minority carriers across the emitter with the Auger-impact minority carrier lifetime within the emitter region.

II. Derivation

We consider an n-type heavily doped quasi-neutral emitter region; analogous results apply to p-type emitters. The minority carrier current density in the n-type region is

$$J_p(x) = q\mu_p \Delta P(x) E(x) - qD_p \frac{d\Delta P(x)}{dx} \qquad (1)$$

If low-level injection in the emitter is assumed, then E(x) is given by its thermal-equilibrium value,

$$E(x) = \frac{D_p}{\mu_p} \cdot \frac{1}{P_0(x)} \cdot \frac{dP_0(x)}{dx} \quad . \tag{2}$$

We now define an effective intrinsic density n_{ie} such that

$$n_{ie}^2(x) = P_0(x)\, N_0(x) \tag{3}$$

in which $P_0(x)$ and $N_0(x)$ are the hole and electron concentrations in thermal equilibrium. The parameter n_{ie}^2 depends on position for two reasons:

1. the influence of Fermi-Dirac statistics, and
2. the influence of bandgap narrowing.

These influences are discussed in section III. For Maxwell-Boltzmann statistics and no bandgap narrowing, n_{ie}^2 is the square of the intrinsic carrier concentration in silicon and is a function of temperature only.

If the expressions in (2) and (3) are used in (1), we get, after some manipulations,

$$J_p(x) \frac{N_0(x)}{n_{ie}^2(x)}\, dx = -qD_p d\left[\Delta P(x) \cdot \frac{N_0(x)}{n_{ie}^2(x)}\right]. \tag{4}$$

If we integrate (4) over the quasi-neutral emitter region, we get

$$\int_0^{W_E} J_p(x) \cdot \frac{N_0(x)}{n_{ie}^2(x)}\, dx = -\, q\bar{D}_p \left[\Delta P(x) \cdot \frac{N_0(x)}{n_{ie}^2(x)}\right]_0^{W_E} \tag{5}$$

where $\bar{D}_p$ is some average value of D_p. If the emitter is transparent (transit-time limited), that is, if the minority carrier transit time τ_t is much less than the minority carrier lifetime τ_p (for an n-type emitter), then J_p is constant independent of position in the emitter.

Use of the minority carrier boundary conditions [15]

$$\Delta P(0) = P_0(0)\ (e^{qV/kT} - 1) \tag{6}$$

at the edge of the emitter space charge region, and

$$J_P(W_E) = q \cdot S_p \cdot \Delta P\ (W_E) \tag{7}$$

at the emitter surface, enable (5) to be expressed as

$$J_P = \frac{q\bar{D}_P(e^{qV/kT} - 1)}{\int_0^{W_E} \frac{N_0(x)}{n_{ie}^2(x)}\, dx + \frac{\bar{D}_P \cdot N_0(W_E)}{S_p \cdot n_{ie}^2(W_E)}} \tag{8}$$

Equation (8) is the general expression for the minority carrier current in a transparent emitter.

To check the condition, $\tau_t << \tau_p$, required for transparency, we must determine the steady-state transit time τ_t, which is defined by the charge control relation,

$$\tau_t = \frac{Q_P}{J_P} . \tag{9}$$

Here Q_P is the excess minority carrier charge storage in the emitter:

$$Q_P = q \int_0^{W_E} \Delta P(x)\ \ dx \tag{10}$$

Using (4), (8), and (10) to express Q_P, and combining with (9), we

find the following expression for the minority carrier transit time:

$$\tau_t = q\left\{\left[\frac{1}{\bar{D}_p}\int_0^{W_E}\frac{N_0(x)}{n_{ie}^2(x)}\,dx + \frac{N_0(W_E)}{S_p \cdot n_{ie}^2(W_E)}\right]\cdot\int_0^{W_E}\frac{n_{ie}^2(x)}{N_0(x)}\,dx - \frac{1}{\bar{D}_p}\int_0^{W_E}\int_0^{x}\frac{N_0(x')}{N_0(x)}\cdot\frac{n_{ie}^2(x)}{n_{ie}^2(x')}\,dx'\,dx\right\} \tag{11}$$

Some special cases are of interest. For a flat impurity concentration profile, the above expression reduces to

$$\tau_t = \frac{W_E^2}{2\bar{D}_p} + \frac{W_E}{S_p} \tag{12}$$

If, furthermore, S_p is infinite, (12) reduces to the familiar expression,

$$\tau_t = \frac{W_E^2}{2\bar{D}_p} . \tag{13}$$

III. Heavy Doping Effects

In thermal equilibrium, heavy doping concentrations of shallow level impurities affect the minority carrier concentration in a quasi-neutral region by two mechanisms: bandgap narrowing and Fermi-Dirac statistics. These two mechanisms affect the minority carrier concentration in opposite ways. For any given position of the Fermi level relative to the band edges, bandgap narrowing tends to increase the

minority carrier concentration, while inclusion of Fermi-Dirac statistics tends to decrease the minority carrier concentration below the value calculated using Maxwell-Boltzmann statistics. The dominance of either of the two effects, at any specific impurity concentration, depends on the model of bandgap narrowing adopted.

In this treatment, we assume that bandgap narrowing occurs without changing the parabolic dependence on energy of the density of states in the conduction and valence bands. This is the rigid-band approximation.

The effects of bandgap narrowing and Fermi-Dirac statistics can be lumped into a position-dependent effective intrinsic carrier concentration at thermal equilibrium given by

$$n_{ie}^2(x) = \frac{n_i^2 e^{\Delta E_G(x)/kT}}{1 + C(\eta)\, e^{\eta}} \tag{14}$$

where

$$\eta = \eta_C = (E_F - E_C)\ /kT \tag{15}$$

for n-type material, and

$$\eta = \eta_V = (E_V - E_F)\ /kT \tag{16}$$

for p-type material. The derivation of (14) appears in the Appendix. In (15) and (16), E_C and E_V are the edges of the conduction and valence bands, respectively, and E_F is the Fermi level. The factor $C(\eta)$ is a function of η, which, for $\eta \leq 4$ (e.g., $N_0 \leq 2 \times 10^{20}$ cm^{-3} in n-type silicon), is [16]

$$C(\eta) \cong - 0.04\eta + 0.3 \tag{17}$$

The above approximation of $C(\eta)$ gives values of the Fermi-Dirac intergral of order ½ (see Appendix) with less than 4% error.

In nonequilibrium conditions, bandgap narrowing increases the minority carrier current by:

1. Increasing the minority carrier concentration.
2. Decreasing the retarding built-in electric field acting on the minority carriers.

The increase in the minority carrier concentration P results from the increase in $n_{ie}^2(x)$. The decrease of the built-in electric field is due to the position dependence of $n_{ie}^2(x)$ (and hence of the effective bandgap) in the inhomogeneously doped emitter.

To develop a simple expression illustrating the reduction of the electric field, we now include only bandgap narrowing excluding the effect of Fermi-Dirac statistics for the present. Then the effective electric field acting on the minority carriers, given in (2), can be expressed by using (3) and (4) as:

$$E(x) = A(N_0) \left[- \frac{D_N}{\mu_N} \cdot \frac{1}{N_0(x)} \cdot \frac{dN_0(x)}{dx} \right] \tag{18}$$

where

$$A(N_0) \equiv \left[1 - \frac{N_0(x)}{KT} \cdot \frac{d\,\Delta E_G(x)}{dN_0(x)} \right] \tag{19}$$

The factor $A(N_0)$ measures the reduction of the built-in electric field due to bandgap narrowing. For any model of bandgap narrowing, $A(N_0)$ is always less than one. Figure 1 shows $A(N_0)$ as a function of the electron (majority carrier) concentration for three models of bandgap narrowing: Slotboom and DeGraaff [17], Hauser [18], and Lanyon and Tuft [19].

In the absence of bandgap narrowing, the holes experience a retarding electric field in an n-type diffused emitter. Equations (18) and (19) indicate that the position dependence of the bandgap narrowing, in effect, decreases the retarding electric field. The more it is decreased the smaller is the transit time for a specific surface recombination velocity. In (11) the transit time is shown to be a function of n_{ie}^2. In Figure 2 the transit time is plotted as a function of W_E, the width of the quasi-neutral emitter region, in two cases: neglecting bandgap narrowing, and including bandgap narrowing (Slotboom and De Graaff model). Note that inclusion of bandgap narrowing makes the transit time close to the value it has if the impurity profile is flat. In general, bandgap narrowing decreases the transit time if the impurity profile is not flat.

Conversely, inclusion of Fermi-Dirac statistics increases the transit time as can be seen in Figure 2. Inclusion of Fermi-Dirac statistics shifts the value of the transit time closer to that calculated when heavy doping effects are neglected.

IV. Discussion

From (8), the minority carrier saturation current for a transparent emitter is

$$J_{PO} = \frac{q\bar{D}_p}{\int_0^{W_E} \frac{N_0(x)}{n_{ie}^2(x)}\,dx + \frac{D_p N_0(W_E)}{S_p n_{ie}^2(W_E)}} \quad . \tag{20}$$

If

$$S_p >> \frac{N_0(W_E)}{n_{ie}^2(W_E)} \cdot \frac{\bar{D}_p}{\int_0^{W_E} \frac{N_0(x)}{n_{ie}^2(x)}\,dx} \quad , \tag{21}$$

then (20) reduces to

$$J_{PO} \cong \frac{q\bar{D}_P}{\int_0^{W_E} \frac{N_0(x)}{n_{ie}^2(x)}\,dx} \tag{22}$$

which is the exact expression for an infinite surface recombination velocity. For

$$S_P << \frac{N_0(W_E)}{n_{ie}^2(W_E)} \cdot \frac{\bar{D}_P}{\int_0^{W_E} \frac{N_0(x)}{n_{ie}^2(x)}\,dx}\,, \tag{23}$$

(20) reduces to

$$J_{PO} \cong \frac{qS_P n_{ie}^2(W_E)}{N_0(W_E)}\,. \tag{24}$$

It is desirable to make J_{PO} small for the bipolar transistor. This results in a large emitter efficiency. For the p-n junction solar cell, if the emitter recombination current J_{PO} is small compared with the base recombination current, the value of V_{OC} can approach the classical theoretical limit.

To illustrate the dependence of J_{PO} on S_P, consider the desirable case in the transparent-emitter model in which S_P is small enough to satisfy (23). Figures 3 and 4 show the variation of the emitter saturation current density, J_{PO}, and the transit time, τ_t, as a function of S_P for three models of bandgap narrowing: Slotboom and De Graaff [17], Hauser [18], and the recent model of Lanyon and Tuft [19], which has the form

$$\Delta E_G = 22.5 \times 10^{-3} \, (N/10^{18})^{1/2} \quad eV$$

for non-degenerately doped silicon, and (25)

$$\Delta E_G = 162. \times 10^{-3} \, (N/10^{20})^{1/6} \quad eV$$

for degenerately doped silicon.

A Gaussian impurity profile is assumed with a surface impurity concentration of 10^{20} cm^{-3} and a junction depth of .25 μm. Full ionization of the impurity atoms is also assumed.

For values of S_p below 10^6 cm/sec, J_{PO} and τ_t vary rapidly with variations in S_p, while for values of S_p above 10^6 cm/sec, both J_{PO} and τ_t saturate. J_{PO} saturates to its largest value, and τ_t saturates to its lowest value. The largest value of J_{PO} at any S_p occurs for the Lanyon-Tuft model of bandgap narrowing.

The validity of the transparent emitter model is based on the condition that the minority carrier transit time is much smaller than the minority carrier lifetime: $\tau_t \ll \tau_p$. To test this condition, τ_t is calculated from (11). Values of τ_t are plotted in Figures 4 and 5. In Figure 4, τ_t is plotted as a function of S_p for the three models of bandgap narrowing (assuming W_E = .25 μm). While in Figure 5, values of τ_t are plotted as a function of the quasi-neutral emitter region width, W_E, for $S_p = 5 \times 10^5$ cm/sec. The recombination lifetime τ_p has an upper bound determined by the Auger band-to-band recombination at high impurity concentration.

To illustrate the self-consistency test for transparency, we assume the surface concentration of a diffused emitter to be 10^{20} cm^{-3}. With the impurity profile assumed gaussian, this corresponds to an average

Auger lifetime of $\tau_A = 2.4 \times 10^{-9}$ sec [20]. In Figures 4 and 5, we compare this lifetime with τ_t for each of the three bandgap narrowing models (assuming that $W_E = 0.25$ μm). Note that the emitter is completely transparent if S_p exceeds 10^5 cm/sec and is opaque if S_p is below 10^4 cm/sec.

V. Application to p-n Junction Silicon Solar Cells

In this section, we apply the transparent-emitter model to calculate the open-circuit voltage of silicon p-n junction solar cells having low substrate resistivity.

The open-circuit voltage is given by

$$V_{OC} \cong \frac{kT}{q} \ell n \frac{J_{SC}}{J_0} \tag{26}$$

where J_{SC} is the short-circuit current density and J_0 is the saturation current of the solar cell in the dark. The saturation current density J_0 of the diode is

$$J_0 = J_{PO} + J_{NO} \tag{27}$$

where J_{PO} is the emitter minority carrier saturation current density and J_{NO} is the base minority carrier saturation current density.

The base saturation current density is

$$J_{NO} = \frac{qn_i^2 D_N}{N_{AA} L_N} . \tag{28}$$

Consider low-resistivity silicon solar cells with base doping concentration of $N_{AA} = 5 \times 10^{17}$ cm^{-3}. Measurements made on such cells indicated the minority carrier diffusion length, L_N, to be 80 μm [21], corresponding to $J_{NO} \cong 6.2 \times 10^{-14}$ A/cm^2. The general expression for

the transparent emitter current density, given in (8), has yielded J_{PO} as a function of S_p, as shown in Figure 3.

Combining these characterizations for J_{NO} and J_{PO} with J_{SC} = 23 mA/cm^2 (AMO conditions) [22], we plot, in Figure 6, V_{OC} versus S_p. For low S_p (about 10^3 cm/sec), V_{OC} is limited by the base current, and for higher values of S_p, V_{OC} is limited by the emitter current, as has been observed experimentally [22]. Note that for $S_p > 10^5$ cm/sec, V_{OC} saturates to its lowest value. Note also that the Lanyon and Tuft model of bandgap narrowing gives lower values of V_{OC} (for any given value of S_p) than those given by the Slotboom and De Graaff and Hauser models.

So far we have assumed, for simplicity, that all of the emitter surface is characterized by a single value of S_p. We now consider a more realistic structure of silicon solar cells, Figure 7(a). The emitter saturation current J_{PQ} is the sum of three components from regions 1, 2, and 3 shown in Figure 7(b), [23]. The components of the current density from the metal-covered surface, region 1, and the nonmetal-covered surface, region 2, are given by (8). In region 3, the flow of minority carriers is two-dimensional since the minority carriers within about a diffusion length from region 1 are much more influenced by the high value of S_p of region 1 than they are by the relatively low value of S_p of region 2. To avoid the complexity of two-dimensional analysis, we make the first-order approximation that the component of J_{PO} from region 3 is essentially the same as that from region 1 ($J_{P3} \cong J_{P1}$) because S_p of the unmetallized surface can be made orders of magnitude smaller than S_p of the ohmic contact.

The emitter saturation current is then

$$I_{PO} = (A_1 + A_3)\ J_{PO1} + A_2 J_{PO2} \tag{29}$$

where A_1 is the metallized surface area and $(A_2 + A_3)$ is the unmetallized surface area and J_{PO1} and J_{PO2} are the corresponding currents. The area A_3 is approximately equal to

$$A_3 \cong 2nL_G L_P \tag{30}$$

where n is the number of metal grid lines (or fingers), L_G is the length of the grid lines (see Figure 7), and $A_2 = A_T - (A_3 + A_1)$, A_T being the total area of the cell.

As a numerical example, let $A_T = 4\ cm^2$, $L_G = 2$ cm, $n = 6$, $L_P \cong 1\mu m$, and assume 10% metal coverage. Then $A_1 \cong 0.4\ cm^2$, $A_2 \cong 3.59\ cm^2$, and $A_3 \cong 0.0024\ cm^2$. In this case, A_3 is negligible, and

$$V_{OC} = \frac{kT}{q}\ \ell n\ \frac{J_{SC}}{\frac{A_1}{A_T} \cdot J_{PO1} + \frac{A_2}{A_T} \cdot J_{PO2} + J_{NO}} \tag{31}$$

This expression can be used to estimate S_P of the nonmetallized surface from experimental values of V_{OC}. For diffused, thin-junction p-n junction solar cells made on low resistivity ($\cong 0.1\ \Omega$-cm) material, the maximum observed open-circuit voltage is about 600 mV [22]. As one example, if we consider the Lanyon-Tuft model of bandgap narrowing, and let S_P of the ohmic contact be 10^6 cm/sec, let the doping concentration be gaussian with a surface concentration of $10^{20}\ cm^{-3}$, then by using (31), with $A_1/A_T = 0.1$ and $V_{OC} = 600$ mV, we get S_P (nonmetal) = 5×10^4 cm/sec. Thus this value for S_P could result in the low V_{OC} seen in conventional,

diffused, thin-junction solar cell. Note that Figures 4 and 5 indicate the self-consistent validity of the transparency assumption for this device in the Lanyon-Tuft model which permits use of (30).

Although the preceding discussion has focused on the transparent emitter model applied to n^+-p silicon solar cells, the model can also be applied to p^+-n cells. It is straightforward to show that heavy doping effects (bandgap narrowing and Fermi-Dirac statistics) degrade n^+-p cell performance more than that of p^+-n cells because the effective mass of electrons in silicon is greater than the effective mass of holes. The resulting different effective densities of states in the conduction and valence bands (N_C and N_V) cause the onset of degeneracy to occur at lower impurity concentrations in p-type material than in n-type material [13], if both n-type and p-type regions have the same bandgap narrowing. Thus the net effect of bandgap narrowing and Fermi-Dirac statistics is to degrade the n-type heavily doped region more than the p-type region with the same impurity concentration. This may, in part, be responsible for the high efficiency p^+-n-n^+ cells that have been observed experimentally [24].

VI. Perspective

This paper has dealt with the transparent-emitter model of a solar cell, which is defined by the condition that the minority carriers in the dark quasi-neutral emitter recombine mainly at the surface rather than in the bulk. Surface recombination can predominate over bulk recombination if the emitter junction depth is shallow enough and if the surface recombination velocity is high enough. In fact, this occurs in typical pn-junction silicon solar cells, as demonstrated by recent

experiments showing the sensitivity of V_{OC} to the surface recombination velocity [1]. From a theoretical standpoint, the self-consistency test in Section IV can determine the validity, for a given solar cell, of the transparent-emitter model, provided the emitter recombination center density is low enough for the Auger process to dominate over the Shockley-Read-Hall process.

Although the transparent-emitter model may describe many conventional shallow pn-junction silicon solar cells, the high value of the surface recombination velocity S necessary to validate the transparent-emitter model is not necessarily desirable from a design point of view. Growth of a thermal SiO_2 layer on the emitter surface can substantially decrease S and increase V_{OC}, particularly if a high-low junction barrier is present near the emitter surface [14]. For such devices, the dark emitter recombination current is determined mainly by bulk recombination.

Appendix

In thermal equilibrium, for a parabolic quantum density of states, the concentrations of charge carriers in a semiconductor are given by

$$N_0 = N_C F_{\frac{1}{2}}(\eta_C) \tag{A-1}$$

$$P_0 = N_V F_{\frac{1}{2}}(\eta_V) \tag{A-2}$$

where N_C and N_V are the effective density of states in the conduction and valence bands, respectively, $F_{\frac{1}{2}}$ is the Fermi-Dirac integral of order $\frac{1}{2}$, and

$$\eta_C = (E_F - E_C)/KT \tag{A-3}$$

$$\eta_V = (E_V - E_F)/KT \tag{A-4}$$

As suggested by Landsberg et al. [16], the analytic approximation

$$F_{\frac{1}{2}}(\eta) = \frac{e^{\eta}}{1 + C(\eta)e^{\eta}} \tag{A-5}$$

can be used in the range $-4 \leq \eta \leq +10$. Here $C(\eta)$ is a function of η given in figure 4 of [16].

Using (A-5) in (A-1) and (A-2), we can write

$$N_0 = \frac{N_C e^{\eta_C}}{1 + C(\eta_C)\, e^{\eta_C}} \tag{A-6}$$

$$P_0 = \frac{N_V e^{\eta_V}}{1 + C(\eta_V)\ e^{\eta_V}} \tag{A-7}$$

Thus, from (A-6) and (A-7),

$$n_{ie}^2(x) = N_0 P_0 = \frac{N_C N_V e^{-E_G(x)/KT}}{1 + C(\eta_C) e^{\eta_C} + C(\eta_V)\ e^{\eta_V} + C(\eta_C)\ C(\eta_V)\ e^{-E_G(x)/KT}} \tag{A-8}$$

where

$$E_G(x) = E_{GO} - \Delta E_G(x)\ , \tag{A-9}$$

in which E_{GO} is the bandgap of the intrinsic semiconductor, and $\Delta E_G(x)$ is the bandgap narrowing due to heavy doping. For an n-type heavily doped region, $\eta_V << 0$ and $C(\eta_V) = 0$ in (A-8). Furthermore, the term $C(\eta_C)\ C(\eta_V)\ e^{-E_G(x)/KT} << 1$. Therefore, for a heavily doped n-type region, (A-8) reduces to

$$n_{ie}^2(x) = N_0 P_0 = \frac{n_i^2 e^{\Delta E_G(x)/KT}}{1 + C(\eta_C)\ e^{\eta_C}} \tag{A-10}$$

Similarly, for a p-type heavily doped region

$$n_{ie}^2(x) = N_0 P_0 = \frac{n_i^2 e^{\Delta E_G(x)/KT}}{1 + C(\eta_V)\, e^{\eta_V}} \qquad \text{(A-11)}$$

In (A-10) and (A-11), n_i is the intrinsic concentration in the pure semiconductor.

REFERENCES FOR CHAPTER 3

[1] J. G. Fossum, F. A. Lindholm, and M. A. Shibib, "The Importance of Surface Recombination and Energy Bandgap Narrowing in PN-Junction Silicon Solar Cells", submitted for publication in IEEE Transactions on Electron Devices.

[2] L. I. Rosier, "Surface States and Surface Recombination Velocity Characteristics of Si-SiO_2 Interfaces", IEEE Trans. Elec. Dev., ED-13, 260-268 (1966).

[3] M. Tanenbaum and D. E. Thomas, "Diffused Emitter and Base Silicon Transistors", Bell Syst. Tech. J., 35, 1-22 (1956).

[4] H. J. J. DeMan, "The Influence of Heavy Doping on the Emitter Efficiency of a Bipolar Transistor", IEEE Trans. Elec. Dev., ED-18, 833-834 (1971).

[5] R. J. Van Overstaeten, H. J. DeMan, R. P. Mertens, "Transport Equations in Heavily Doped Silicon", IEEE Trans. Elec. Dev., ED-20, 290-298 (1973).

[6] M. S. Mock, "On Heavy Doping Effects and the Injection Efficiency of Silicon Transistor", Solid State Electron., 17, 819-824 (1974).

[7] B. L. H. Wilson, "The Emitter Efficiency of Silicon Transistors", Solid State Electron., 20, 71-74 (1977).

[8] H. C. De Graaff, J. W. Slotboom, and A. Schmitz, "The Emitter efficiency of Bipolar Transistors: Theory and Experiment", Solid State Electron., 20, 515-521 (1977).

[9] F. A. Lindholm and C. T. Sah, "Fundamental Electronic Mechanisms Limiting the Performance of Solar Cells", IEEE Trans. Elec. Dev., ED-24, 299-304 (1977).

[10] C. T. Sah and F. A. Lindholm, "Carrier Generation, Recombination, Trapping, and Transport in Semiconductors with Position-Dependent Composition", IEEE Trans. Elec. Dev., ED-24, 358-362 (1977).

[11] P. M. Dunbar and J. R. Hauser, "A Study of Efficiency in Low Resistivity Silicon Solar Cells", Solid State Electron., 19, 95-102 (1976).

[12] J. R. Hauser and P. M. Dunbar, "Performance Limitations of Silicon Solar Cells", IEEE Trans. Elec. Dev., ED-24, 305-321 (1977).

[13] P. M. Dunbar and J. R. Hauser, "Theoretical Effects of Surface Diffused Region Lifetime Models on Silicon Solar Cells", Solid State Electron., 20, 697-701 (1977).

[14] F. A. Lindholm, A. Neugroschel, S. C. Pao, J. G. Fossum, and C. T. Sah, "Design Considerations for Silicon HLE Solar Cells", Record 13th Photovoltaic Specialists Conf., 1300-1305, June 1978, and A. Neugroschel, F. A. Lindholm, S. C. Pao, and J. G. Fossum, "Emitter Current Suppression in a High-Low-Junction Emitter Solar Cell Using an Oxide-Charge-Induced Electron Accumulation Layer", Appl. Phys. Lett., 33, 168-170 (1978).

[15] W. Shockley, Electrons and Holes in Semiconductors, Princeton, N. J.: Van Nostrand, 1950.

[16] P. T. Landsberg, R. W. MacKay, and A. D. McRonald, "The Parameters of Simple Excess Semiconductors", Proc. Phys. Soc. A, 476 (1950).

[17] J. W. Slotboom and H. C. DeGraaff, "Measurement of Bandgap Narrowing in Si Bipolar Transistors", Solid State Electron., 19, 857-862 (1976).

[18] J. R. Hauser, Final Report on NSF Grant GK-1615, 1969.

[19] H. P. D. Lanyon and R. A. Tuft (unpublished work).

[20] The average Auger recombination lifetime was calculated from a model similar to that of W. W. Sheng in "The Effect of Auger Recombination on the Emitter Injection Efficiency of Bipolar Transistors", IEEE Trans. Elec. Dev., Corres., ED-22, 25-27 (1975), in which the emitter is divided into two regions; one region has Shockley-Read-Hall recombination, and the surface region is dominated by Auger recombination.

[21] P. A. Iles and S. I. Soclof, "Effect of Impurity Doping Concentration on Solar Cell Output", Record 11th Photovoltaic Specialsts Conf., 19-24, Scottsdale, Arizona, 1975.

[22] F. A. Lindholm, A. Neugroschel, C. T. Sah, M. P. Godlewski, and H. W. Brandhorst, Jr., "A Methodology for Experimentally Based Determination of Gap Shrinkage and Effective Lifetimes in the Emitter and Base of P-N Junction Solar Cells and Other P-N Junction Devices", IEEE Trans. Elec. Dev., ED-24, 402-410 (1977).

[23] M. Wolf, "The Silicon Solar Cell Design Handbook", Record 9th Photovoltaic Specialists Conf., 53-60, Silver Spring, Maryland, 1972.

[24] J. G. Fossum and E. L. Burgess, "High-Efficiency $P^+N\,N^+$ Back-Surface-Field Silicon Solar Cells", Appl. Phys. Lett., 33, 238-240 (1978), and J. G. Fossum, R. D. Nasby, and E. L. Burgess, " Development of High-Efficiency $P^+N\,N^+$ Back-Surface-Field Silicon Solar Cells", Record 13th Photovoltaic Specialists Conf., 1294-1299, 1978.

Figure 1: The bandgap-narrowing reduction factor A(N) versus the electron (majority-carrier) concentration N for: (A) Lanyon-Tuft model, (B) Hauser model, and (C) Slotboom-De Graaff model.

Figure 2: The transit time τ_t versus the width of the emitter region W_E for S = 5×10^5 cm/sec and a gaussian profile with: no heavy doping (NHD), bandgap narrowing (Slotboom-De Graaf model) and Fermi-Dirac statistics (BGN+FD), bandgap narrowing (Slotboom-De Graaf model) only (BGN), and for a flat profile (NHD+FLAT).

Figure 3: The emitter saturation current density J_{PO} as a function of the surface recombination velocity S_p, for W_E = .25 μm, Fermi-Dirac statistics and bandgap narrowing included: (A) Lanyon-Tuft, (B) Hauser, and (C) Slotboom-De Graaf. For low values of S_p (less than about 10^4 cm/sec) the self-consistency test yields $\tau_t > \tau_p$ so the emitter current is then due to Auger recombination and may be larger than values reported above.

Figure 4: τ_t as a function of surface recombination velocity S_p for W_E = .25 μm, Fermi-Dirac statistics and bandgap narrowing are included: (A) Lanyon-Tuft, (B) Hauser, and (C) Slotboom-De Graaff.

Figure 5: τ_t versus W_E for S = 5×10^5 cm/sec. Fermi-Dirac statistics and bandgap narrowing are included: (A) Lanyon-Tuft, (B) Hauser, and (C) Slotboom-De Graaff.

Figure 6: V_{OC} versus S_p for W_E = .25 μm. Fermi-Dirac statistics and bandgap narrowing are included: (A) Lanyon-Tuft, (B) Hauser, and (C) Slotboom-De Graaff. In (D) heavy doping effects are not included. For low values of S_p (less than 10^4 cm/sec) V_{OC} is limited by the Auger-recombination current in the emitter because $\tau_t > \tau_p$ and V_{OC} may be lower than values reported above.

Figure 7: (a) The structure of p-n junction solar cell

(b) The three components of the emitter current: J_{P1}, J_{P2}, and J_{P3}.

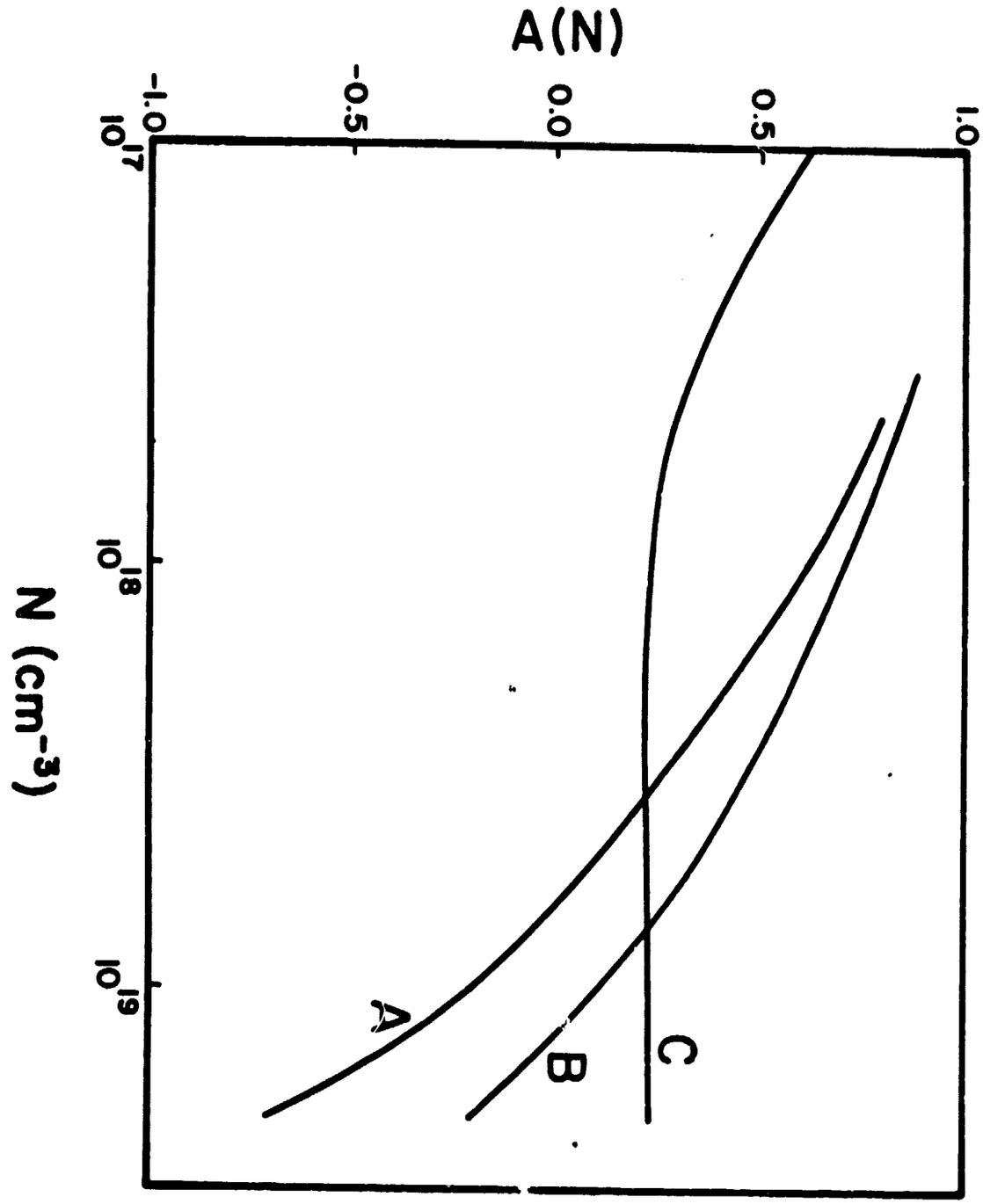

FIGURE 1

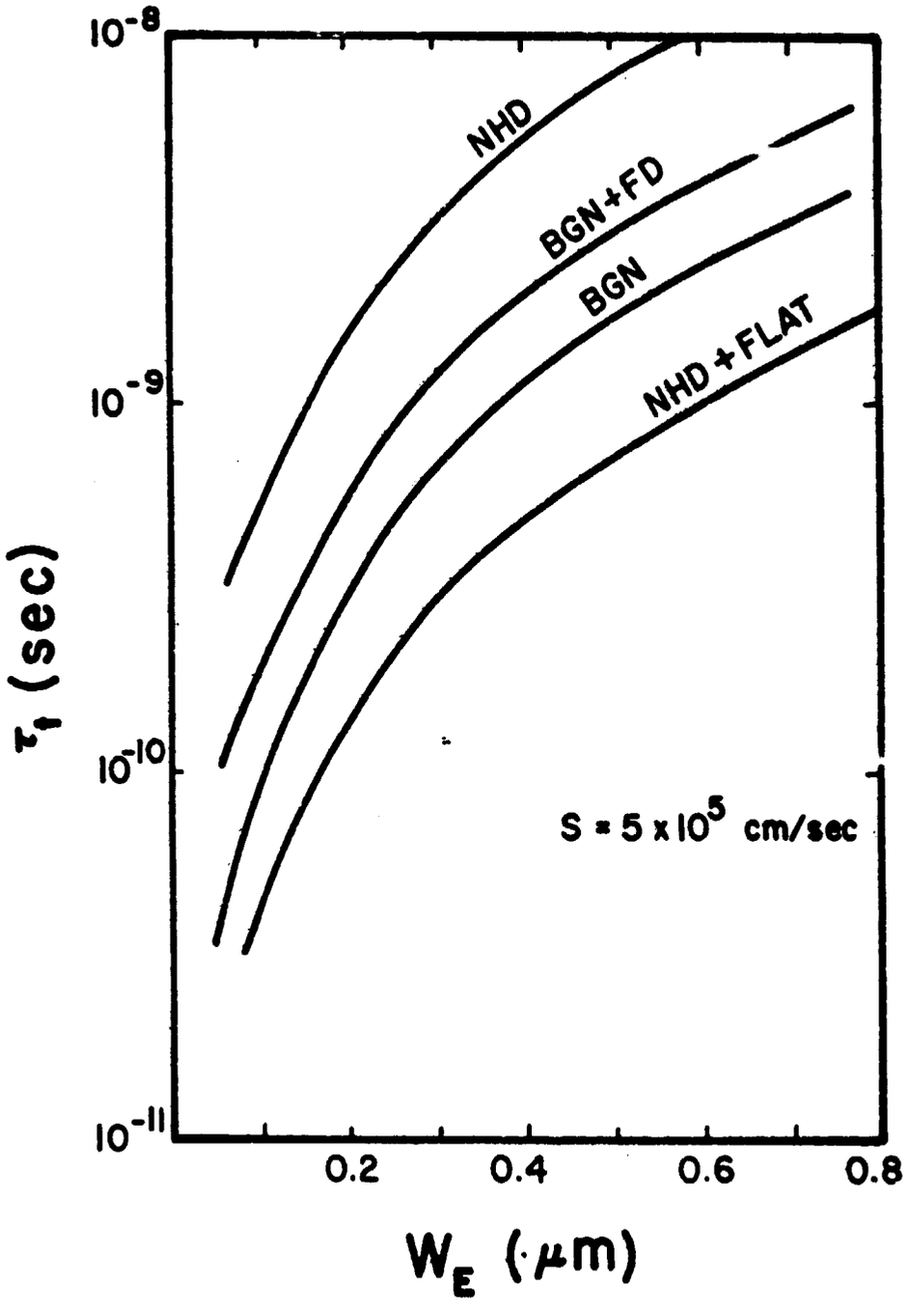
10^{-8}
10^{-9}
10^{-10}
10^{-11}
τ_t (sec)
NHD
BGN+FD
BGN
NHD+FLAT
S = 5 x 10^5 cm/sec
0.2
0.4
0.6
0.8
W_E (μm)

FIGURE 2

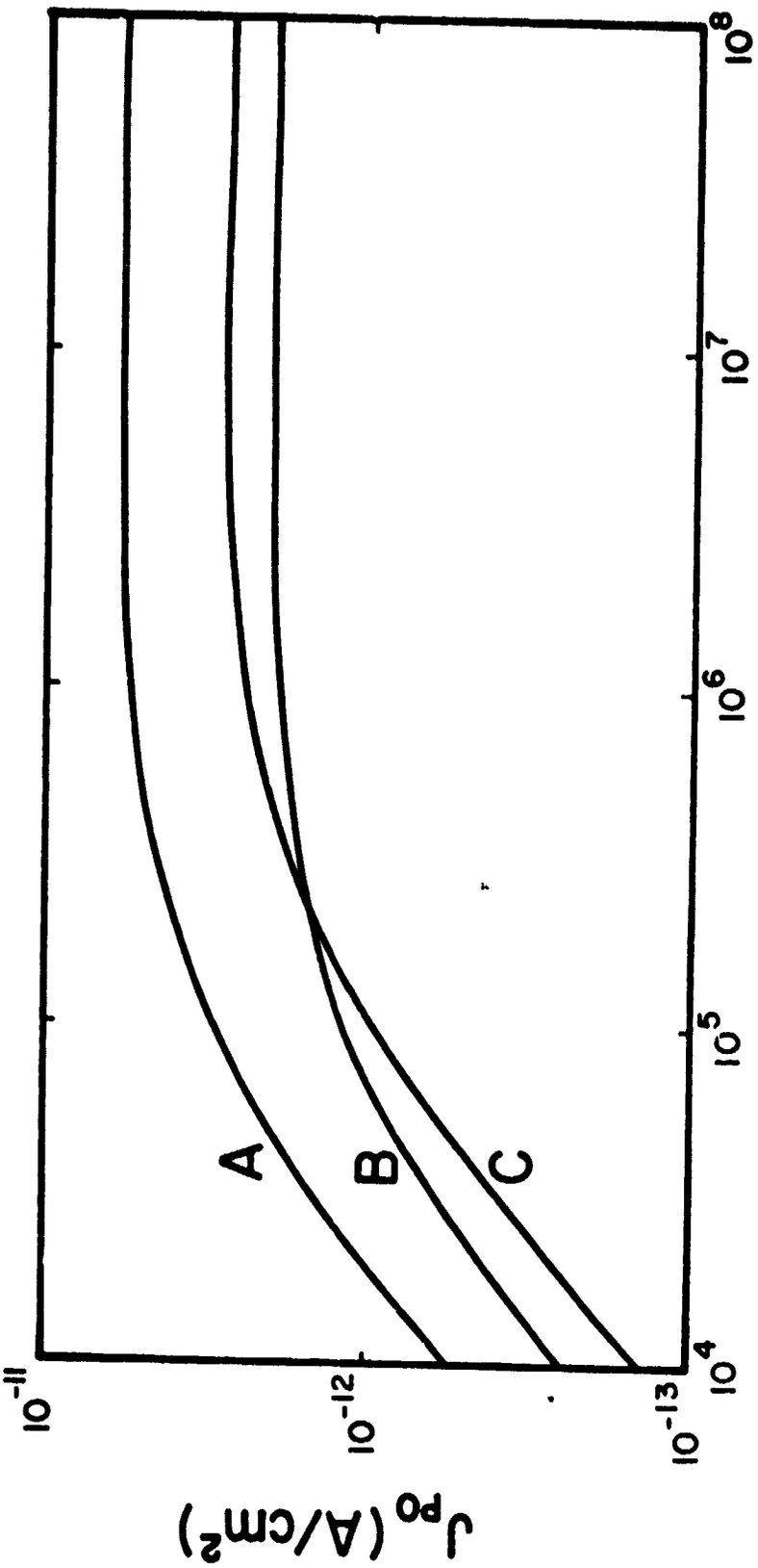

FIGURE 3

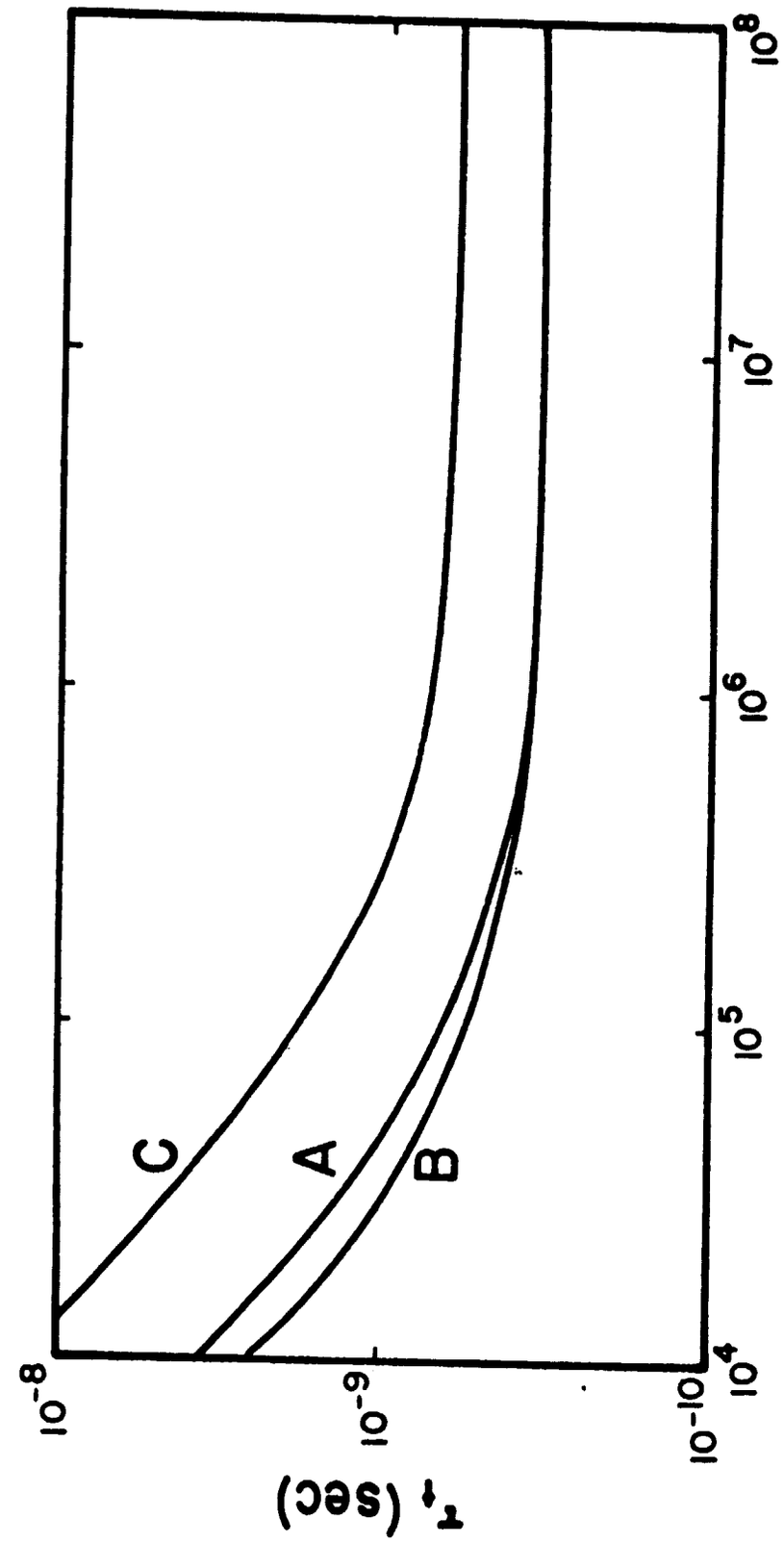

FIGURE 4

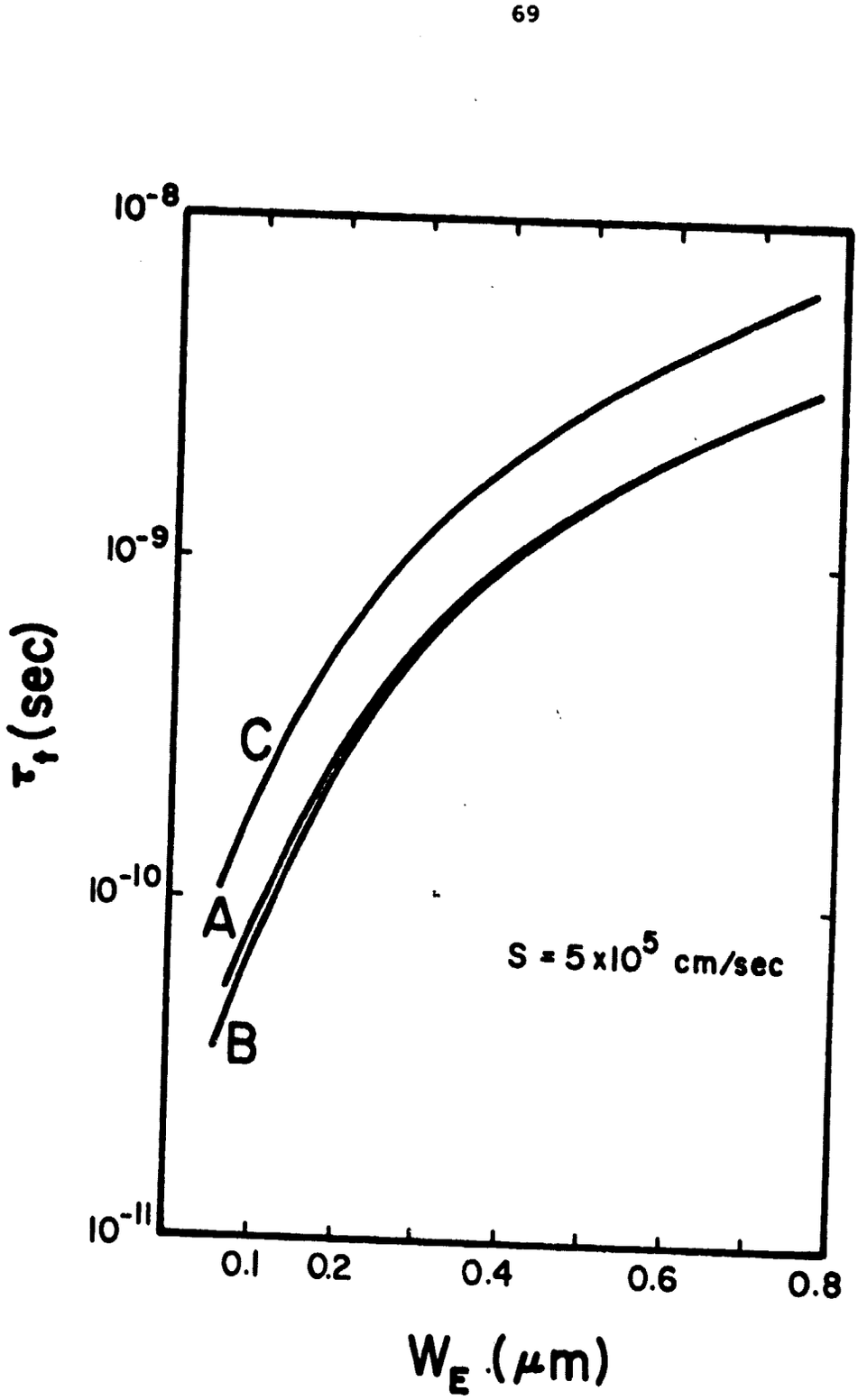
10^{-8}
10^{-9}
10^{-10}
10^{-11}
τ_t (sec)
C
A
B
$S = 5 \times 10^5$ cm/sec
0.1
0.2
0.4
0.6
0.8
W_E (μm)

FIGURE 5

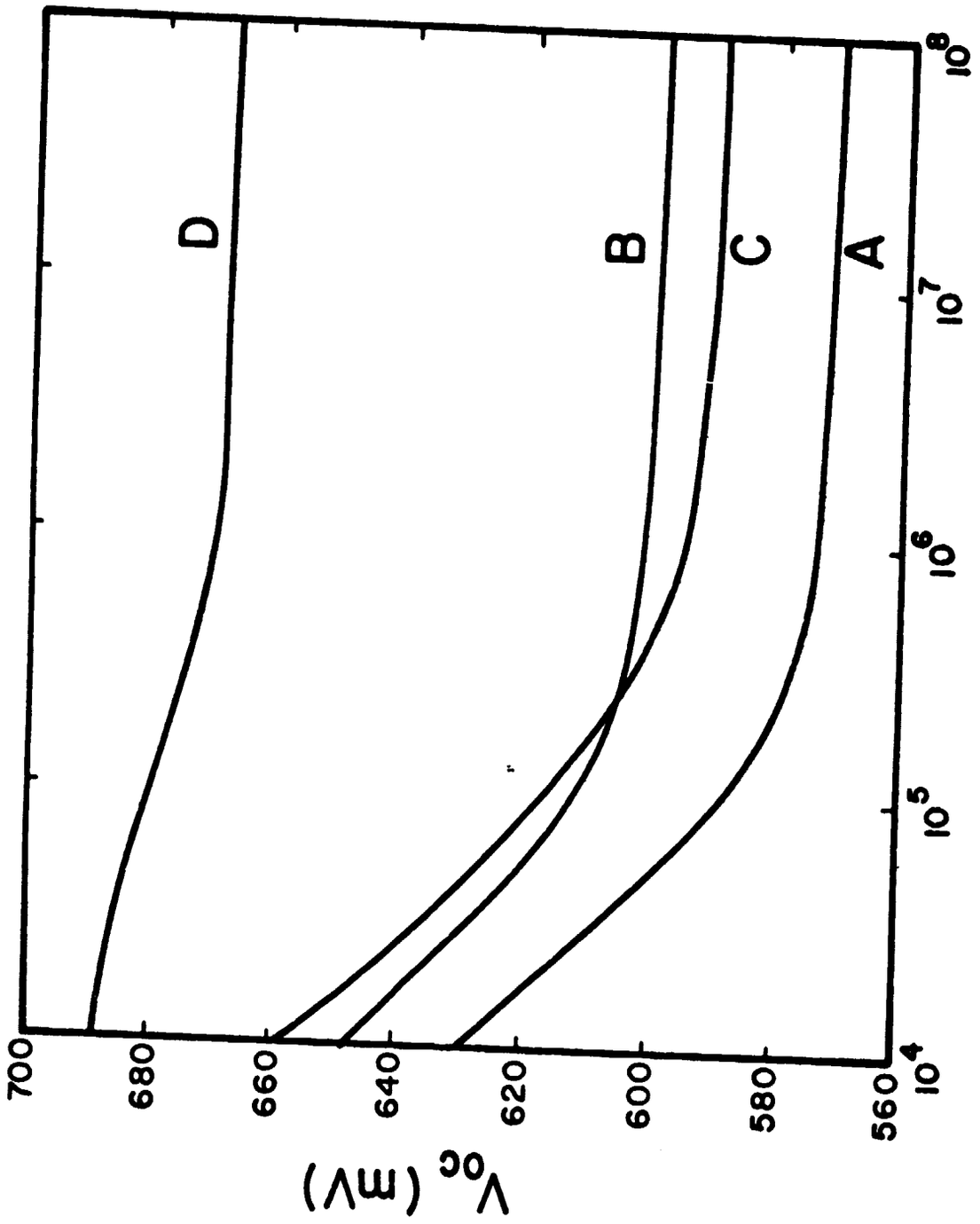
D
B
C
A
700
680
660
640
620
600
580
560
10^4
10^5
10^6
10^7
10^8
V_{oc} (mV)
S_p (cm/sec)

FIGURE 6

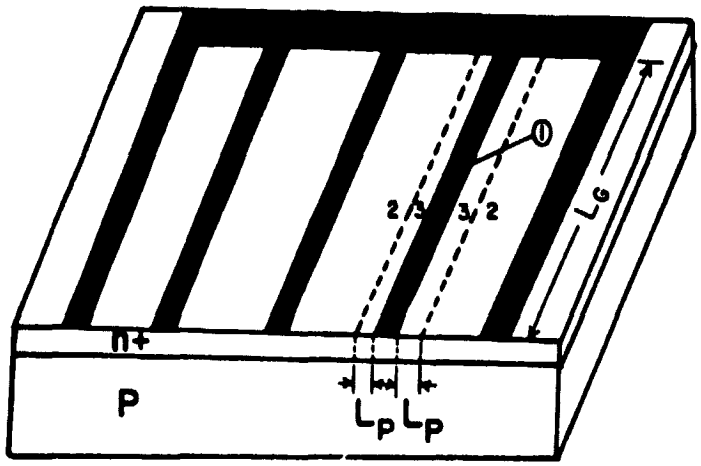
n+
P
L_P L_P
2/3
3/2
L_G

(a)

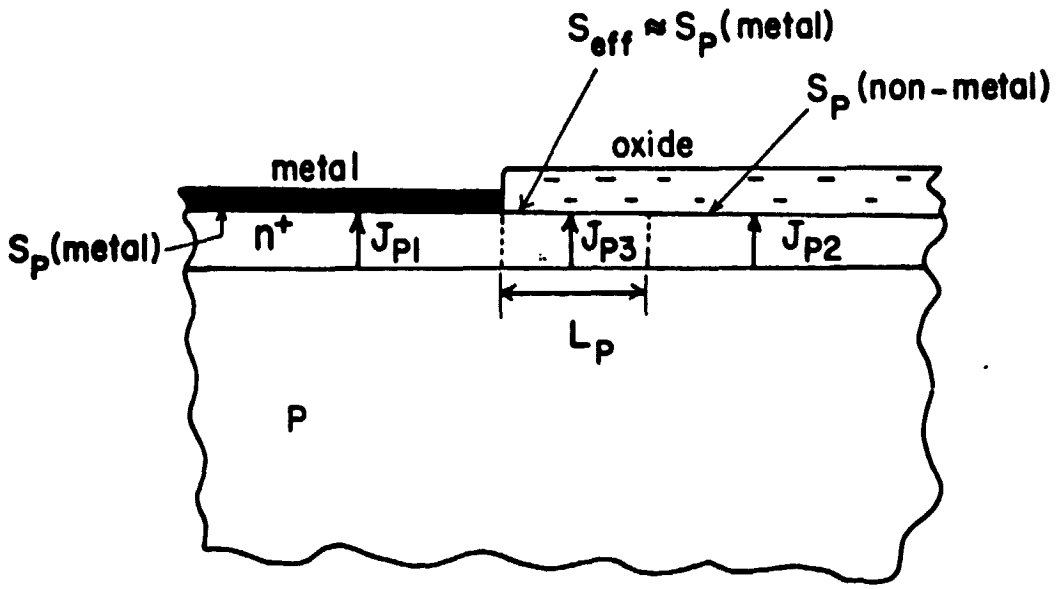
$S_{eff} \approx S_P$(metal)
S_P(non-metal)
oxide
metal
S_P(metal)
n+
J_{P1}
J_{P3}
J_{P2}
L_P
P

(b)

FIGURE 7

CHAPTER 4

HIGH-LOW-EMITTER SOLAR CELL

4.1 Introduction

As Brandhorst first noted [1] the power conversion efficiency η in silicon p-n junction solar cells is considerably less than the maximum theoretical value of η mainly because the open-circuit voltage V_{OC} is smaller than simple p-n junction theory predicts. Experiments [2] on n^+-p silicon cells have shown that this discrepancy in V_{OC} results from the dominance, in the non-illuminated cell, of the emitter recombination current J_E over the base recombination current J_B. In cells having base doping concentrations of the order of 10^{17} cm^{-3}, for which the largest values of V_{OC} are seen, J_E exceeds J_B by about an order of magnitude [2], rather than being several orders of magnitude less than J_B as is predicted by simple p-n junction theory. The excess J_E has been attributed to the mechanisms [3,4] of energy bandgap narrowing and lifetime degradation that accompany heavy doping concentrations in the n^+ emitter. The excess J_E may also arise, in part, from a large surface recombination velocity over the non-metallized portion of the surface.

To suppress J_E and thus raise the achievable values of V_{OC}, a new structure, the High-Low-Emitter (HLE) solar cell has been proposed and its performance has been calculated on theoretical grounds [5-7]. This device contains a high-low junction near an emitter surface of low

surface recombination velocity. In the second section of this chapter we outline the theory underlying HLE solar cell behavior; then we discuss early experimental results on test devices employing the HLE structure. In particular, we focus on one category of HLE solar cell: the Oxide-Charge-Induced (OCI) HLE solar cell in which an electron accumulation layer is used to form a high-low junction [7,8].

4.2 Physical Basis Underlying Emitter Current Suppression in HLE Solar Cells

As is illustrated in Fig. 4.1(a), the HLE cell differs from the conventional p-n junction solar cell in that it contains a high-low junction in the emitter. The mechanisms underlying the suppression of the emitter current resemble, in part, those which suppress base current in Back-Surface-Field (BSF) solar cells: as the injected minority carriers (holes) diffuse across the lightly-doped n region into the n^+ region, where the electron density is much higher, the partially reflecting boundary condition [9] at the high-low junction depresses the hole density near the emitter surface. In contrast to the BSF cell, however, in the HLE cell the emitter surface, which is close to the high-low junction, is designed to have a low surface recombination velocity S_p. The combination of low hole density and low S_p results in a suppression of the injected hole current.

In Fig. 4.1(b) we contrast the spatial distributions of the excess hole concentrations in the quasi-neutral emitters of two structures: one, an HLE structure, the other, a structure with no H-L junction and with a large value of S_p. In this comparison, it is assumed that the holes injected from the base into the emitter recombine mainly at the emitter surface (x=0). Figure 4.1(c) shows qualitatively the effect

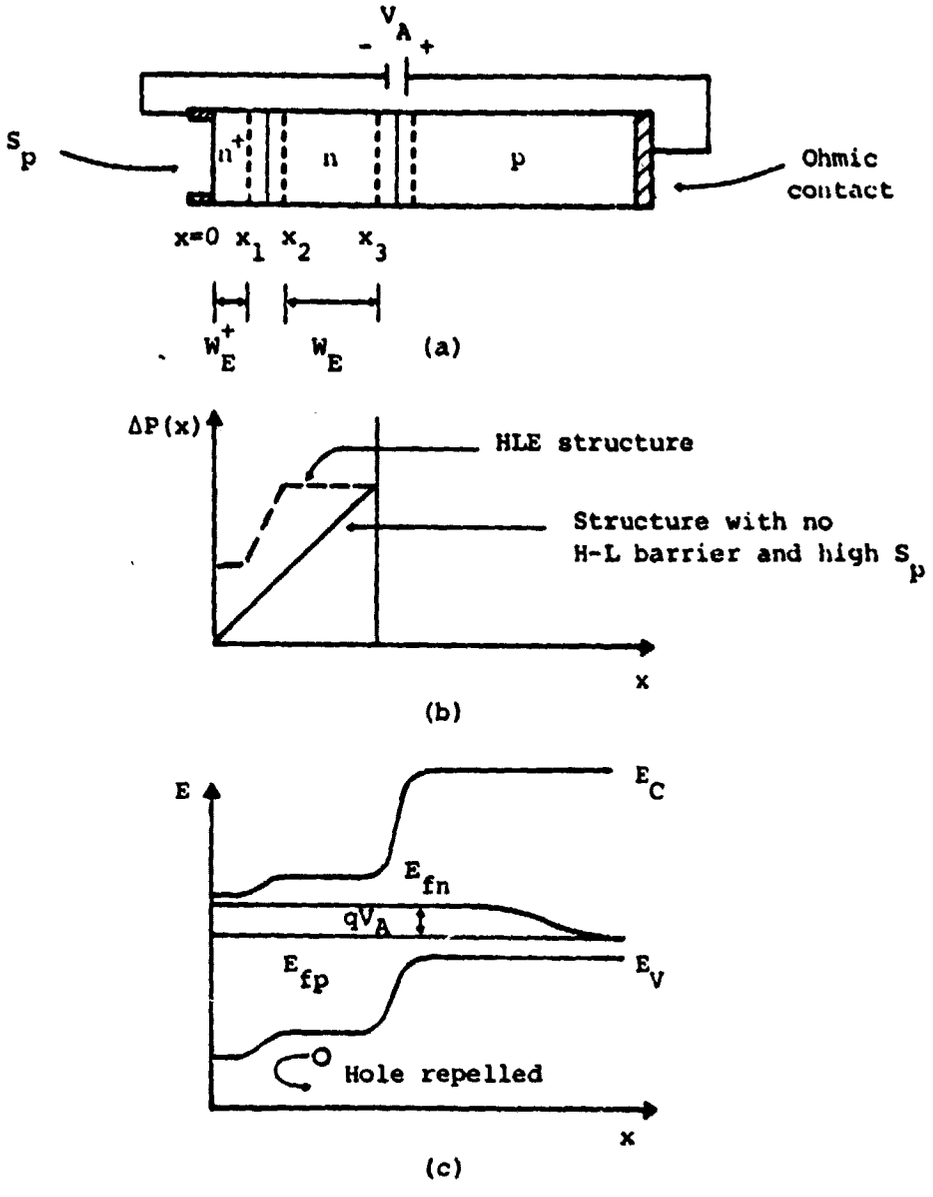

Figure 4.1 (a) High-Low-Emitter junction solar cell structure under external bias voltage V_A.

(b) Excess hole distribution in a HLE structure (dashed line) and in a structure with no H-L barrier and with high value of S_p (solid line).

(c) Energy band diagram showing the Coulomb repulsion of injected holes by the H-L barrier.

of Coulomb-force repulsion associated with the high-low barrier on injected holes in the vicinity of the high-low junction.

To study the emitter current in the HLE structure more quantitatively, we make use of the discussion in Chapter 3 for the Back-Surface-Field solar cells. Analogous to (3.1), the emitter current in HLE structure can be decomposed into two components: J_E^+, the current component due to recombination in the n^+ bulk and surface region and J_E, the current component due to recombination in the n bulk region. Using the same notations as in (3.1), we write the total emitter current $J_p(X_3)$ as

$$|J_p(X_3)| = q\Delta P(x_2)S_E + q\frac{[\Delta P(x_2)+\Delta P(x_3)]}{2}\frac{W_E}{\tau_p} \qquad (4.1)$$

where the first term on the right hand side represents J_E^+, the second term represents J_E, S_E is the effective recombination velocity for holes at $x = x_2$, and the geometrical variables x_2, x_3, and W_E are as defined in Fig 4.1(a).

For good cell performance both J_E and J_E^+ must be made small. The current J_E must be small so that the injected carriers can interact with the high-low barrier. This imposes the following conditions on the n region: (a) its hole lifetime must be long compared to the hole transit time across the n layer so that nearly all the holes injected from the base diffuse through to the high-low junction rather than recombining within the region, and (b) its doping concentration must be low enough (less than 10^{17} to 10^{18} cm^{-3}) to avoid the effects of energy band-gap narrowing and severe hole lifetime degradation. These considerations suggest that a 5 to 20 μm thick n-type epitaxial layer with resistivity in the range of 0.1 Ω-cm to 1 Ω-cm would be appropriate.

Note that higher conductivity offers the advantage of reducing the lateral component of series resistance.

We next investigate J_E^+, the recombination current component in the n^+ region. For concreteness in the discussion, we assume for now that the n^+ region is formed by a heavy doping concentration of donor atoms, resulting from diffusion or ion implantation or some other method of fabrication. A later discussion, in Section 4.3, generalizes to include the possibility that the large electron concentration in the n^+ region is formed without heavy doping as in the OCI-HLE solar cell.

For this diffused (or ion-implanted) HLE device, we assume the n^+ region to be thin enough that all the holes recombine mainly at the surface which can be characterized by a surface recombination velocity S_p. We further assume the quasi-neutral n^+ region to be field-free, as a result of the built-in electric field due to the doping gradient being balanced approximately by the quasi-field due to the gradient of the energy band-gap narrowing $\Delta E_G(x)$. Solution of the continuity equation for holes then yields [7].

$$|J_E^+| \simeq \frac{q\, n_{ie}^2(x_1)}{N_{DD}^+(x_1)} \left[\frac{1}{S_p} + \frac{1}{D_p/W_E^+}\right]^{-1} [\exp(qV_A/kT)-1] \qquad (4.2)$$

where D_p is the hole diffusivity, W_E^+ is the thickness of the quasi-neutral n^+ region, x_1 is the quasi-neutral region edge of the high-low junction nearest the surface, N_{DD}^+ is the doping concentration, and n_{ie}^2 is the effective intrinsic density squared which can differ from n_{io}^2, the intrinsic density squared for intrinsic silicon because of the effects of Fermi-Dirac statistics [10] and energy band narrowing [3,11].

In the field-free model for the n^+ region [10], note that

$$n_{ie}^2(x_1) / N_{DD}^+(x_1) = n_{ie}^2(x) / N_{DD}^+(x) \tag{4.3}$$

where x is any point in the n^+ region. This relation can simplify the quantitative use of (4.2) in analysis.

For a well passivated surface, S_p is low and often W_E^+ is thin enough that D_p/W_E^+ is much larger than S_p. Under this assumption, the total emitter current is

$$|J_p(x_3)| \approx \left[\frac{q\, n_{ie}^2\, S_p}{N_{DD}^+} + \frac{q\, n_{io}^2\, W_E}{N_{DD}\, \tau_p}\right] [\exp(qV_A/kT)-1] \quad . \tag{4.4}$$

Here we assume $\Delta P(x_2) \approx \Delta P(x_3) \approx n_{io}^2/N_{DD}$ where N_{DD} is the doping concentration in the n region.

Provided that the bulk recombination in the n-type region is negligible, the emitter current is then

$$J_p(x_3) \approx \frac{q\, n_{ie}^2\, S_p}{N_{DD}^+} [\exp(qV_A/kT)-1] \quad . \tag{4.5}$$

The same suppression would occur in a conventional n^+-p solar cell if all the holes were transported across the emitter to the surface and if the surface were passivated to reduce S_p. The advantage of the HLE structure is that the n^+ layer of the HLE cell can be made very thin ($\sim$ 1000 Å) with lower doping concentration to decrease the heavy-doping effects. The lower sheet resistance of the n^+ layer will be compensated by the parallel resistance of the n-type epitaxial layer. The low-doped emitter epitaxial region will contribute significantly to the short-circuit current, since for low S_p most of the optically

generated carriers will be collected by the p-n junction. The low doping of the n region is consistent with long minority-carrier lifetime which enables the achievement of a high collection efficiency.

In the Oxide-Charge-Induced HLE structure, which we will study in the following section, the emitter current is suppressed so low by the surface and the high-low barrier that the base current J_B alone determines the dark current.

4.3 Oxide-Charge-Induced HLE Solar Cell: Structure, Fabrication, and Performance

4.3.1 Structure

As is shown in Fig. 4.2, the high-low junction in the emitter results from an electron accumulation layer induced in the n-type epitaxial emitter region by a positive oxide charge Q_{OX}. The charge Q_{OX} is created near the silicon-silicon dioxide interface during a low-temperature oxygen heat treatment [12]. Experiments on MOS capacitors indicate that the positive oxide charge Q_{OX} resides within about 300 Å from the silicon-silicon dioxide interface and strongly depends on the last high temperature process and the crystal orientation [12,13]. For <111> wafers annealed in 700°C dry oxygen, Q_{OX} is found to be about $5.5\times10^{11}/cm^2$ [12,13]. The total charge accumulated near the silicon surface is approximately Q_{OX}. The electron distribution is described by MOS theory [26], and most of the electrons in the accumulation layer reside within about three extrinsic Debye lengths from the surface. For the above value of Q_{OX}, the electron surface concentration is about 9.3×10^{17} cm^{-3} for ρ_{epi}=1.5 Ω-cm and about 1.2×10^{18} cm^{-3} for ρ_{epi}=0.1 Ω-cm. To assure a good ohmic contact, a shallow phosphorous diffusion is

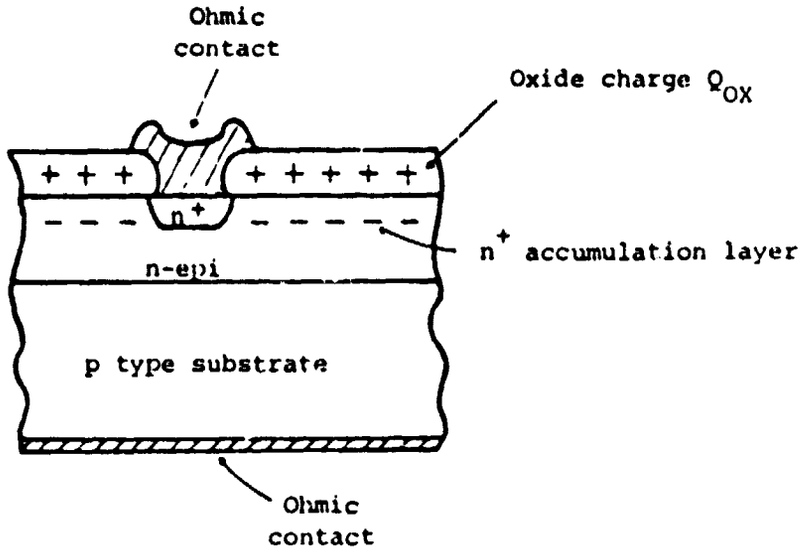

Figure 4.2 Cross section of an oxide-charge-induced high-low-emitter (OCI-HLE) solar cell. Electron accumulation layer is induced by a positive oxide charge Q_{OX}.

made under the metallized portion of the top surface area. This n^+ diffusion also provides a high-low barrier and a small effective surface recombination velocity [9] for holes. The p-type base has a doping concentration $N_{AA} \simeq 5 \times 10^{17}$ cm^{-3}, which approximately minimizes J_B in a cell without a back-surface field [1].

From a device performance point of view, the oxide-charge-induced H-L structure of Fig. 4.2 is an attractive realization of the HLE solar cell because it avoids a high concentration of donor impurity atoms in the thin H layer near the surface. This diminishes some sources of degrading heavy-doping effects [3], such as some mechanisms that give rise to band-gap narrowing [14] and hole lifetime degradation in the H layer, and it can also help the achievement of low values of surface recombination velocity. The avoidance of a diffusion step to form a highly-doped H layer eliminates, over the nonmetallized portion of the surface, the diffusion of unwanted impurities and vacancies into the silicon along with the donor atoms. These advantages can result without the occurrence of a large lateral component of the series resistance R_s, and consequent degradation of the fill factor FF [15], because the thickness and doping concentration of the L portion of the H-L junction can be adjusted to supply the needed lateral conductance. For applications in concentrated sunlight, this is particularly important.

The preceding section contains expressions for the dark emitter current for the diffused (or ion-implanted) HLE. These were based on a field-free model of the n^+ region in which the built-in electric field and the quasi-field nearly cancelled one another. For the OCI-HLE solar cell, however, this is an inappropriate model because the gradient of the energy band gap that produces the quasi-field is small for the

low values ($\sim 10^{18}$ cm^{-3}) of electron concentration induced at the surface while the electron concentration can change by several orders of magnitude in a Debye length thereby producing a large built-in electric field. To derive an expression for the dark emitter current in the OCI-HLE cell, note that the large electron concentration and the desired suppressed hole current suggest that the quasi-Fermi levels for both electrons and holes are nearly flat throughout the emitter region, as Fig. 4.1(b) indicates. Then by multiplying together the expressions for the electron and hole densities (in terms of the qausi-Fermi levels), one finds the excess hole density at the surface. If the injected holes recombine mainly at the surface, which is a preferred design for the reasons indicated in the preceding section, then the surface excess hole density times qS_p gives the magnitude of the dark emitter current:

$$|J_p| = qS_p(n_{ies}^2/N_s) \quad [\exp(qV_A/kT)-1] \tag{4.6}$$

where N_s is the electron concentration at the surface and n_{ies}^2 is the effective intrinsic density squared at the surface. It can differ from n_{io}^2 even though the electron concentration N_s is low because of the effects of minority-carrier screening by the majority carriers [14,16] and of Fermi-Dirac statistics [10]. Note that (4 6) is essentially the same as (4.5) for the field-free model of the used (or ion-implanted) HLE cell. Indeed, an alternate, but not equivalent, derivation of (4.5) could follow the reasoning directly above employing the near flatness of the quasi-Fermi levels in the emitter region.

4.3.2 Fabrication

The fabrication of the OCI-HLE solar cell is simple. A major portion of the devices fabricated in this study are made using the following basic processing steps:

1. Wafer cleaning.
2. Thermal oxidation of silicon surfaces.
3. Defining ohmic contact windows on front surface using photolithographic process (mask #1).
4. Phosphorous diffusion through contact windows.
5. Low temperature oxygen annealing.
6. Etching oxides over contact windows.
7. Metal deposition on front surface.
8. Defining metal grid pattern on front surface by photolithographic process (mask #2).
9. Lapping the back surface.
10. Metal deposition on back surface.
11. Annealing the wafer in forming gas (10% hydrogen, 90% nitrogen).

Details regarding processing temperature and time for devices fabricated using the above schedule are summarized in Appendix II and Appendix III. We have also fabricated some devices using processing schedules that are slightly different from the above and they are also listed in Appendix III. The layout of masks used are shown in Appendix IV.

4.3.3 Performance of OCI-HLE Cells

We now discuss the experimental results of process runs number 25 and 26. The starting material for run #25 is <111> p-type Czochralski-grown wafer with a 10 μm, 1.4 Ω-cm n-type arsenic-doped epitaxial

layer. The p base is boron-doped with a resistivity of 0.14 Ω-cm and a thickness about 300 μm. The wafer was oxidized in dry oxygen with 0.3% trichloroethylene (TCE) at 1100°C for three hours to grow a 2500 Å thick oxide. The temperature of 1100°C was chosen for this cell to assure a good quality oxide and a low value of surface recombination velocity. Holes were opened in the oxide for a phosphorous diffusion done at 900°C for 15 minutes. The phosphosilicate glass was etched off and the wafer was heat treated in dry oxygen for two hours at 700°C to increase the oxide charge Q_{OX} [12]. The thin oxide over the contact opening was then etched and the field oxide was thinned to 1100 Å to improve the antireflection properties. An aluminum grid pattern was defined photolithographically on the front surface. The back surface was lapped in silicon carbide abrasive powder, and aluminum was evaporated on the back surface. The wafer was then annealed in forming gas at 450°C for 15 minutes. This serves to anneal the surface states at the silicon-silicon dioxide interface [17] as well as to make the aluminum-silicon contact ohmic. The wafer was then scribed into cells of different sizes. It is found that the scribing process introduces crystal damages at the periphery of the cell. The effect manifests itself as an edge recombination current in the current-voltage characteristics of the cell. Although the magnitude of this current is insignificant at higher voltages (> 0.6 V), its presence at lower voltages can often decrease the fill factor and hinder proper data analysis, for example, the determination of the quasi-neutral saturation current [18]. To eliminate this current component, all finished cells are etched in CP4 solution (3 parts hydrofluoric acid, 5 parts nitric acid, 3 parts acetic acid) for 10 minutes. The front

and back surfaces of the cells are protected by wax while the edges are left clear of wax during the etching.

The base diffusion length L_n, measured using the X-ray excitation method [19] was $L_n \approx 20$ μm. Measurement of the dark I-V characteristics shows that the ideal saturation current (determined by subtracting the space-charge-region recombination current [18]) is 2.9×10^{-13} Amp/cm^2 at 294.8°K. The corresponding base saturation current at this temperature, $q\, n_{io}^2\, D_n/(N_{AA} L_n)$, is 2.8×10^{-13} Amp/cm^2. This demonstrates that $J_E << J_B$. Thus the open-circuit voltage V_{OC} is determined mainly by J_B in this device. The results of the measurements show further that the emitter saturation current J_{E0} is suppressed to less than about 1.5×10^{-14} Amp/cm^2, assuming an experimental uncertainty of 5%. This current component corresponds to a voltage, $kT/q \ln(J_{SC}/J_{E0}) > 720$ mV, for a short-circuit current density J_{SC} of 35 mA/cm^2 (measured in this device). Thus J_E is suppressed to values so low that it presents no barrier to the achievement of $V_{OC} \approx 700$ mV, which is the maximum value of V_{OC} predicted by classical theory for a 0.1 Ω-cm base resistivity for Air-Mass-Zero (AM0) illumination.

The experimental setup for the V_{OC} and J_{SC} measurements is shown in Fig. 4.3. The light source is a General Electric 300 watt ELH lamp. The standard cell is a diffused HLE solar cell which has $J_{SC} \approx 36.7$ mA/cm^2 and $V_{OC} \approx 620$ mV at 25°C under AM0 conditions as measured by NASA Lewis Research Center. The value of J_{SC} for the standard cell, as well as for all cells we measured, are calculated on an per-effective-area basis.

For the V_{OC} measurement, both standard and test cell are placed side by side and the intensity of the light source is adjusted by a

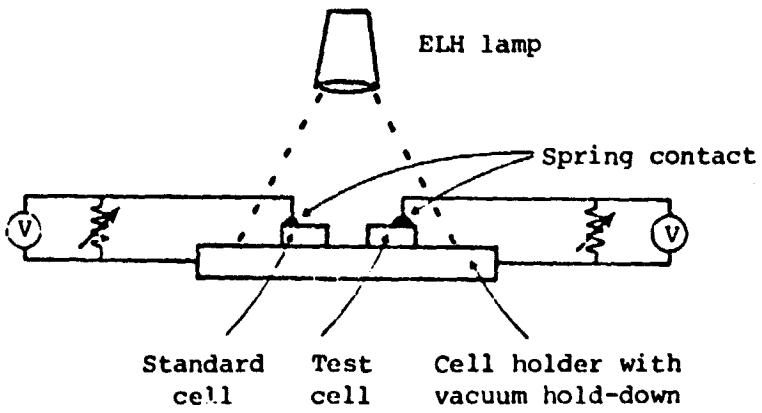

Figure 4.3 Experimental setup for V_{OC} and J_{SC} measurement.

variac such that V_{OC} of the standard cell is 620 mV. A reading on the test device is then taken. This value of V_{OC} is then the V_{OC} of the test cell at 25°C. This method works even when the ambient temperature is slightly different from 25°C since the change in V_{OC} with temperature is mainly due to the change of n_{io}^2 for both the standard and the test device. Likewise, for the J_{SC} measurement, the J_{SC} of the test device, as measured by a high impedance voltmeter across the 1 Ω resistor, is taken when the short-circuit current in the standard cell corresponds to a value of 36.7 mA/cm^2. The experimental accuracy is about ± 3mV for V_{OC} and ± 0.3 mA/cm^2 for J_{SC}, determined by comparing with the measurements done at NASA Lewis Research Center on the same devices.

The open-circuit voltage measured on devices of Run #25 is V_{OC} = 627 mV at 25°C and AM0 illumination, the short-circuit current density is J_{SC} = 35.5 mA/cm^2.

For Run #26, the starting material is different from that of Run #25. It is a <111> p type Czochralski-grown wafer with a 10μm, 0.1 Ω-cm n-type arsenic-doped epitaxial layer. The p-type substrate is boron-doped with a resistivity of 0.1 Ω-cm. The processing schedule for Run #26 is summarized in Appendix III. For this device, the emitter current again is completely suppressed. The measured V_{OC} is 634 mV at 25°C and J_{SC} is 32.8 mA/cm^2. Although the base diffusion length for these devices is only about 13 μm, the higher doping concentration and lower electron diffusivity reduce the base recombination current so that V_{OC} is higher than that of Run #25. The smaller value of J_{SC} is probably due to the heavier-doped epitaxial layer and a shorter base diffusion length.

Although the emitter current is suppressed in these devices, the results suggest that if the base diffusion length of these wafers can be improved, better cell performance can be expected. One approach would be to modify the fabrication procedures, particularly the higher temperature steps, to achieve a longer base diffusion length. Another approach would be to obtain better quality starting material. We will discuss these approaches in the next section.

4.4 Fabrication Considerations for OCI-HLE Junction Solar Cells

In Section 4.3 we have discussed the experimental results of process runs #25 and #26 which were the first runs made. It is noted that the degrading effects of heavy doping concentration and large surface recombination in the emitter region have been avoided in the OCI-HLE junction solar cell so that the open-circuit voltage in these cells is determined primarily by the base recombination current. However, the base minority-carrier lifetime in these devices is more than an order of magnitude lower than that of conventional n^+-p solar cells fabricated on substrate materials with about the same doping concentration. Diffusion lengths in the substrates of wafers used in Run #25 and #26 before processing were about 50 μm and 25 μm respectively, compared to a diffusion length of about 100 μm measured on some 0.1 Ω-cm substrates without the epitaxial layer. The low values of lifetime observed in these epitaxial wafers is probably due in part to the poor starting substrate, and to the defects or impurities introduced into the substrate during the epitaxial growth. The introduction of stacking faults during the initial high temperature oxidation can also reduce the bulk lifetime.

In this section we discuss the results of a sequence of device runs that employ fabrication schedules designed to improve the bulk minority-carrier lifetime compared to the schedules used for Run #25 and #26. These methods include the use of phosphorous gettering for metallic impurity removal [20] (Run #27), lower oxidation temperature (Run #31, #32), slow cooling of wafers after high temperature processes (Run #35, #36), and prolonged high temperature oxidation in the presence of chlorine compounds for annihilation of oxidation-induced stacking faults [21-23] (Run #48). Not all of these methods are suitable for the OCI-HLE solar cell fabrication since some of these processes may cause degradation in the emitter region, such as an increase in surface recombination velocity. The purpose of this study is to implement the most compatible method to improve the open-circuit voltage of the device. The relevant descriptions of the epitaxial wafers used for these runs are listed in Appendix III.

To find the bulk lifetime of the starting material, measurements were performed utilizing the existing p-n junction between the epitaxial layer and the substrate (Run #28). A low temperature n^+ phosphorous layer was diffused into the epitaxial wafer. This provides a better electrical contact to the lightly-doped epitaxial layer. The n^+ layer at the back side was removed and ohmic contacts at both surfaces of the wafer were created by evaporating Ti-Ag to both surfaces. Several 1 cm x 1 cm diodes were scribed from the middle of the wafer and the edges were etched in CP4 solution. Diffusion lengths in these devices were measured using the X-ray irradiation technique. The results were $L_n \approx 50$ μm for the 0.15 Ω-cm bulk material and $L_n \approx 25$ μm for the 0.1 Ω-cm material.

We now discuss the results of Run #27, 31, 32, 35, 36, and 48. The starting material of Run #27 is the same as Run #26 and except for an additional phosphorous gettering step the two runs are identical. The bulk diffusion length measured is about 15 μm, which is about the same as that for Run #26. While phosphorous gettering is known to result in significant improvement of bulk lifetime in lightly-doped materials [24], the ineffectiveness of this method to improve the bulk properties of these heavier-doped substances suggests that metallic impurities are not the dominant factors limiting the bulk lifetime in these materials. The result is consistent with the observed decrease in bulk diffusion length with higher substrate doping concentrations [25].

Run #31 and #32 investigate the possibility of improving bulk lifetime using lower oxidation temperatures. The main differences between these runs and the previous ones are the 900°C wet oxidation step (Run #31) and the 800°C dry oxidation step (Run #32). Details of the fabrication schedule are summarized in Appendix III. The diffusion lengths measured on these devices are low in comparison with that of Run #28. The open-circuit voltages of these devices are also low. Analysis of dark I-V characteristics [18] shows that the recombination current in the emitter region is significant. The results are displayed in Table 4.1. The low values of open-circuit voltages observed suggests the presence of a high density of surface states at the silicon-silicon dioxide interface as indicated by a control MOS capacitor made on 1 Ω-cm n-type wafers as shown in Fig. 4.4.

In Run #35 the epitaxial wafers are cooled slowly in nitrogen after the 1100°C oxidation and the 850°C phosphorous diffusion. In

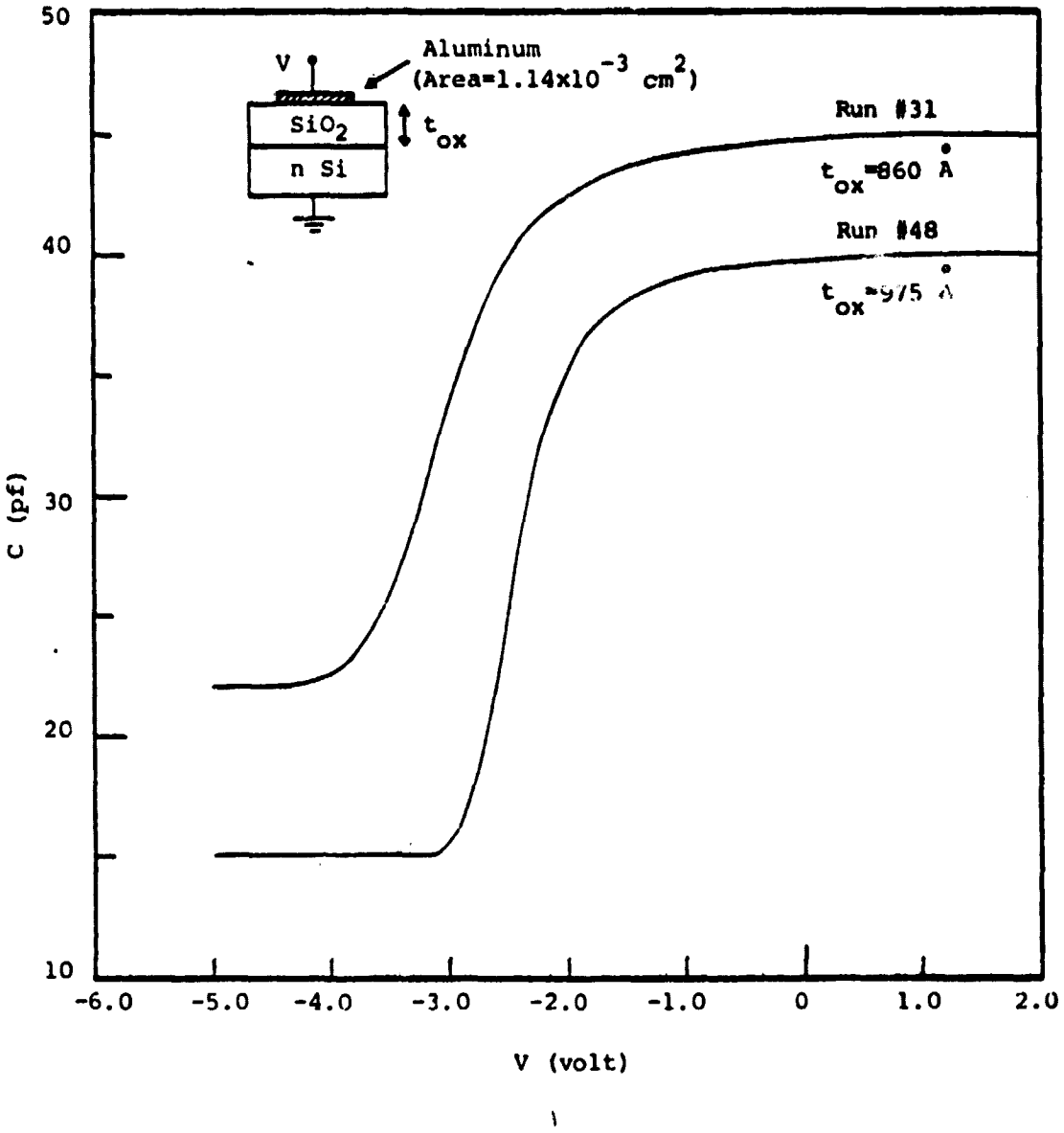

Figure 4.4 C-V plot for control MOS capacitor of Runs #31 and #48.

Run #36 the wafers were cooled in an oxygen ambient. For devices of Run #35, the diffusion lengths measured were $L_n \approx 54$ μm for cells fabricated on 0.15 Ω-cm substrate and $L_n \approx 21$ μm for cells fabricated on 0.1 Ω-cm substrate. If the emitter recombination current is suppressed and the space-charge region recombination current is small, the open-circuit voltages of these devices would be about 660 mV and 650 mV at 25°C respectively. However, the observed V_{OC} is only 604 mV for cells made on the 0.15 Ω-cm material and 623 mV for cells made on the 0.1 Ω-cm material. Analysis of dark I-V characteristics reveals that the emitter recombination current in these devices constitutes about 90% and 60%, respectively, of the total quasi-neutral region recombination current. The results again suggest the influence of surface states associated with low temperature oxides [12,13]. The diffusion length for devices of Run #36 is $L_n \approx 35$ μm for the 0.15 Ω-cm material. The degradation in L_n is probably due to prolonged heat treatment in oxygen.

In Run #48 the wafers are oxidized in 1150°C for 5 hours with 1.5 ℓ/min dry oxygen with 0.3% TCE. An oxidation time of five hours was chosen with the intent to suppress the oxidation-induced stacking faults (OISF) [21,22]. Following the standard n^+ contact diffusion the phosphosilicate glass is etched off and the wafers are annealed in dry oxygen at 700°C for 2 hours. The diffusion lengths for this run are $L_n \approx 50$ μm for the 0.15 Ω-cm material and $L_n \approx 23$ μm for the 0.1 Ω-cm material. Although we have obtained long diffusion lengths for these materials, the open-circuit voltages of these devices are still low. They are 606 mV and 622 mV respectively. Capacitance-Voltage measurement on control MOS capacitors made on 1 Ω-cm n-type wafers indicates the surface state density is low, as would be expected for

higher temperature oxides (Fig. 4.4). The low values of V_{OC} are due to an inadequate density of oxide charge to induce a sufficient high-low barrier ($Q_{OX}/q \approx 4.2 \times 10^{11}$ cm^{-2}). In Run #51 we repeat Run #48 except the wafers are annealed in dry oxygen at 700°C for 12½ hours to allow more time to form the oxide charges ($Q_{OX}/q \approx 5.5 \times 10^{11}$ cm^{-2}). The results are $L_n \approx 34$ μm, $V_{OC} \approx 635$ mV for the 0.15 Ω-cm material and $L_n \approx 16$ μm, $V_{OC} \approx 639$ mV for the 0.1 Ω-cm material. We have also fabricated devices using epitaxial wafers with heavily-doped (0.025 Ω-cm) substrates. V_{OC} of 640 mV has been obtained. These results emphasize the importance of the properties of the front surface. Although the values of L_n are smaller for Run #51 than Run #48, values for V_{OC} are higher due to a more effective high-low barrier.

We have discussed several approaches of OCI-HLE solar cell fabrication to improve the open-circuit voltage. It is important that these devices have a well passivated surface with low recombination velocity as well as long diffusion length in the substrate for good cell performance. Oxidation in dry oxygen at elevated temperatures with TCE, followed by low temperature dry oxygen annealing was found to be the best approach for the silicon materials used in this study. In Table 4.1 we summarize all pertinent results obtained for the devices under study. In Table 4.2 we characterize the surface properties of the OCI-HLE solar cells under study. The oxide charge density Q_{OX}/q is obtained from the flatband voltage shift in the C-V plot for control MOS capacitors, the electron concentration at the surface N_s follows from classical MOS theory [26], and the surface recombination velocity S_p is evaluated using (4.6).

Table 4.1 Experimental Results of OCI-HLE Solar Cells Performance. Data with Asterisk Were Measured at NASA Lewis Research Center.

Run #	Wafer	Substrate Resistivity (By Four Point Probe Method) ρ_{base} (Ω-cm)	Device Area $A(cm^2)$	Non-Metallized Surface Area $A_e(cm^2)$	Measurement Temperature T(K)
25	9900AP	0.14	0.99	0.75	294.8
26	MONSANTO	0.10	1.00	0.83	293.2
27	MONSANTO	0.10	0.72	0.58	293.4
28	9900AQ	0.14	1.00	0	
	MONSANTO	0.10	1.00	0	
31	9900AP	0.14	1.65	1.30	295.2
	9900AQ	0.14	1.59	1.26	294.8
32	9900AQ	0.15	0.90	0.77	292.6
35	9900AP	0.14	0.91	0.76	293.4
	MONSANTO	0.10	1.89	1.56	293.5
36	9900AP	0.14	1.21	0.97	293.4
48	9900AP	0.14	0.84	0.68	292.7
	MONSANTO	0.10	0.98	0.79	293.4
51	9900AP	0.14	0.95	0.77	292.6
	MONSANTO	0.10	0.95	0.80	293.5
	MOTOROLA	0.024	1.91	1.68	293.1

Table 4.1 (extended)

L_n (μm)	J_{QNO} (Amp/cm^2)	J_{BO} (Amp/cm^2)	J_{EO} (Amp/cm^2)	$V_{OC}\|_{25°C}$ (mV)	I_{SC}/A_e (mA/cm^2)	Fill Factor
20.1	2.86×10^{-13}	2.83×10^{-13}	$<1.5\times10^{-14}$	627*	35.5*	0.703*
13.5	1.90×10^{-13}	1.90×10^{-13}	$<1.0\times10^{-14}$	634*	32.8*	0.801*
14.1	1.87×10^{-13}	1.87×10^{-13}	$<1.0\times10^{-14}$	635	32.8	
49.4						
26.6						
19.3	1.40×10^{-12}	2.94×10^{-13}	1.11×10^{-12}	584	32.2	
9.6	3.39×10^{-12}	5.94×10^{-13}	2.80×10^{-12}	566	29.4	
26.3	7.50×10^{-13}	1.61×10^{-13}	5.89×10^{-13}	603	28.7	
53.5	7.93×10^{-13}	8.36×10^{-14}	7.10×10^{-13}	605	35.2	
21.0	3.16×10^{-13}	1.28×10^{-13}	1.88×10^{-13}	623	31.3	
34.5	7.05×10^{-13}	1.30×10^{-13}	5.75×10^{-13}	602	33.6	
49.9	5.62×10^{-13}	7.83×10^{-14}	4.84×10^{-13}	606	34.6	
22.7	3.85×10^{-13}	1.16×10^{-13}	2.69×10^{-13}	622	32.7	
33.8	1.73×10^{-13}	1.20×10^{-13}	5.30×10^{-14}	635*	36.0*	0.717*
17.0	2.13×10^{-13}	1.60×10^{-13}	5.30×10^{-14}	639*	34.3*	0.806*
∿2.5	1.25×10^{-13}	4.00×10^{-14}	8.50×10^{-14}	640*	29.1*	0.739*

C-2

Table 4.2 Characterization of Surface Properties of OCI-HLE Solar Cells Fabricated.

Run #	Wafer	Q_{OX}/q (cm^{-2})	N_s (cm^{-3})	S_p (cm /sec)*
25	9900AP	4.8×10^{11}	6.9×10^{17}	8.7×10^{2}
31	9900AP	5.8×10^{11}	1.0×10^{18}	9.1×10^{4}
	9900AQ	5.8×10^{11}	1.0×10^{18}	2.4×10^{5}
32	9900AQ	3.3×10^{11}	3.3×10^{17}	2.4×10^{4}
35	9900AP	5.9×10^{11}	1.1×10^{18}	6.2×10^{4}
	MONSANTO	5.9×10^{11}	1.3×10^{18}	2.6×10^{4}
36	9900AP	8.5×10^{11}	2.2×10^{18}	1.3×10^{5}
48	9900AP	4.2×10^{11}	5.2×10^{17}	3.1×10^{4}
	MONSANTO	4.2×10^{11}	7.7×10^{17}	2.2×10^{4}
51	9900AP	5.5×10^{11}	9.3×10^{17}	6.1×10^{3}
	MONSANTO	5.5×10^{11}	1.2×10^{18}	7.2×10^{3}
	MOTOROLA	1.6×10^{11}	2.4×10^{17}	2.3×10^{3}

* UPPER limit (recombination losses in the n-type epitaxial layer neglected)

4.5 Additional Experiments

About 20 additional runs were made using wet oxidation in a temperature range of 1100-1150°C. The oxidation time was 15-45 min. Best results obtained using wet oxides to date were: (a) V_{OC} = 647 mV for a Motorola wafer described in Appendix III with base resistivity of 0.024 Ωcm, and (b) V_{OC} = 643 mV for wafer with 0.1 Ωcm base resistivity and an 8 μm, 0.15 Ωcm epitaxial layer. These results are reproducible and were repeated at least five times. The values of V_{OC} using wet oxides were always above 640 mV in all runs.

Wet oxidation at high temperatures has several advantages compared to dry oxidation for the fabrication of the OCI-HLE cells:

(a) Shorter oxidation times are required to grow about 2000 Å SiO_2. This will reduce the damage to both the substrate and epitaxial layers that results from long (~5 hrs) dry thermal oxidation.

(b) Oxidation temperatures of about 1100°C were sufficient to obtain $V_{OC} \simeq 640$ mV compared to 1150°C required for dry oxide.

(c) Wet oxides have a smaller density of surface states at the $Si-SiO_2$ interface and a higher density of oxide charge, resulting in smaller values for S_{eff}.

One fabrication run using a diffused n^+n HLE junction was done. This run used the 0.1 Ωcm p-type Monsanto substrate (Appendix III). Phosphorous was diffused into the entire area of the epitaxial emitter at 850°C for 15 min, followed by a thermal oxidation at 900°C for 10 min in a dry-wet oxygen ambient. This device had V_{OC} = 625 mV and a dark emitter recombination current $J_{E0} \simeq 3 \times 10^{-13}$ A/cm^2 at 25°C, AM0.

REFERENCES FOR CHAPTER 4

1. H. W. Brandhorst, Jr., Record of 9th IEEE Photovoltaic Specialists Conf., 1 (1972).

2. F. A. Lindholm, A. Neugroschel, C. T. Sah, M. Godlewski, and H. W. Brandhorst, Jr., IEEE Trans. Electron Devices, ED-24, 402 (1977).

3. F. A. Lindholm and C. T. Sah, IEEE Trans. Electron Devices, ED-24, 299 (1977).

4. C. T. Sah and F. A. Lindholm, IEEE Trans. Electron Devices, ED-24, 358 (1977).

5. C. T. Sah, F. A. Lindholm, and J. G. Fossum, IEEE Trans. Electron Devices, ED-25, 66 (1978).

6. J. G. Fossum, F. A. Lindholm, and C. T. Sah, Tech. Digest 1977 Int. Electron Devices Mtg., 222 (1977).

7. F. A. Lindholm, A. Neugroschel, S. C. Pao, J. G. Fossum, and C. T. Sah, Record of 13th IEEE Photovoltaic Specialists Conf., 1300 (1978).

8. A. Neugroschel, F. A. Lindholm, S. C. Pao, and J. G. Fossum, Appl. Phys. Lett., 33(2), 168 (1978).

9. J. R. Hauser and P. M. Dunbar, Solid State Electronics, 18, 715 (1975).

10. M. A. Shibib, F. A. Lindholm, and F. Therez, IEEE Trans. Electron Devices, ED-26, 959 (1979).

11. A. Neugroschel, P. J. Chen, S. C. Pao, and F. A. Lindholm, Record of 13th IEEE Photovoltaic Specialists Conf., 70 (1978).

12. B. E. Deal, M. Sklar, A. S. Grove, and E. H. Snow, J. Electrochem. Soc., 114, 266 (1967).

13. F. Montillo and P. Balk, J. Electrochem. Soc., 118, 1463 (1971).

14. H. P. D. Lanyon and R. A. Tuft, Tech. Digest 1978 Int. Electron Devices Mtg., 316 (1978).

15. M. A. Green, Solid State Electronics, 20, 265 (1977).

16. J. R. Hauser, Final Report on NSF Grant GK-1615, (1969).

17. P. L. Castro and B. E. Deal, J. Electrochem. Soc., 118, 280 (1971).

18. A. Neugroschel, F. A. Lindholm, and C. T. Sah, IEEE Trans. Electron Devices, ED-24, 662 (1977).

19. W. Rosenzeweig, Bell Syst. Technical J., 1573 (1962).

20. S. P. Murarka, J. Electrochem. Soc., 123, 765 (1976).

21. C. L. Claeys, E. E. Laes, G. J. Declerck, and R. J. Van Overstraetan, Semiconductor Silicon 1977, The Electrochem. Soc., Inc., 773.

22. H. Shiraki, Semiconductor Silicon 1977, The Electrochem. Soc, Inc. 546.

23. B. R. Singh and P. Balk, J. Electrochem. Soc., 125, 453 (1978).

24. J. G. Fossum, R. D. Nasby, and E. L. Burgess, Record of 13th IEEE Photovoltaic Specialist Conf., 1294 (1978).

25. P. A. Iles, NASA Contract Report NAS 3-17360.

26. S. M. Sze, Physics of Semiconductor Devices, 430 (1969).

APPENDIX I

PROGRAM TO ANALYZE TRANSISTOR AND DIODE I-V CHARACTERISTIC

```
      DIMENSION V(100),AMP(100),X(100),Y(100)
      REAL MX,IXO,IX,ID, ISAT
      CHARACTER*10 DEVICE,DATE
    1 FORMAT(F10.3)
    2 FORMAT(2F10.2,I10)
    3 FORMAT(8E10.3)
    4 FORMAT(9X,'V',12X,'I(DATA)',9X,' ISAT '/)
    5 FORMAT(F10.3,1PE20.4)
    6 FORMAT(F10.3 1PE20.4,E16.4)
    7 FORMAT('0',' T=',F9.3/)
    8 FORMAT('0',' MX=',F8.3,2X,'IXO=',1PE11.4)
  111 FORMAT('1','DATE:',A10,'     DEVICE NUMBER:     ',A10,
     1//1X,'SOLAR CELL PROJECT, UNIVERSITY OF FLORIDA,',
     1' GAINESVILLE, FLORIDA'//1X,'PROGRAM PA05 I - V DATA',
     1' FITTING'///)
  222 FORMAT(2A10)
C
C THIS PROGRAM COMPUTES MX AND IXO FROM A SET OF PRECHOSEN I-V DATA
C POINTS AT LOWER BIASES WITH INITIAL VALUE AT V1 AND SUBSEQUENT VALUES
C AT DV1 APART.  THE CONTRIBUTION OF THIS COMPONENT AT HIGHER BIASES
C IS SUBTRACTED FROM THE ACTUAL MEASURED DATAS AT HIGHER BIASES
C (STARTING AT V2 WITH AN INCREMENT OF DV2) TO OBTAIN THE DIFFUSION
C COMPONENT ID.  ISAT IS CALCULATED USING ISAT = ID/EXP(V/VT)
C N1 = NUMBER OF DATA POINTS FOR MX, IXO FIT
C N2 = NUMBER OF DATA POINTS FOR ISAT CALCULATION
C MX = SLOPE FACTOR OF LOWER PORTION OF I-V CURVE
C IXO = PRE-EXPONENTIAL FACTOR FOR LOWER PORTION OF I-V CURVE
C IX = SPACE-CHARGE COMPONENT AT BIAS V
C ID = DIFFUSION COMPONENT AT BIAS V
C VT = KT/Q
C ISAT = ESTIMATED DIFFUSION SATURATION CURRENT.  THERE WILL BE A
C        RANGE OF VOLTAGES THAT ISAT IS APPROXIMATELY CONSTANT (VALUES
C        OF ISAT AT LOWER BIASES CALCULATED USING THIS ALGORITHM ARE NOT
C        THE REAL VALUES OF DIFFUSION SATURATION CURRENT DUE TO THE
C        DOMINANCE OF SPACE-CHARGE RECOMBINATION CURRENT AND VALUES OF
C        ISAT AT HIGHER VOLTAGES ARE ALSO NOT THE TRUE VALUES OF DIFFUSION
C        SATYRATUIB CURRENT DUE TO THE EFFECTS OF SERIES RESISTANCE).
C        A SINGLE VALUE OF ISAT CAN BE OBTAINED BY AVERAGING ALL VALUES
C        OF ISAT IN THE VOLTAGE RANGE WHERE THEY ARE APPROXIMATELY
C        CONSTANT.
C
  888 READ(5,222) DEVICE, DATE
      READ(5,1) T
```

```
      IF(T.LE.0) GO TO 999
      READ(5,2) V1,DV1,N1
      READ(5,3) (AMP(I),I=1,N1)
      VT=T*8.616E-5
      DO 10 I=1,N1
      V(I)=V1+(I-1)*DV1
      X(I)=V(I)/VT
   10 Y(I)=ALOG(AMP(I))
      CALL LSQ3(X,Y,N1,MX,IXO)
      IXO=EXP(IXO)
      WRITE(6,111) DATE,DEVICE
      WRITE(6,4)
      DO 20 I=1,N1
   20 WRITE(6,5) V(I),AMP(I)
      READ(5,2) V2,DV2,N2
      READ(5,3) (AMP(I),I=1,N2)
      DO 30 I=1, N2
      V(I)=V2+(I-1)*DV2
      IX=IXO*EXP(V(I)/(MX*VT))
      ID=AMP(I)-IX
      ISAT=ID/EXP(V(I)/VT)
   30 WRITE(6,6)  V(I),AMP(I),ISAT
      WRITE(6,7) T
      WRITE(6,8) MX,IXO
      GO TO 888
  999 STOP
      END

      SUBROUTINE LSQ3(X,Y,N,A,B)
      DIMENSION X(N),Y(N),XN(30)
      XBAR=0
      DO 10 I=1,N
   10 XBAR=XBAR+X(I)
      XBAR=XBAR/N
      F=0
      FX1=0
      X2=0
      DO 20 I=1,N
      XN(I)=X(I)-XBAR
      FX1=FX1+Y(I)*XN(I)
      F=F+Y(I)
   20 X2=X2+XN(I)*XN(I)
      A=FX1/X2
      B=F/N
      B=B-A*XBAR
      A=1./A
      RETURN
      END
```

APPENDIX II

STANDARD WAFER CLEANING PROCESS

1. Scrub with cotton swab soaked with TCE.
2. Boil in TCE, 5 min.
3. Boil in ACE, 5 min.
4. Boil in methyl alcohol, 5 min.
5. Rinse in deionized water, 5 min.
6. Dip in $1HCL:1H_2O_2:6H_2O$ solution at 80°C, 15 min.
7. Rinse in deionized water, 5 min.
8. Deglaze in $1HF:10H_2O$ solution, 10 sec.
9. Rinse in deionized water, 5 min.
10. Spin dry with N_2 gas flow.

APPENDIX III

FABRICATION SCHEDULE FOR OXIDE-CHARGE-INDUCED HIGH-LOW EMITTER JUNCTION SOLAR CELL

We have fabricated OCI-HLE solar cells on several types of wafers. We will identify them as follows:

1. 9900AP - 1.5 Ω-cm, 10 μm thick n-type arsenic-doped epitaxial layer on 300 μm thick <111> 0.15 Ω-cm boron-doped Czochralski-growth substrate.
2. 9900AQ - 1.5 Ω-cm, 4 μm thick n-type arsenic-doped epitaxial layer on 300 μm thick <111> 0.15 Ω-cm boron-doped Czochralski-grown substrate.
3. MONSANTO - 0.1 Ω-cm, 10 μm arsenic-doped epitaxial layer on 300 μm thick <111> 0.1 Ω-cm boron-doped Czochralski-grown substrate.
4. MOTOROLA - 0.15 Ω-cm, 5 μm n-type epitaxial layer on 500 μm thick <100> 0.025 Ω-cm boron-doped Czochralski-grown substrate.

In the following process runs all push-in and pull-out of wafers for the oxidation, phosphorous diffusion, and oxygen annealing processes are done in a nitrogen ambient in about 5 min unless otherwise specified.

Run #25

Wafer: 9900AP with 5000 Å of chemical-vapor-deposited (CVD) oxide on front surface.

Steps:

1. Phosphorous gettering: 1100°C, 3 hr.
2. Etch oxides from both sides.
3. Standard wafer clearning (Appendix II).
4. Oxidation: 1100°C, 3 hr with 1 ℓ/min dry O_2 and 5 cc/min N_2 bubbling through TCE. Oxide thickness ≈ 2500 Å.
5. Define front contact openings using mask #1.
6. Standard wafer cleaning.
7. Phosphorous diffusion through contact openings: 900°C, 15 min with 20 cc/min N_2 bubbling through $POCl_3$ at 30°C, 100 cc/min O_2, and 1.5 ℓ/min N_2 as carrier gas. R_s ≈ 30 Ω/square.
8. Etch phosphosilicate glass in BOE etch for 10 sec.
9. Oxygen anneal: 700°C, 2 hr with 1.5 ℓ/min dry O_2.
10. Oxide etch until field oxide reaches 1100 Å.
11. Aluminum deposition on front surface.
12. Define metal grid pattern using mask #2.
13. Remove the n^+ diffusion from the backside by lapping with silicon carbide abrasive powder.
14. Aluminum deposition on back surface.
15. Forming gas anneal (10% H_2, 90% N_2) : 450°C, 15 min.
16. Scribing and edge etching.

Run #26

Wafer: MONSANTO

Steps:

1. Standard wafer cleaning.
2. Oxidation: 1100°C, 7 hr with 1 ℓ/min dry O_2 and 5 cc/min N_2 bubbling through TCE. Oxide thickness ≈ 3750 Å.
3. Define front contact openings using mask #1.
4. Standard wafer cleaning.
5. Phosphorous diffusior through contact openings: 900°C, 20 min with 20 cc/min N_2 bubbling through $POCl_3$ at 30°C, 100 cc/min O_2, and 1.5 ℓ/min N_2 as carrier gas. R_s ≈ 25 Ω/square.
6. Oxygen annealing: 700°C, 10 hr with 1.5 ℓ/min dry O_2.
7. Etch oxide until field oxide is about 1100 Å.
8. Aluminum deposition on front surface.
9. Define metal grid pattern using mask #2.
10. Lapping the back surface.
11. Aluminum deposition on back surface.
12. Forming gas anneal: 450°C, 15 min.
13. Scribing and edge etching.

Run #27: Effect of phosphorous gettering on bulk lifetime

Wafer: MONSANTO

Steps:

1. Standard wafer cleaning.
2. Oxidation: 1100°C, 7 hr with 1 ℓ/min dry O_2 and 5 cc/min N_2 bubbling through TCE.
3. Remove oxide at the back surface.
4. Phosphorous gettering: 1000°C, 45 min with 20 cc/min N_2 bubbling through $POCl_3$ at 30°C, 100 cc/min O_2, and 1.5 ℓ/min N_2 as carrier gas.
5. See steps 3 - 13 of Run #26.

Run #28: Determination of bulk lifetime in starting wafers

Wafer: 9900AQ, MONSANTO

Steps:

1. Standard wafer cleaning.
2. Phosphorous diffusion: 850°C, 15 min.
3. Etch oxides from both sides.
4. Remove n^+ diffusion from back side.
5. Evaporate aluminum on both front and back surfaces.
6. Scribing and edge etching.

Run #31: Oxidation (wet) at lower temperature (900 C)

Wafer: 9900AP, 9900AQ, both with CVD oxide on front surface.

Steps:

1. Define contact windows through CVD oxide for n^+ contact diffusion.
2. Standard wafer cleaning.
3. Phosphorous diffusion: 850°C, 15 min with the same flow rates and source temperature as previous runs. Cool wafers down to 700°C in N_2 (90 min).
4. Strip oxides on both surfaces.
5. Oxidation: 900°C, 5 min dry oxidation, 10 min wet oxidation, 5 min dry oxidation. Wafers cooled to 700°C in dry O_2 (900°C).
6. Reopen contact windows using mask #1.
7. Standard metallization and annealing process (steps 11-16 of Run #25).

Run #32: Oxidation (dry) at lower temperature (800°C)

Wafer: 9900AQ with CVD oxide on front surface.

Steps:

1. See steps 1 - 4 of Run #31.
2. Oxidation: 800°C, 16 hr and cool wafers down to 700°C in N_2 in 1 hr then in O_2 for 2 hr at 700°C in same furnace.
3. Reopen contact windows using mask #1.
4. Standard metallization and annealing process (steps 11 - 16 of Run #25).

Run #35: Slow cooling of wafers in N_2 after high temperature processes

Wafer: 9900AP, MONSANTO

Steps:

1. Standard wafer cleaning.
2. Oxidation: 1100°C, 3 hr with 1 ℓ/min dry O_2 and 5 cc/min N_2 bubbling through TCE. Cool wafers down to 1000°C at 0.5°C/min and to 900°C at 1.5°C/min and then to 700°C in 90 min. The cooling was done in a nitrogen ambient.
3. Define contact openings using mask #1.
4. Standard wafer cleaning.
5. Phosphorous diffusion: 850°C, 20 min. Cool wafers down to 700°C in N_2 in 90 min.
6. Etch oxide until field oxide is about 1100 Å.
7. Oxygen annealing: 700°C, 2 hr.
8. Etch thin oxide over contact windows.
9. Standard metallization and annealing process (as steps 11 - 16 of Run #25).

Run #36: Slow cooling of wafers in O_2 after high temperature processes.

Wafer: 9900AP

Steps:

1. Standard wafer cleaning.
2. Oxidation: 1100°C, 3 hrs with 1 ℓ/min dry O_2 and 5 cc/min N_2 bubbling through TCE. Cool wafers down to 1000°C at 0.5°C/min and to 900°C at 1.5°C/min and then to 700°C in 90 min. The cooling was done in an oxygen ambient.
3. Define contact openings using mask #1.
4. Standard wafer cleaning.
5. Phosphorous diffusion: 850°C, 20 min. Cool wafers down to 700°C in O_2 in 90 min.
6. Etch oxide until field oxide is about 1100 Å.
7. Standard metallization and annealing process (as steps 11 - 16 of Run #25).

Run #48: Oxidation with TCE at 1150°C

Wafer: 9900AP, MONSANTO

Steps:

1. Standard wafer cleaning.
2. Oxidation: 1150°C, 5 hr with 1.5 ℓ/min dry O_2 and 3cc/min N_2 bubbling through TCE.
3. Define front contact openings using mask #1.
4. Standard wafer cleaning.
5. Phosphorous diffusion: 850°C, 20 min.
6. Oxygen annealing: 700°C, 2 hr.
7. Oxide etch until field oxide reaches 1100 Å.
8. Usual metallization and annealing process (steps 11 - 16 of Run #25).

Run #51

Wafer: 9900AP, MONSANTO, MOTOROLA

Steps:

As Run #48 except the wafers are annealed in dry oxygen at 700°C for 12½ hours in Step 8.

APPENDIX IV

LAYOUT OF MASKS USED IN SOLAR CELLS FABRICATION

We use photolithographic techniques to define the contact openings to the front emitter surface and also the metal grid pattern on the front surface. The layout of masks used are shown below. The shaded areas correspond to the darkened area in the emulsion plate. Waycoat negative photoresist is used throughout.

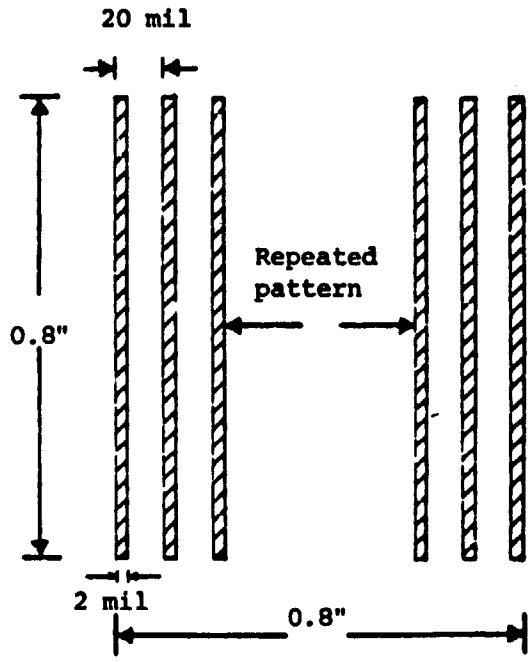

Mask #1: Mask used for contact openings to the front emitter surface. It consists of thirty nine 2 mil x 800 mil strips, with 20 mil center to center spacing.

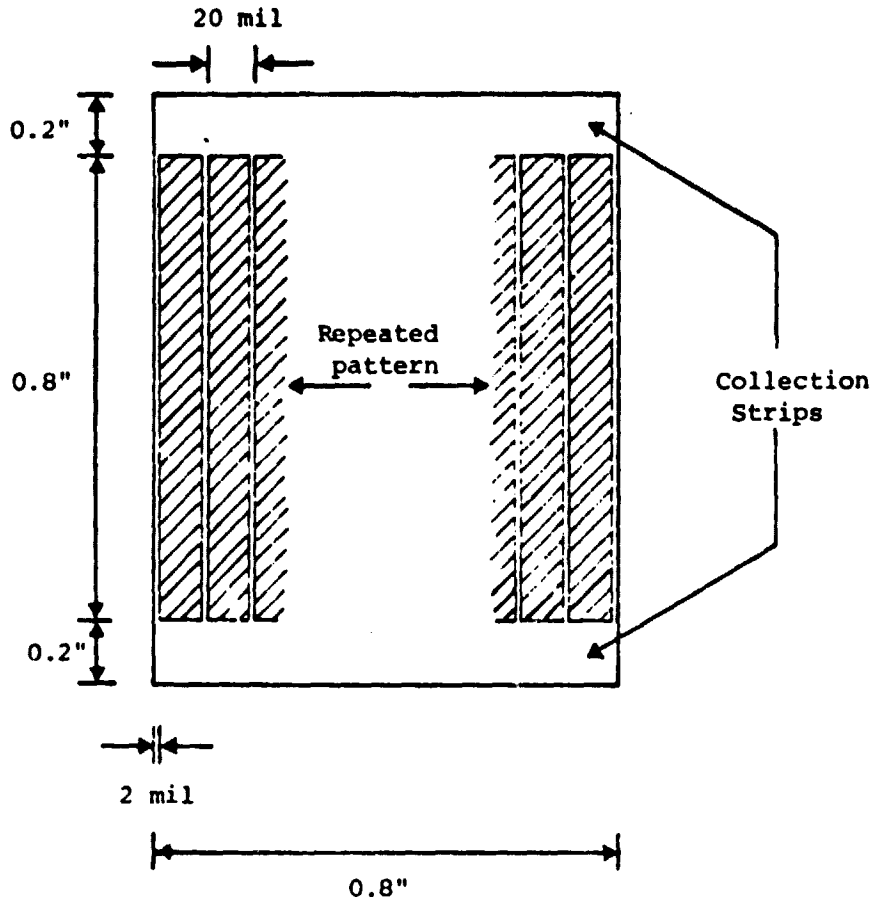

Mask #2: Mask used for defining metal grid pattern on the front surface. The thin contact fingers occupy 10% of the area excluding the collection strips.

CHAPTER 5

DETERMINATION OF LIFETIMES AND RECOMBINATION CURRENTS IN p-n JUNCTION SOLAR CELLS AND DIODES

I. INTRODUCTION

The minority carrier base diffusion length is an important material parameter determining the performance of solar cells. Very long diffusion lengths, longer than the base width, are desirable for the successful operation of BSF, IBC, FSF, and TJ cells [1] - [4]. Such long diffusion lengths are necessary to achieve large values of the short circuit current J_{SC}, to minimize the base dark current, and thus lead to large cell efficiency η. A long diffusion length is also necessary in the emitter of the HLE cell [5] for similar reasons.

Numerous methods exist to measure the base diffusion length L_B [6,7]. These methods are based on the measurement of some device parameter, such as current, capacitance, etc., which is dependent on L_B. To measure L_B accurately, L_B has to be smaller than the base width W_B, i.e., $L_B < W_B$. In this case, the minority carriers recombine within the base without interacting with a back contact. If, however, $L_B \sim W_B$ the minority carriers interact with the back contact and the measured parameter is dependent on a slowly varying (hyperbolic) function of W_B/L_B [7]. If $L_B > W_B$, the measured parameters depends on W_B only, and is independent of L_B. Thus, existing methods of measurement do not work well for cells with $L_B > W_B$.

An accurate knowledge of L_B is still very important even if $L_B > W_B$, since the dark base recombination current Q_B/τ_B can still significantly contribute to the total dark current of the device.

In this paper, methods for the accurate measurement of L in a narrow region W in cells for which L > W are described. The methods are applicable to essentially all cells and diodes with a narrow region either in the base or in the emitter.

The first method, described in Section II, is based on basewidth-modulation of n-p-n or p-n-p transistor-like structures. The method involves measurement of the low-frequency small signal conductances which arise from the basewidth-

modulation by a small ac signal. TJ cells are directly applicable for the method, since they are, in essence, transistor structures. For other cells, transistor-like structures can be obtained by modification of the cell structures done at low temperature. The method requires only a knowledge of the base width W_B and the base doping, and the accuracy is better than about $\pm$ 10%. The method applies for both high and low levels of carrier injection.

Section III discusses the small-signal admittance method. This method can be applied to practically any cell with a narrow region either in the base, or in the emitter which is the case for the HLE cell [5]. It also leads to determination of the recombination velocity at the back of the narrow region. Section IV describes a simple method to determine the diffusion length, which is based on measurements of dc currents on two related structures.

Based on an accurate knowledge of L, a simple analysis of the cells can be made. This analysis, described in Section V, uses measurement of dark currents and small-signal admittance, and leads to determination of the recombination currents in each region of the cell. Section VI shows illustrative examples of the analysis of three cells: n^+-p-n^+ TJ cell, n^+-p-p^+ BSF cell, and p^+-n-n^+ BSF cell. Section VII discusses the accuracy of the measurements.

II. BASEWIDTH-MODULATION METHOD

A. Minority carrier lifetime

The basewidth-modulation (BWM) method for determination of the minority carrier base lifetime of junction transistors was recently published (8). This method is applied here for the case of very wide base regions in solar cells. The method is also extended to determine the recombination currents in the quasi-neutral emitter and collector regions of the cells.

The basewidth-modulation effects arise from voltages appearing across the base-collector junction of the transistor. Any change in the base-collector voltage will produce a change in the width of the junction space-

charge-region (SCR) which, in turn, produces a change in the width, W_B, of the quasi-neutral base (QNB) region, as illustrated in Fig.1 for an n^+-p-n^+ transistor. The change in the base width, ΔW_B, produces three effects: a) the amount of excess minority carrier (electron) charge Q_B stored in the QNB changes by ΔQ_B; b) the component of the base current due to recombination within the QNB changes by $\Delta Q_B/\tau_B$; and c) the collector current changes because of the change in the slope of the excess minority electron distribution N(x) in the base.

The BWM effects can be detected by measuring a low-frequency small-signal output conductance G_o and a reverse transconductance G_r [2] of the device:

$$G_o = \frac{i_c}{v_{ce}}\bigg|_{v_{be}=0} = \frac{\partial I_c}{\partial W_B}\cdot\frac{W_B}{V_{CB}}\bigg|_{V_{BE}} \tag{1}$$

$$G_r = \frac{i_b}{v_{ce}}\bigg|_{v_{be}=0} = \frac{\partial I_B}{\partial W_B}\cdot\frac{\partial W_B}{\partial V_{CB}}\bigg|_{V_{BE}} . \tag{2}$$

G_o and G_r result from modulation of the base width by a small ac signal applied between the collector and emitter terminals with base-emitter voltage V_{BE} kept constant. For an n-p-n transistor (for example) with a uniform base doping N_{AA}, under condition of low-injection and negligible recombination in the QNB ($L_n >> W_B$), the charge-control minority carrier (electron) lifetime τ_n is [8]

$$\tau_n = -\tau_F \frac{G_o}{G_r} \tag{3}$$

where

$$\tau_F = \frac{W_B^2}{2D_n} \tag{4}$$

is the minority-carrier transit time across the QNB and D_n is the electron diffusion coefficient. The minus sign in (3) results from the fact that G_r is negative. G_o and G_r are both proportional to $\exp(qV_{BE}/kT)$ [8]. The minority carrier lifetime in the base can thus be determined by measuring G_o and G_r and calculating τ_F from the base width and base doping.

This method can be extended for use under the condition of high-injection occuring in the p-type base. In high injection [9]

$$N(0) = n_i \exp \frac{qV_{BE}}{2kT} \quad . \tag{5}$$

Using (5), we obtain for the collector and base currents:

$$I_C = \frac{A_{BE} 2qD_n n_i}{W_B} \exp \frac{qV_{BE}}{2kT} \tag{6}$$

$$I_B = \frac{A_{BE} q n_i W_B}{2\tau_H} \exp \frac{qV_{BE}}{2kT} \tag{7}$$

where $\tau_H = \tau_n + \tau_p$ is the high-injection lifetime [9].

Using (1) and (2) we obtain:

$$\tau_H = -\frac{1}{2} F \frac{G_o}{G_r} \quad . \tag{8}$$

This expression is similar to (3) for the low-injection case except for a factor of 1/2. Note also that G_o and G_r are both proportional to $\exp(qV_{BE}/2kT)$ in high-injection [9]. Equation (6) is valid if $W < L$ and if the recombination current in the emitter is negligible [9]. This will apply to many devices with a wide low-doped base region. If the above conditions do not apply, then a more general solution is required to obtain τ_H [9].

Our treatment was restricted so far to the case for which $L_n > W_B$, resulting in a linear dependence of N(x) on distance within the base. The method, however, is applicable also for $L \sim W_B$. It can be easily shown that for this general case:

$$\frac{G_o}{G_r} = -\frac{\cosh \frac{W_B}{L_n}}{\sinh \frac{W_B}{2L_n}} \quad . \tag{9}$$

This expression converges to (3) for $W_B/L_n < 1$. For $W_B/L_n = 1$, the difference between L_n determined from (3) and (9) is only about 8%, i.e., for $W_B \approx L_n$, (3) can be used with only a small error.

Conductances G_o and G_r are due only to changes in the QNB region provided V_{CB} is low enough to make the generation currents in the collector depletion layer negligible. They are independent of the recombination currents in the emitter and in the base-emitter space-charge region, since V_{BE} is held constant. Therefore, G_o and G_r will follow the ideal $\exp(qV_{BE}/kT)$ dependence in low-injection and $\exp(qV_{BE}/2kT)$ dependence in high-injection. This ideal exponential dependence of both G_o and G_r on voltage serves as a very convenient self-consistency measurement check of the method. This check also assures us that series resistance is low enough, mainly in high-injection, to validate the assumptions underlying the method.

B. Determination of the emitter current

Once the base lifetime, τ_n, is measured using the BWM technique, the emitter contribution to the base current can be easily found. The total measured base current I_{BT} for forward-active operation in low-injection is [10,11]

$$I_{BT} = \frac{Q_B}{\tau_n} + \frac{Q_E}{\tau_E} + \frac{Q_{SCR}}{\tau_{SCR}} \qquad (10)$$

where Q_B, Q_E and Q_{SCR} are the excess minority carrier charges in the base, emitter, and SCR, respectively; and τ_n, τ_E and τ_{SCR} are the respective charge-control time constants. The SCR recombination current Q_{SCR}/τ_{SCR} can be removed from the measured I_B-V_{BE} characteristic by an appropriate subtraction [10,11]. The remaining base saturation current, I_{BO} is then

$$I_{BO} = \frac{Q_{BO}}{\tau_n} + \frac{Q_{EO}}{\tau_E} \qquad (11)$$

where Q_{BO} and Q_{EO} are the minority charges at equilibrium: $Q_B = Q_{BO} \exp(qV_{BE}/kT)$, $Q_E = Q_{EO} \exp(qV_{BE}/kT)$.

The ideal common emitter current gain is given by [11]

$$h_{FE}(\text{ideal}) = \frac{I_{CO}}{I_{BO}} = \frac{Q_{BO}/\tau_F}{Q_{BO}/\tau_n + Q_{EO}/\tau_E} \quad . \qquad (12)$$

Solving for Q_{EO}/τ_E and combining with (3), the recombination current occuring within the quasi-neutral emitter is

$$\frac{Q_{EO}}{\tau_E} = \frac{Q_{BO}}{\tau_n}\left(\frac{G_o/G_r}{h_{FE}(\text{ideal})} - 1\right) \quad . \tag{13}$$

Q_{EO}/τ_E is thus found by combining the small-signal ac measurements (G_o/G_r) with dc characteristics of the transistor (h_{FE}).

For a transistor with negligible recombination losses in the emitter, $Q_{EO}/\tau_E \ll Q_{BO}/\tau_B$, note that

$$h_{FE}(\text{ideal}) = \frac{Q_{BO}/\tau_F}{Q_{BO}/\tau_n} = \frac{\tau_n}{\tau_F} \tag{14}$$

in accord with conventional transistor theory. The minority carrier base lifetime is then simply $\tau_n = \tau_F\, h_{FE}(\text{ideal})$. This provides a method for finding τ_n that is an alternative to that based on (3). But finding $h_{FE}(\text{ideal})$ requires subtraction of the SCR current component from I_{BT}. This subtraction is subject to errors depending on magnitude and voltage dependence of components in (10). Thus, the method based on (3) is the more accurate method.

The current due to recombination in the n^+-collector quasi-neutral region can be measured by reversing the roles of collector and emitter and using (13) again.

III. SMALL-SIGNAL ADMITTANCE METHOD

A. Minority carrier lifetime

The BWM technique described in the previous section is directly applicable for TJ cells, since the TJ cell is actually a transistor-like structure. It cannot, however, be applied directly to some other cells with a narrow base or emitter region which are diode structures only, without a collector. In these cases, a different measurement method has to be used. In this section we present a method applicable to all cells with a narrow base or emitter region.

Fig. 2 shows two different cells with either narrow base, BSF cell--Fig. 2(a), or narrow emitter, HLE cell--Fig. 2(b). In both cases a high-low junction exists in the narrow region of the cell, and is characterized by an effective surface recombination velocity S_{eff} for the minority carriers. Fig. 2(c) shows the basic structure of the IBC, FSF, and TJ cells [2,3,4]. In this structure both the n^+-region and the p^+ contacts to the base are on the bottom nonilluminated surface. The p^+ regions cover only a small portion ($\sim$10%) of the total area. The top illuminated surface is left floating and is characterized by the surface recombination velocity S for the IBC cell. If a p^+-p junction (FSF cell) or a n^+-p junction (TJ cell) is used on the top surface, then the surface region can be characterized by an effective surface recombination velocity S_{eff}. Due to structural similarities which are evident in Fig. 2, the cells shown in Fig. 2 will all have a similar treatment for the narrow region small-signal admittance. The treatment shown below is done for a n^+-p-p^+ BSF cell as an illustration.

Consider, for example, a n^+-p-p^+ BSF cell, Fig. 3, with a base width W_p and minority carrier base lifetime τ_n corresponding to the diffusion length $L_n = \sqrt{D_n \tau_n}$. The electron current at the high-low junction ($x = W_p$) is [12]

$$J_n(W_p) = qS_{eff}N(W_p) \tag{15}$$

where S_{eff} is the effective surface recombination velocity for electrons at $x = W_p$. By solving a continuity equation [13] in low-injection for an ac signal superimposed on a steady forward bias, and using boundary condition (15), we can derive the expressions for the small-signal quasi-neutral base capacitance C_{QNB} and conductance G_{QNB} valid for a low frequency signal with $\omega\tau_n \ll 1$:

$$C_{QNB} = \frac{q}{kT}\frac{AqD_n n_i^2}{2N_{AA}L_n}\left[\frac{\frac{W_p D_n}{L_n} - \frac{L_n W_p S_{eff}^2}{D_n} - S_{eff}L_n}{2\sinh^2\frac{W_p}{L_n}\left(\frac{D_n}{L_n}\coth\frac{W_p}{L_n} + S_{eff}\right)^2} + \tau_n\frac{\frac{D_n}{L_n} + S_{eff}\coth\frac{W_p}{L_n}}{\frac{D_n}{L_n}\coth\frac{W_p}{L_n} + S_{eff}}\right]\left[\exp\left(\frac{qV}{kT}\right) - 1\right] \tag{16}$$

$$G_{QNB} = \frac{q}{kT} \frac{AqD_n n_i^2}{L_n N_{AA}} \left[\frac{\frac{D_n}{L_n} + S_{eff} \coth \frac{W_p}{L_n}}{\frac{D_n}{L_n} \coth \frac{W_p}{L_n} + S_{eff}} \right] \left[\exp\left(\frac{qV}{kT}\right) - 1 \right] \quad . \tag{17}$$

The expression for C_{QNB} can be simplified for the following conditions:

$$W_p/L_n \gtrsim 1 \tag{18}$$

$$S_{eff} \sim 100 \text{ cm/sec} \quad . \tag{19}$$

These conditions are not restrictive for an actual device, with good performance and a narrow base. Under these conditions the first term inside of the parentheses in (16) can be neglected and combining (16) and (17) yields

$$\tau_n \simeq 2 \frac{C_{QNB}}{G_{QNB}} \quad . \tag{20}$$

This expression for τ_n is similar to that valid for $W_p >> L_n$ [14].

To determine C_{QNB}, we measure the capacitance at two frequencies: C_{LF} at $\omega\tau_n << 1$ and C_{HF} at $\omega\tau_n >> 1$ to obtain [14]:

$$C_{QN} \simeq C_{QNB} = C_{LF} - C_{HF} \quad . \tag{21}$$

This results because the n^+ base and p^+ emitter regions are much narrower than W_p and the amount of minority-carrier charge in these regions will be negligible compared to that in the wide base, giving $C_{QN} \simeq C_{QNB}$.

To determine G_{QNB}, we measure a total conductance G at the terminals which consists of a few components [10]:

$$G = G_{QNE} + G_{QNB} + G_{SCR} \tag{22}$$

where G_{SCR} is the conductance from the bulk and surface base-emitter space-

charge region, and G_{QNE} designates the contribution of the emitter quasi-neutral region. G_{SCR} can be eliminated from the data by a subtraction technique to give

$$G_{QN} = G_{QNE} + G_{QNB} \quad . \tag{23}$$

If $G_{QNE} < G_{QNB}$, then $G_{QN} \simeq G_{QNB}$ and τ_n can be then determined from (20). This condition will apply for many devices made on high resistivity substrates ($\sim$1-10 Ωcm) with wide base. If G_{QNE} is not negligible, an independent method is required to determine it before we can calculate τ_n from (20). One simple method involves thinning the base region to assure $W_p < L_n$ and providing an ohmic contact to the base instead of a high-low junction. The narrow-base current can then be calculated using a conventional formula and subtracted from the total measured diode current to give the emitter current or G_{QNE}.

For the case of the HLE cell of Fig. 4, we note that the n-type emitter is the narrow region of interest, with a minority carrier (hole) lifetime τ_p. To determine τ_p, we proceed as follows: we measure the electron diffusion length in a wide base by an X-ray technique, [15] or some other suitable method, and calculate C_{QNB} and G_{QNB}. These two values are then subtracted from measured C_{QN}, G_{QN} to give C_{QNE}, G_{QNE}, and

$$\tau_p = 2 \frac{C_{QNE}}{G_{QNE}} \quad . \tag{24}$$

The small-signal admittance method can be also applied for conditions of high-injection in the narrow region. Following the derivation of (16) and (17) for $P \simeq N$ we obtain for high-injection lifetime:

$$\tau_H \simeq 4 \frac{C_{QNB}}{G_{QNB}} \quad . \tag{25}$$

Equation (25) is similar to (20) except for a factor of two which results because the electron diffusion constant D_n is doubled in high-injection [9]. This

equation is valid for the common case of a negligible emitter current and $W_p/L_n < 1$ [9].

A more complicated, but accurate way to determine both G_{QNE} and τ_n in the BSF cell and other structures of Fig. 2 is to use the BWM technique described in the previous section. In order to do that, we have to first create a modified transistor-like structure from the actual cells. This can be done quite easily as shown in Fig. 5. For the case of p^+-n-n^+ BSF cell, the n^+ region on the back can be etched-off from about 90% of the area and Al can be evaporated on n-type base to create a Schottky barrier collector; the remains of n^+ BSF region serve as a contact to the base, see Fig. 5(a). This procedure can be also used for n^+-n-p HLE cell from Fig. 2(b). In the case of a n^+-p-p^+ BSF cell, Fig. 5(b), an n^+-diffusion is performed simultaneously from both sides of the p-type substrate. Emitter can then be a mesa-type and the p^+ region for the base contact over about 10% of the area can be done by a standard method used to create a BSF region. Schottky barrier collector using Al cannot be used on p-type substrates because a metal-semiconductor junction on p-type substrates is usually very poor. Similar transistor-like structures can be made also from the FSF and IBC cells.

B. Determination of S (S_{eff})

Once the minority carrier lifetime in the narrow region is found, then $S(S_{eff})$ can be determined either from small-signal quasi-neutral conductance or capacitance of this region. The capacitance is, however, a much better choice because of reasons discussed earlier (see also Section VI C). This procedure is strictly valid only if $S(S_{eff})$ is constant, independent of applied voltage. This condition will be satisfied at low-injection for BSF, FSF, and HLE cells [12], but may not be satisfied for TJ and IBC cells. If $S(S_{eff})$ is not constant, then using (16) or (17) will result in an average value.

IV. MINORITY CARRIER BASE LIFETIME FROM DC CURRENT MEASUREMENTS

An alternative method, suitable for TJ cells or the transistor-like structures, Fig. 5, is proposed. This method requires only dc current measurements on two related structures. The first structure is the actual TJ cell (for example), Fig. 6(a). The other structure, Fig. 6(b), is created by removing the n^+ layer on one side of the cell and replacing it by an ohmic contact.

We will neglect the contribution of the SCR, which can be removed by an experimental procedure [10]. The base saturation current of the transistor-like structure is given by (11), the collector saturation current is $I_{CO} = Q_{BO}/\tau_F$. The saturation current I_0 of the narrow-base diode from Fig. 6(b) is

$$I_0 = \frac{Q_{BO}}{\tau_F} + \frac{Q_{EO}}{\tau_E} \quad . \tag{26}$$

Combining (11) and (26), we obtain for τ_n:

$$\tau_n = \frac{I_{CO}}{I_{BO} + I_{CO} - I_0} \tau_F \quad . \tag{27}$$

In (27) all currents are measured and $\tau_F = W_B^2/2D_n$ is calculated.

The disadvantage of this procedure is that the separation of SCR current components [10] is subject to errors. This will limit the applicability of this method, mainly if $I_{BO} + I_{CO} \sim I_0$, which is the case when the emitter dominates the current. The recombination current in the emitter is simply found from (26)

$$\frac{Q_{EO}}{\tau_E} = I_0 - I_{CO} \quad . \tag{28}$$

An expression similar to (28) can be derived for τ_H, differing only by a factor of 1/2 on the right side of (28). Note that in this case the currents in (27) are proportional to exp(qV/2kT). Also note that a highly-doped emitter will remain in low-injection.

V. ANALYSIS OF DARK CURRENTS IN THE CELL

The analysis of dark currents in the cell is demonstrated for a n^+-p-p^+

BSF and for n^+-n-p HLE cell shown in Figs. 3 and 4, which also show distribution of minority carriers in these cells. The analysis is based on independent measurement of τ_n by one of the three methods described before. The effective surface recombination velocity is determined from a small-signal capacitance using (16). This allows us to calculate N(x) [9] and the recombination currents in the p and p^+ portions of the base. The SCR current, I_{SCR} is determined graphically [10], the recombination current in the emitter region can be obtained by the BWM technique or using the dc method. The sum of all currents recombining within the cell has to be equal to the total measured dark current I. This serves as a self-consistency check of the analysis. Another check for dark current I results from measurement of the short circuit current I_{SC} and open-circuit voltage V_{OC} through

$$V_{OC} = \frac{kT}{q} \ln \frac{I_{SC}}{I_0} \tag{29}$$

where I_0 is the dark saturation current corresponding to I.

The analysis of the n^+-n-p HLE solar cell, Fig. 4, starts with the wide p-type base. The electron diffusion length is measured by the X-ray method [15], and the base dark current and small-signal quasi neutral capacitance [14] are calculated. The hole lifetime τ_p and S_{eff} at the n^+-n junction are then evaluated as was described in Section 3A, 3B. The rest of the analysis follows the BSF case above.

For high-injection conditions in the low-doped part of the base in the BSF cell or low-doped part of the emitter in the HLE cell, we again measure τ_{II} in these regions as described in Sections IIA, IIIA, and IV. The value of S_{eff} increases with applied voltage in high-injection [12]. The analysis has to be then made for a certain voltage, for example $V = V_{OC}$ corresponding to a certain illumination level; S_{eff} can then be calculated based on its low-injection value provided that the voltage drop in the quasi neutral low-doped portion of the base is negligible [12]. The high-doped regions of the cell will remain in low-injection. The analysis then follows the low-injection case.

VI. ILLUSTRATIVE EXAMPLES

To demonstrate the various methods for analysis of the cells, we have done measurements on three different types of cells. The complete analysis for these devices is summarized in this section.

A. n^+-p-n^+ TJ cell

This cell is fabricated on 6 Ωcm($N_{AA} \simeq 2 \times 10^{15}$ cm^{-3}) p-type substrate. The top illuminated n^+-layer is about 0.3 μm deep, the surface is texturized and covered by an AR coating. The bottom n^+-layer is about 0.7 μm deep. The base width is 160 μm. Measured performance at one-sun AM0 illumination at 25°C with top junction floating was: $V_{OC} = 577$ mV, $J_{SC} = 30.5$ mA/cm^2.

An ohmic contact to the top junction was provided after removing the AR coating. The measured dc and ac characteristics for this transistor-like structure are shown in Fig. 7. The data were taken with the bottom n^+-region serving as an emitter. The BWM conductances were measured at 2kHz using a Wayne-Kerr B224 admittance bridge. The dependencies of I_c, G_o and G_r are proportional to exp $q(V_{BE}/kT)$, which confirms that the BWM effects alone are responsible for G_o and G_r. For $V_{BE} < 0.4$ V the leakage of the base-collector junction may dominate G_o and G_r, in some devices, giving almost constant values independent on V_{BE}. These values can be then subtracted from the measured G_o and G_r to extend the range of the exponential dependence on V_{BE}.

From Fig. 7 we have for the low-injection case: $G_o/G_r \simeq \tau_n/\tau_F \simeq 13$; $h_{FE}(\text{ideal}) \simeq 13$. Using (4) and (13) we then obtain: $\tau_n \simeq 50$ μsec ($L_n \simeq 410$ μm) and $Q_{EO}/\tau_E \simeq 0$, i.e. $Q_{EO}/\tau_E << Q_{BO}/\tau_n$. Examination of the I_B-V_{BE} dependence in Fig. 7 shows that the base will be in high-injection for $V_{BE} > 0.6$ V. The base current follows an exp $q(V_{BE}/2kT)$ dependence in accord with (7), provided that the effects of series resistance R_s are negligible. Because $Q_E/\tau_E << Q_B/\tau_B$, τ_H can be found from (7): $\tau_H \simeq 200$ μsec. Further analysis of the cell, described in Section V, with the top junction left floating leads to determination

of recombination losses in the top n^+-layer and in the p-base region. A summary of all results obtained for this cell are shown below. The dark currents are given as a fraction of the total dark current density $J = 3 \times 10^{12}$ A/cm^2 measured at $V = V_{OC} = 577$ mV. The results are:

$\tau_n \approx 50$ μsec

$L_n \approx 410$ μm

$\tau_H \approx 200$ μsec

$S_{eff} \approx 350$ cm/sec

$J_E \approx 0.52$ J

$J_B \approx 0.42$ J

$J_{SCR} \approx 0.06$ J

$J_C \ll J_B$.

The measurements of G_o and G_r in high-injection were not possible, because the collector current in this region exceeded the maximum allowable current of the bridge for the large area (4 cm^2) device used.

B. n^+-p-p^+ BSF cell

This cell was fabricated on 1.5 Ωcm($N_{AA} \approx 1 \times 10^{16}$ cm^{-3}) substrate. The n^+-region is about 0.3 μm deep, sheet resistance is about 55 Ω/square. The BSF high-low junction was created by an Al-paste alloying [16]. The cell was 220 μm thick and has a Ta_2O_5 AR coating on the top. The parameters measured at one-sun (AM0, 25°C) illumination are: $V_{OC} = 617$ mV, $J_{SC} = 38$ mA/cm^2.

The values for τ_n and Q_E/τ_E were measured by the BWM method on a modified structure shown in Fig. 5(b). The recombination currents in the p and p^+-region were then measured on the actual BSF cell, S_{eff} was determined from the dark base current using (17). The inspection of the dark I-V characteristic showed that this cell is in low-injection at one-sun illumination level.

The results are: $\tau_n \approx 120$ μsec

$L_n \approx 600$ μm

$S_{eff} \simeq 380$ cm/sec

$J_E \simeq 0.4$ J

$J_B \simeq 0.15$ J

$J_{B^+} \simeq 0.4$ J

$J_{SCR} \simeq 0.05$ J

where $J \simeq 3.8 \times 10^{-2}$ A/cm^2 is the measured total dark current density at $V = V_{OC} = 617$ mV.

C. p^+-n-n^+ BSF cell

This cell was fabricated on about 7 Ωcm ($N_{DD} \simeq 6 \times 10^{14}$ cm^{-3}) float zone silicon wafer. The p^+-emitter is about 0.25 μm deep. The n^+-layer on the back is about 1 μm deep. Thickness of the cell was 320 μm. The details of the fabrication process are in Ref. 17.

The one-sun (AM0, 25°C) data were: $V_{OC} = 605$ mV, $J_{SC} = 39$ mA/cm^2. We will demonstrate here the use of the small-signal admittance method, described in Section III. Fig. 8 shows the measured dependencies of C and G on voltage V. The low frequency capacitance C_{LF} and conductance G_{LF} were measured at 500 Hz, C_{HF} was measured at 100 kHz using a Wayne-Kerr B224 bridge. Subtraction of these two dependencies yields $C_{QN} = C_{LF} - C_{HF}$ which follows the exp(qV/kT) dependence for about 2 decades. Similar procedure is used to extract G_{QN} [10]. Using a simple test described in Section IIIA we found that $G_{QNE} << G_{QNB}$. The hole lifetime is then obtained from (20) and S_{eff} from (16): $\tau_p \simeq 200$ μsec, $S_{eff} \simeq 80$ cm/sec. Using these values for τ_p and S_{eff}, we find that the first term in the parentheses in (16) is indeed small compared to the second term, which then validates (20). These results are consistent with measurements on p^+-n-n^+ cells reported by others [17, 18].

The advantages of calculating S_{eff} from C_{QN} (instead of from) G_{QN} are clearly evident in Fig. 8. The measured C_{LF} characteristic is almost an ideal one; the correction by subtracting C_{HF} is very small. On the other hand, the correction due to G_{SCR} to obtain G_{QN} is very substantial.

For V > 0.6 Volts the n-region of the base is in high-injection as shown by $G_{QN} \propto \exp(qV/2kT)$ for V > 0.6 Volts, which was obtained by subtracting G_{SCR} from G. The C_{LF} dependence on voltage for V > 0.6 Volts is also expected to be proportional to exp(qV/2kT). The C_{LF} in Fig. 8 shows, however, an excessive bending due to the contact resistance between the cell and the measurement probes. The C_{LF} was measured using only 2 probes, however 4 probe measurements are necessary to eliminate the contact resistance. Such capacitance measurements are possible. The series resistance R_s will have a negligible effect on C_{LF} [19]. The G-V curve was taken using 3 probe arrangement, effectively suppressing R_s for V < 0.7 Volts. Due to the difficulty with the high-injection value of C_{LF}, τ_H could not be found using the admittance method. The estimate of τ_H follows from recognizing that $G_{QNE} < G_{QNB}$ at V ≈ 600 mV, $W_n < L_p$ and S_{eff} is small. This will result in a nearly flat profile of P(x) in the n-base, and $I_B \approx Aqn_i W_n/\tau_H [\exp(qV/2kT)]$, which yields $\tau_H \approx 320$ μsec. The fact that $G_{QN} \propto \exp(qV/2kT)$ indicates that the low-doped portion of the base dominates the dark current at $V \approx V_{OC} = 605$ mV.

The results for this cell are summarized below:

$\tau_p \approx 200$ μsec;

$L_p \approx 500$ μm

$\tau_H \approx 320$ μsec

$S_{eff} \approx 80$ cm/sec (low injection)

$J_B \approx 0.8$ J

$J_{SCR} \approx 0.2$ J

$J_E \ll J_B$

$J_{B+} \ll J_B$

where $J \approx 2.9 \times 10^{-2}$ A/cm^2 is the measured total dark current density at $V = V_{OC} = 605$ mV.

VII. SUMMARY

This work presented new methods for determining the minority-carrier lifetime in narrow regions of solar cells. This leads to a simple analysis which results in determination of recombination currents in each region of the cell. Such an analysis was demonstrated for three different types of cells. The basewidth-modulation (BWM) and the small-signal admittance method involve measurements using very accurate admittance bridges. The accuracy of the BWM method depends on the accuracy with which τ_F can be determined from (4). This can be done very accurately for wide regions with a uniform doping. No other material parameter is required to obtain the lifetime from (3) or (8). Additional reasons for the high accuracy of this method are that it is independent of the currents not associated with the region in which the lifetime is measured and that it has a self-consistency check. The accuracy of the BWM method is estimated to be about $\pm$ 5%.

The lifetime measured by the small-signal admittance method, as determined from (20) or (25), does not require knowledge of any material parameter of the cell. The high frequency capacitance C_{HF} can be measured at relatively small frequencies ($\sim$100kHz) because of very long lifetimes in the measured cells. This allows measurements on large area devices ($\sim 1 cm^2$) using commerically available bridges. This method also has a self-consistency check. The total accuracy of this method is estimated to be about $\pm$ 10%. The dc current method is less accurate than the previous two methods, mainly if the emitter current is dominant.

The determination of lifetimes and recombination currents in the cell allows identification of regions that limit cell efficiency. It will also allow monitoring of fabrication steps and material properties.

REFERENCES FOR CHAPTER 5

1. J. Mandelkorn and J. H. Lamneck, Jr., "Simplified Fabrication of Back Surface Electric Field Silicon Cells and Novel Characteristics of Such Cells," in Record of 9th IEEE Photovoltaic Specialists Conf. pp. 66-72, 1972.

2. M. D. Lammert and R. J. Schwartz, "The Interdigitated Back Contact Solar Cell: A Silicon Solar Cell for Use in Concentrated Sunlight," IEEE Trans. Electron Devices, Vol. ED-24, pp. 337-342, April 1977.

3. O. von Roos and B. Anspaugh, "The front surface field solar cell, a new concept," Record of 13th IEEE Photovoltaic Specialists Conf., pp. 1119-1120, 1978.

4. S. Y. Chiang, B. G. Carbajal, and G. F. Wakefield, "Thin Tandem Junction Solar Cell," in Record of 13th IEEE Photovoltaic Specialists Conf. 78CH1319-3ED, 1978.

5. F. A. Lindholm, A. Neugroschel, S. C. Pao, J. G. Fossum, and C. T. Sah, "Design considerations for silicon HLE solar cells," in Record of 13th IEEE Photovoltaic Specialists Conf., pp. 1300-1305, 1978.

6. W. M. Bullis, NBS Technical Note 465, Nov. 1968.

7. J. H. Reynolds and A. Meulenberg, Jr., "Measurement of diffusion length in solar cells", J. Appl. Phys., Vol. 45, pp. 2582-2592, June 1974.

8. M. S. Birrittella, A. Neugroschel, and F. A. Lindholm, "Determination of the Minority-Carrier Base Lifetime of Junction Transistors by Measurements of Basewidth-Modulation," IEEE Trans. Electron Devices, Vol. ED-26, pp. 1361-1363, Sept. 1979.

9. A. K. Jonscher, Principles of Semiconductor Device Operation, New York: Willey, 1960.

10. A. Neugroschel, F. A. Lindholm, C. T. Sah, "A method for determining the emitter and base lifetimes in p-n junction diodes," IEEE Trans. Electron Devices, Vol. ED-24, pp. 662-671, June 1977.

11. A. Neugroschel, F. A. Lindholm, C. T. Sah, "Experimental determination of the stored charge and effective lifetime in the emitter of junction transistors," IEEE Trans. Electron Devices, Vol. ED-24, pp. 1362-1365, Dec. 1977.

12. J. R. Hauser and P. M. Dunbar, "Minority carrier reflecting properties of semiconductor high-low junctions," Solid-State Electron., Vol. 18, pp. 715-716, July 1975.

13. W. Shockley, "The theory of p-n junctions in semiconductors and p-n junction transistors," Bell Syst., Tech, J., Vol. 28, pp. 435-489, July 1949.

14. A. Neugroschel, P. J. Chen, S. C. Pao, and F. A. Lindholm, "Diffusion length and lifetime determination in p-n junction solar cells and diodes by capacitance measurements," IEEE Trans. Electron Devices, Vol. ED-25, pp. 485-490, April 1978.

15. W. Rosenzweig, "Diffusion length measurement by means of ionizing radiation," Bell Syst. Tech. J., Vol. 41, pp. 1573-1588, Sept. 1962.

16. C. F. Gay, "Thin silicon solar cell performance characteristics", Record of 13th IEEE Photovoltaic Specialists Conf., pp. 444-449, 1978.

17. J. G. Fossum, R. D. Nasby, and E. L. Burgess, "Development of High-Efficiency p^+-n-n^+ Back-Surface-Field Silicon Solar Cells", in Record of 13th IEEE Photovoltaic Specialists Conf., pp. 1294-1299, 1978.

18. J. G. Fossum, R. D. Nasby, and S. C. Pao, "Physics Underlying the Performance of Back-Surface-Field Solar Cells," to be published in IEEE Trans. Electron Devices, April 1980.

19. P. J. Chen, S. C. Pao, A. Neugroschel, F. A. Lindholm, "Experimental determination of series resistance of p-n junction diodes and solar cells," IEEE Trans. Electron Devices, Vol. ED-25, pp. 386-388, March 1978.

FIGURE CAPTIONS

Fig. 1 Basewidth-modulation effects in n^+-p-n^+ TJ cell.

Fig. 2 Schematic illustration of (a) n^+-p-p^+ BSF solar cell; (b) n^+-n-p HLE solar cell; and (c) the basic structure of the TJ (with floating front surface), FSF, and IBC cells.

Fig. 3 (a) Schematic diagram of a n^+-p-p^+ BSF cell; (b) Qualitative sketches of minority carrier distribution in dark.

Fig. 4 (a) Schematic diagram of a n^+-n-p HLE cell; (b) Qualitative sketches of minority carrier distribution in dark.

Fig. 5 (a) p^+-n-n^+ BSF cell and a modified transistor-like structure with a Schottky barrier collector, (b) n^+-p-p^+ BSF cell and a modified n^+-p-n^+ transistor-like structure.

Fig. 6 (a) Schematic diagram of TJ cell; (b) Schematic diagram of a n^+-p diode structure obtained from the TJ cell.

Fig. 7 Measured I_C, I_{BT}, G_0, and G_r versus forward bias V_{BE} for n^+-p-n^+ TJ cell. The base quasi-neutral current components are indicated by the dashed lines, I_{SCR} is the extrapolated SCR current component.

Fig. 8 Measured capacitance and conductance versus forward bias V for p^+-n-n^+ BSF cell. The quasi-neutral components are shown by the dashed lines, G_{SCR} is the extrapolated SCR conductance component.

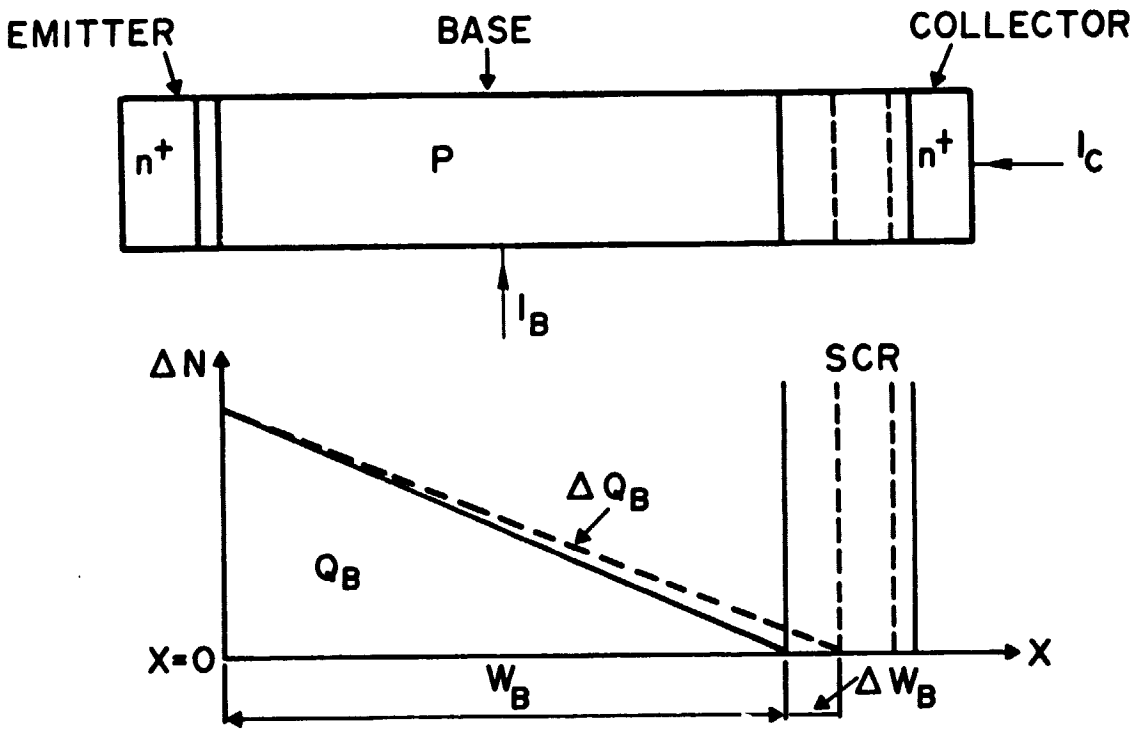
EMITTER
BASE
COLLECTOR
n+
P
n+
I_C
I_B
ΔN
SCR
ΔQ_B
Q_B
X=0
X
W_B
ΔW_B

FIGURE 1

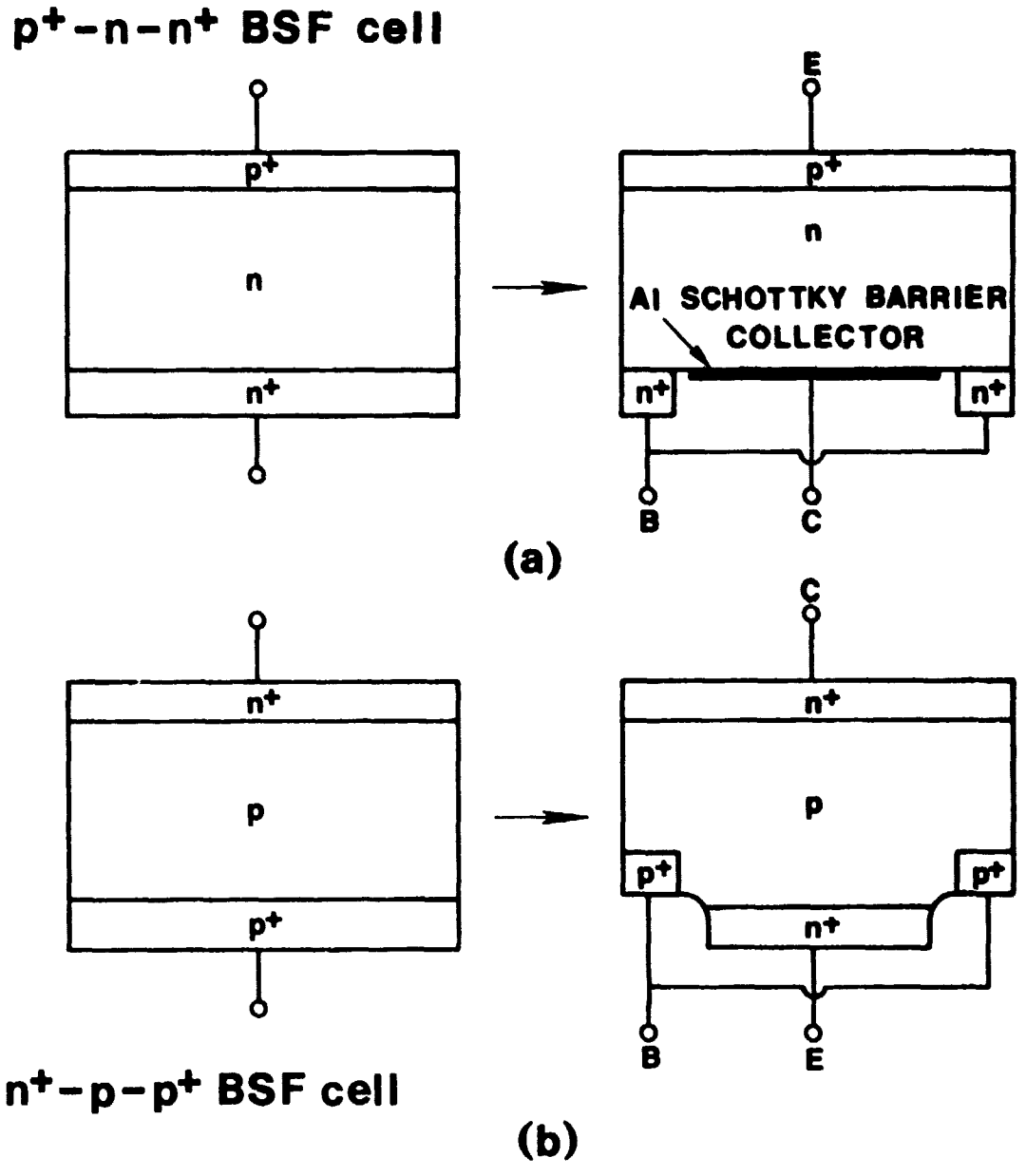
p+-n-n+ BSF cell
E
p+
n
Al SCHOTTKY BARRIER
COLLECTOR
n+
n+
B
C
(a)
C
n+
p
p+
n+
p+
n+
p
p+
B
E
n+-p-p+ BSF cell
(b)

FIGURE 2

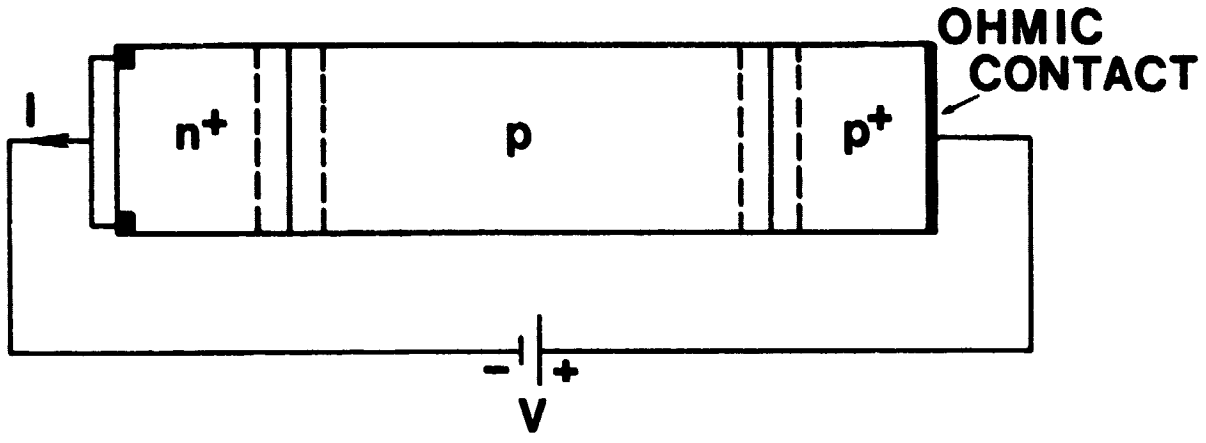

(a)

$$I = I_E + I_{SCR} + \frac{1}{\tau_n}\int_0^{W_p} N(x)\,dx + I_{B^+}$$

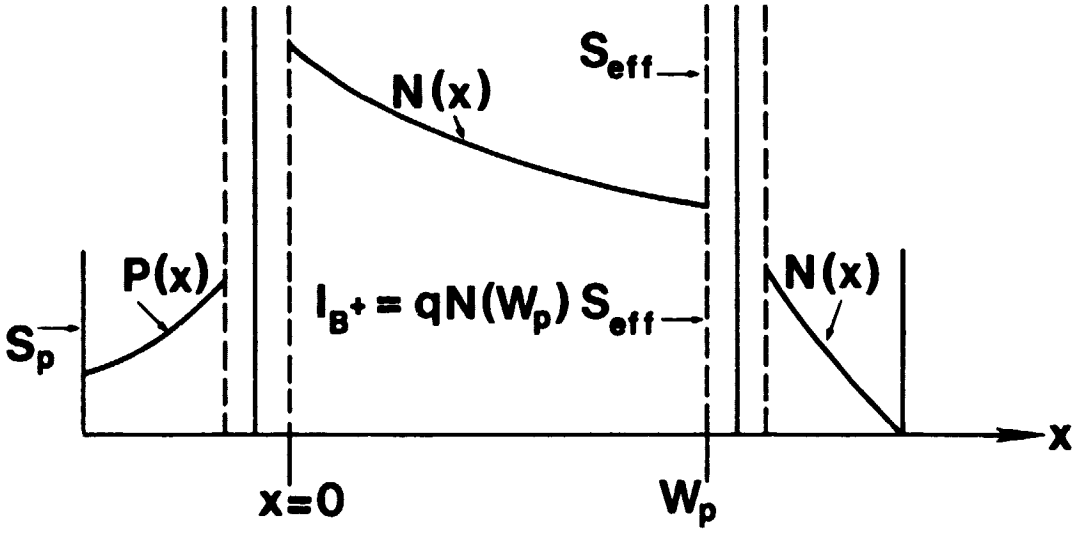

(b)

FIGURE 3

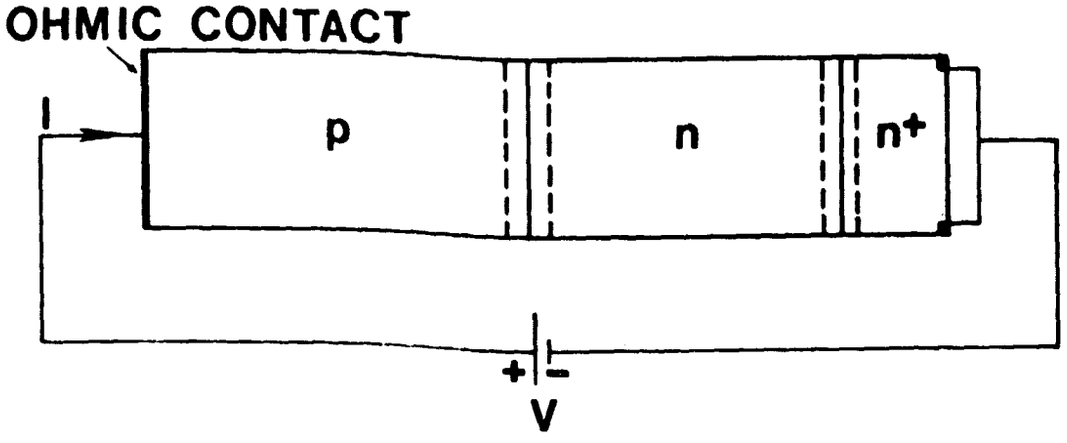

(a)

$$I = I_B + I_{SCR} + \frac{1}{\tau_p}\int_0^{W_n} P(x)\,dx + I_E$$

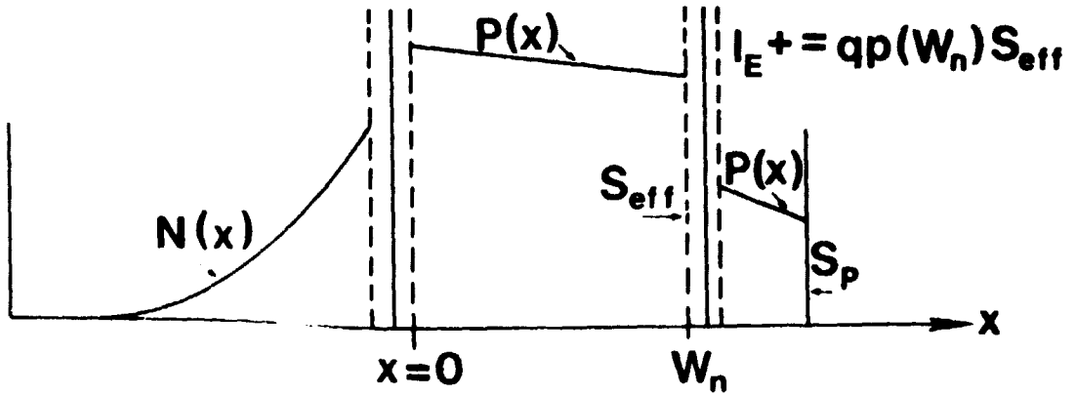

(b)

FIGURE 4

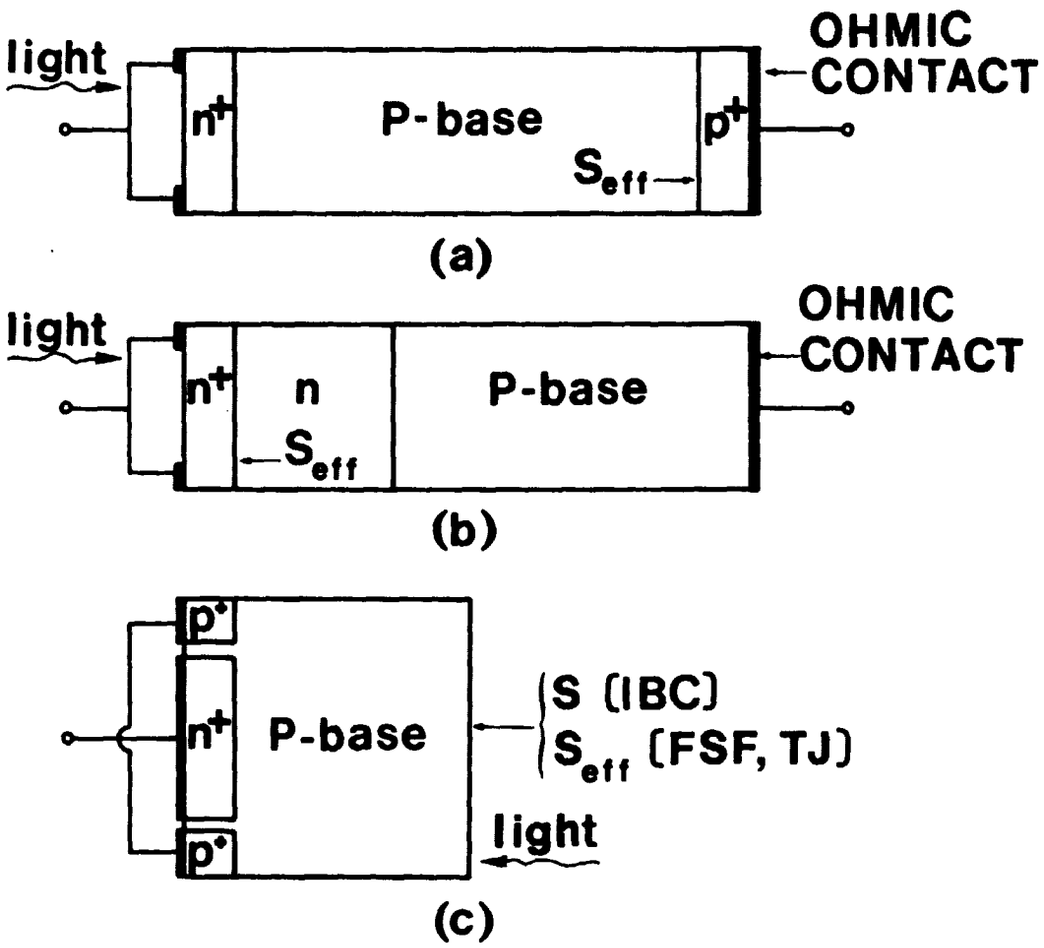
light
n+
P-base
p+
OHMIC
CONTACT
S_{eff}
(a)
light
n+
n
S_{eff}
P-base
OHMIC
CONTACT
(b)
p+
n+
P-base
p+
S (IBC)
S_{eff} (FSF, TJ)
light
(c)

FIGURE 5

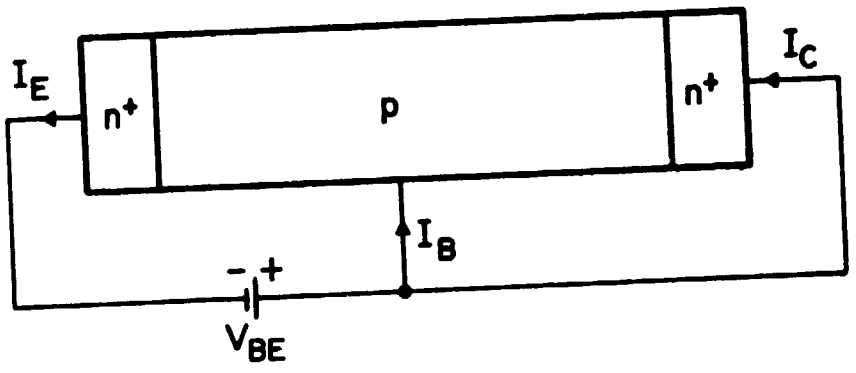

(a)

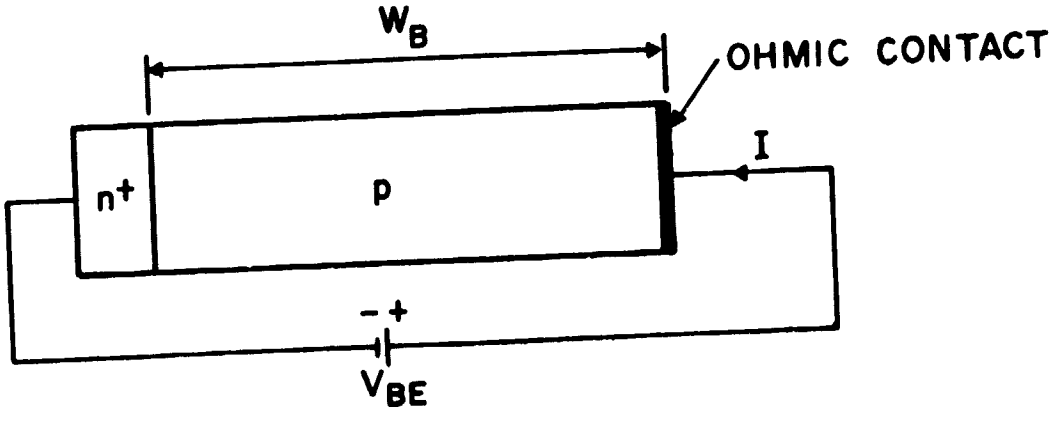

(b)

FIGURE 6

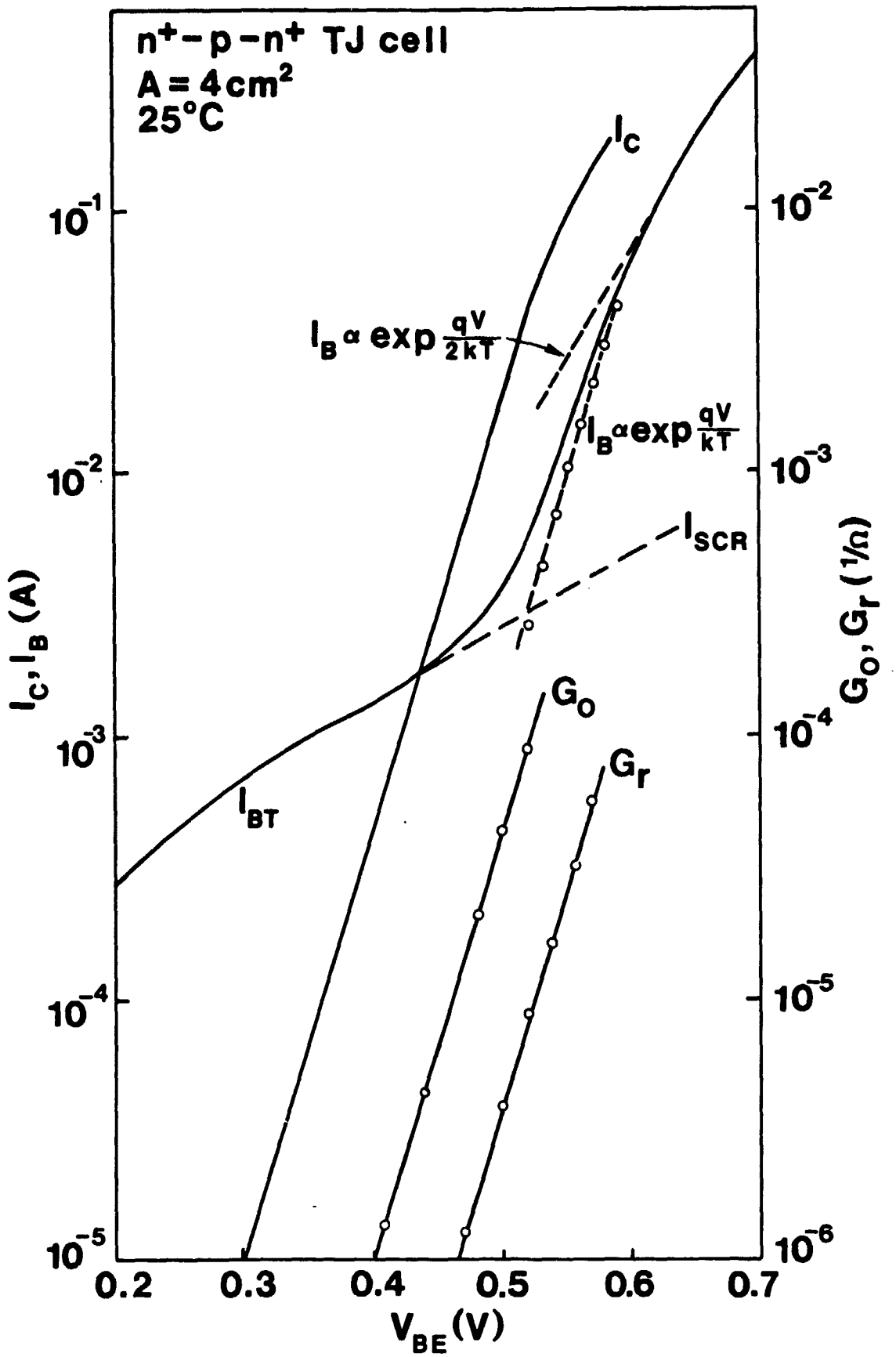
n+-p-n+ TJ cell
A = 4cm²
25°C
I_C
$I_B \alpha \exp \frac{qV}{2kT}$
$I_B \alpha \exp \frac{qV}{kT}$
I_{SCR}
I_{BT}
G_O
G_r
10^{-1}
10^{-2}
10^{-3}
10^{-4}
10^{-5}
10^{-2}
10^{-3}
10^{-4}
10^{-5}
10^{-6}
0.2
0.3
0.4
0.5
0.6
0.7
I_C, I_B (A)
G_O, G_r (1/Ω)
V_{BE} (V)

FIGURE 7

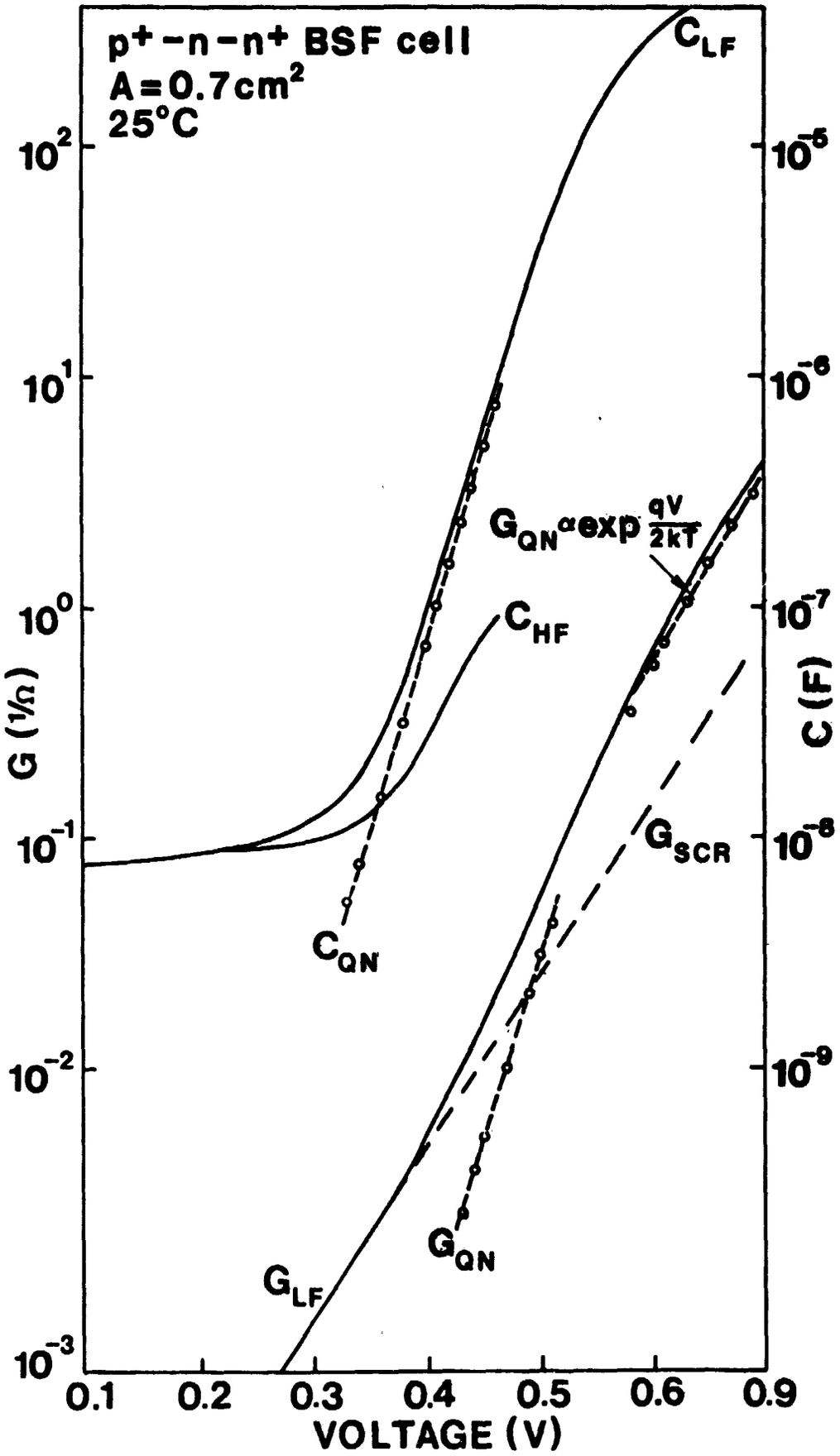
p+-n-n+ BSF cell
A=0.7cm²
25°C
C_LF
G_QN α exp qV/2kT
C_HF
G_SCR
C_QN
G_QN
G_LF
G (1/Ω)
C (F)
VOLTAGE (V)
10²
10¹
10⁰
10⁻¹
10⁻²
10⁻³
10⁻⁵
10⁻⁶
10⁻⁷
10⁻⁸
10⁻⁹
0.1
0.2
0.3
0.4
0.5
0.6
0.9

FIGURE 8

CHAPTER 6

MOS AND OXIDE-CHARGE-INDUCED (OCI) BSF SOLAR CELLS

I. Introduction

The power conversion efficiency of silicon p-n junction solar cells is limited mainly by the recombination currents from highly-doped regions of the cell. The advantages of replacing the highly-doped n^+-diffused emitter region by an electron accumulation layer was very successfully demonstrated recently in the oxide-charge-induced high-low-junction-emitter (OCI-HLE) solar cell [1]. In this particular cell a thermal oxide layer containing a positive oxide charge induces high-low-emitter junction, which together with the low surface recombination velocity resulting from the oxide layer effectively suppresses the emitter current. As a consequence, silicon solar cells with open-circuit voltages V_{OC} of 650 mV were made, which compares with the maximum value of about 600 mV seen in conventional silicon cells. Another demonstration of the desirability of avoiding a highly-doped n^+- emmitter region is provided by recent work in n^+-p MIS solar cells, in wich the oxide-charge-induced n^+-region is an inversion rather than an accummulation region. These devices show a maximum V_{oc} of 655 mV [2].

Fig. 1 shows a schematic diagram of a p^+-n-n^+ BSF cell [3]. As was noted above, the limiting factor in determining the cell efficiency of state-of-the-art silicon solar cells, including BSF cell, is the dark recombination current [4,5]. The dark current is a sum of a recombination currents from the quasi-neutral emitter and base regions. For a low-doped base ($\sim 10\,\Omega$ cm), typical of BSF cells, the emitter contribution is negligible [5]; the recombination current comes mainly from recombination in the n^+ region. The n^+-region current is [6]

$$J_P \approx \frac{qn_i^2}{N_{DD}} \frac{1}{\frac{W_B}{D_P} + \frac{1}{S_{eff}}} \left[\exp\left(\frac{qV}{kT}\right) - 1\right] \qquad (1)$$

where N_{DD} is the doping level in the low-doped part of the base, and S_{eff} is an effective recombination velocity at the n-n^+ low-high (L-H) boundary [6,7].

In the derivation of Eq. (1) we assumed a long diffusion length of minority holes in the low-doped part of the base: $L_p > W_B$. This is a necessary condi-

tion if the back-surface field is to have any considerable effect [8]. In addition, in the derivation of Eq.(1), the recombination current in the low-doped part of the base was neglected. This recombination current will ultimately limit the cell performance, as discussed in Section III. In present-day p^+-n-n^+ BSF cells of the best quality, in which the n^+-region is formed by phosphorus diffusion, the experimental values of S_{eff} are about 40 cm/sec [4]. This limits V_{OC} of present cells to about 615 mV at 300K for one-sun AM1 illumination. For this cell, $W_B \simeq 300$ μm, $D_p \simeq 40$ cm^2/sec, and $\tau_p \simeq 0.7$ msec [5] which implies that

$$J_p \simeq \frac{qn_i^2}{N_{DD}} S_{eff} \left[\exp\left(\frac{qV}{kT}\right) - 1\right] \quad . \tag{2}$$

Thus, reduction of J_p in this cell would result if S_{eff} could be lowered. The next section describes one approach for doing this.

II. MOS-BSF and OCI-BSF cells

Proposed device structures are shown in Figures 2(a) - (c). Instead of creating the L-H junction by the diffusion process, we suggest creating an accumulation layer at the back surface by a MOS gate structure, as in Figures 2(a) and 2(c). In the case of the p^+-n-n^+ structure, the accumulation layer can alternatively be induced by a positive oxide charge Q_0, as was done in OCI-HLE cell [1], Figure 2(b).

Since the accumulation layer is very thin, it will be essentially transparent to the minority holes (for p^+-n-n^+ structures, for example) which will recombine at the Si-SiO_2 interface, with a surface recombination velocity S_p [1,9]. The electron concentration in the base is shown in Fig. 2(d). The induced accumulation layer extends several Debye lengths from the surface, and thus can be as thin as 100 Å. For an electron concentration N_s at the Si-SiO_2 interface, S_{eff} can be written as [6]

$$S_{eff} \simeq \frac{N_{DD}}{N_s} S_p \quad . \tag{3}$$

As can be seen from Eq. (3), if the ratio S_p/N_s can be made small enough, J_p will be small.

Fig. 3 shows S_{eff} as a function of S_p for $N_{DD}=6\times10^{14}$ cm^{-3} at 300°K as a function of oxide charge density Q_0/q, or equivalent gate voltage V_G for SiO_2 thickness of 1000 Å. Values for N_s are calculated using standard MOS theory [10].

From Fig. 3 note that $V_G > 5$ Volts makes $S_{eff} < 40$ cm/sec even for S_p as large as 10^6 cm/sec. $S_{eff} = 40$ cm/sec was the value obtained for diffused n^+ regions [5]. The expected values for S_p for oxidized Si surfaces are much below 10^6 cm/sec. Therefore the MOS gate structure on the back side of the cell is expected to decrease J_p to a larger extent than that achieved in diffused p^+-n-n^+ cells. Thus V_{OC} is expected to increase because

$$V_{OC} \simeq \frac{kT}{q} \ell n \frac{J_{SC}}{J_{PO}} \quad . \tag{4}$$

Fig. 4 shows the dependence of V_{OC} on S_p at 300°K, for the proposed structures, calculated from Eqs. (1) and (4) (where the n-region recombination has been neglected for now) for $J_{SC}=35$ mA/cm^2 and $W_B=250$ μm. Values for V_{OC} larger than 650 mV result even for $S_p \simeq 10^5$ cm/sec provided $V_G \gtrsim 5$ Volts or $Q_0/q \gtrsim 1\times10^{12}$ cm^{-2}. Similar curves can be calculated for n^+-p-p^+ structures.

From two sets of experiments [11] with OCI-HLE cells, one which included thermal oxidation (dry and wet) of the front emitter surface at low temperatures (800-900°C) and a second which used chemical-vapor-deposition (CVD) of SiO_2 at 400°C, followed by heat treatment in oxygen, it was concluded that S_p for these low temperature oxides is about 10^5 cm/sec and $(Q_0/q)_{max}=7\times10^{11}$ cm^{-2}. Low-temperature oxides will have to be used for BSF cells, since high temperature treatments degrade the base material properties, mainly the diffusion length.

Very long diffusion lengths, at least as large as W_B, are necessary if the back-surface field is to have any considerable effect [8] and if the total recombination is to be low enough that $V_{OC} \approx 700$ mV is obtained.

Our experiments [11] and other published data indicate that Q_0/q is limited (for the standard process of thermally grown dry oxides followed by heat treatment in oxygen at about 700°C) to about 7×10^{11} cm^{-2} for (111) orientation [12,13] and to about 3×10^{11} cm^{-2} for (100) orientation [12]. Wet oxides grown at low temperatures (700°-900°C) have $Q_0/q \approx 5\times10^{11}$ cm^{-2} on a (111) surface [13]. CVD SiO_2 prepared at temperatures from 300 to 450°C and evaporated SiO have Q_0/q higher than that for thermally oxidized samples. Q_0/q for these oxides is about 2×10^{12} cm^{-2} [2,14]. However, these oxides have a much higher density of surface states, and thus higher S_p, than that typical of thermal oxides.

Therefore p^+-n-n^+ OCI-BSF cell which relies on oxide charge Q_0 and is made using the oxidation techniques described above may have V_{OC} limited to about 625 mV. Additional experiments are necessary to determine whether this is a real limitation or whether substantially larger V_{OC} can be obtained by these structures. On the other hand, the MOS-BSF structure, in which we apply a bias voltage to an MOS structure at the back side, has no apparent limitation to prevent achieving $V_{OC} \approx 700$ mV. Notice that for p^+-n-n^+ cells, one has the choice of using either Q_0 or V_G as the origin of the H-L junction. Because Q_0 is positive, in an n^+-p-p^+ cell, the gate-voltage approach is the only feasible one.

III. Discussion

As discussed in Section II, the recombination current in BSF cell can be very effectively suppressed by a back accumulation region at the $Si-SiO_2$ interface. If the currents in the back accumulation region and the emitter region are low enough, then the recombination currents in the low-doped base region and at the n-n^+ or p-p^+ diffused Ohmic junction will limit the maximum achievable V_{OC} and η.

Based on available experimental data for lifetimes for holes and electrons [5,15,16] we estimate that the base will not be an obstacle in achieving $(V_{OC})_{max} \simeq 700$ mV and $\eta_{max} \simeq 20\%$ for one-sun AM1 illumination. In this calculation, we accounted the high injection condition present in the low-doped base region.

Fabrication of the proposed structures will involve, over a small part of the area, diffusion of n^+or p^+-regions to insure good ohmic contact to the base, as shown in Fig. 2. Thus created n-n^+or p-p^+ junctions will contribute to the base recombination current. The recombination current density at the n-n^+ diffused junction, for example, is

$$J_{nn^+} \simeq q(n_i^2/N_{eff})(\bar{D}_p/W_{n^+})e^{qV/kT} \qquad (5)$$

where $N_{eff} \simeq 10^{18}$ cm^{-3} is the effective doping concentration including the effects of bandgap narrowing [17] due to heavy doping $\bar{D}_p$ is the average hole diffusivity in the n^+ region and W_{n^+} is the thickness of the n^+-region. In deriving Eq. (5), we have assumed that the hole diffusion length exceeds W_{n^+} in the n^+-region so that the n^+-region is nearly transparent to minority holes. From Eq. (5) we find that J_{nn^+} presents no obstacle to obtaining $V_{OC} \geq 700$ mV provided the area of n-n^+ junctions is 20% or less.

These predictions did not consider heavy-doping effects [17,18,19] which may occur in very strongly accumulated surfaces. Since the accumulation layer is very thin, these effects will be much less severe than in diffused junctions and are not expected to appreciably change our predictions.

The main advantage of the new MOS-BSF and OCI-BSF cells compared to conventional BSF cells is that using the Si-SiO_2 interface instead of an ohmic contact allows very low values of S_{eff} to be achieved at the L-H back junction, yielding large V_{OC} and improved J_{SC} [8,20]. Another advantage is the possibility of using CVD oxides deposited at low temperatures or evaporated oxides to create the MOS gate. The emitter diffusion in the n^+-p-p^+ BSF cell can be replaced by an induced n^+-inversion layer [2,14] which will allow complete fabrication of the cell at very low temperatures, possibly increasing the base lifetime in the finished device.

The disadvantage is that a voltage supply for gate bias V_G is required. No power will be consumed, since the oxide is a very good electrical insulator. The voltage can come from 10 to 30 conventional silicon cells in series, which can supply hundreds of the new proposed cells because no power is consumed by their MOS gate structure. As another disadvantage, additional photoresist steps on the back side are also necessary to define a contact pattern, which raises the cost.

We feel, however, that these disadvantages will be outweighted by increased performance of the cell, even for normal illumination levels. The performance of a BSF cell can improve with increasing of illumination level [5]. For high concentration application the increased cost of production due to additional steps required to produce this new device will become less important, since cost of a cell is very small compared to the cost of an entire system.

REFERENCES FOR CHAPTER 6

1. A. Neugroschel, F. A. Lindholm, S. C. Pao, and J. G. Fossum, "Emitter Current Suppression in a High-Low-Junction Emitter Solar Cell Using An Oxide-Charge-Induced Electron Accumulation Layer," Appl. Phys. Letters, vol. 33, pp. 168-170, July 15, 1978.

2. R. B. Godfrey and M. A. Green, "A 15% Efficient Silicon MIS Solar Cell", Appl. Phys. Letters, vol. 33, pp. 637-639, Oct. 1978; R. B. Godfrey and M. A. Green, "655 mV Open-circuit Voltage, 17.6% Efficient MIS Solar Cells", Appl. Phys. Letters, vol. 737, pp. 790-793, June 1, 1979.

3. J. Mandelkorn and J. H. Lamneck, Jr., "Simplified fabrication of back surface electric field silicon cells and novel characteristics of such cells", in Record of Ninth IEEE Photovoltaic Specialist Conf., pp. 66-72, 1972.

4. H. W. Brandhorst, "Silicon solar cell efficiency-practice and promise," in Record of Ninth IEEE Photovoltaic Specialists Conf., 1972.

5. J. G. Fossum, R. D. Nasby, and E. L. Burgess, "Development of High-Efficiency p^+-n-n^+ Back-Surface-Field Silicon Solar Cells," in Record of Thirteenth Photovoltaic Specialists Conf., pp. 1294-1299, 1978.

6. M. P. Godlewski, C. R. Baraona, and H. W. Brandhorst, "Low-high junction theory applied to solar cells", in Record of Tenth IEEE Photovoltaic Specialist Conf., 1973

7. J. R. Hauser and P. M. Dunbar, "Minority Carrier Reflecting Properties of Semiconductor High-Low Junctions," Solid-State Electron., vol. 18, pp. 715-716, July 1975.

8. J. G. Fossum, "Computer-aided numerical analysis of silicon solar cells", Solid-State Electron., vol. 19, pp. 269-277, 1976.

9. F. A. Lindholm, A. Neugroschel, S. C. Pao, J. G. Fossum, and C. T. Sah, "Design Considerations for Silicon HLE Solar Cells," in Record of Thirteenth IEEE Photovoltaic Specialists Conf., pp. 1300-1305, 1978.

10. R. H. Kingston and S. F. Neustadter, "Calculation of the space charge, electric field and free carrier concentration at the surface of semiconductors, J. Appl. Phys., vol. 26, pp. 718-720, June 1955.

11. A. Neugroschel, unpublished.

12. H. S. Fu and C. T. Sah, "Theory and experiments on surface 1/f noise", IEEE Trans. Electron Devices, vol. ED-19, pp. 273-285, Feb. 1972.

13. B. E. Deal, M. Sclar, A. S. Grove, and E. H. Snow, "Characteristics of the surface-State charge (Q_{ss}) of thermally oxidized silicon, J. Electrochem. Soc., vol. 114, pp. 266-274, March 1967.

14. R. E. Theriault and R. E. Thomas, "A low-temperature CVD oxide process for inversion layer-MIS solar cells, in IEDM Technical Digest, pp. 82-85, Dec. 1978.

15. D. Kendall, Conf. Physics and Application of Lithium Diffused Silicon, NASA-Goddard Space Flight Center, Dec. 1969.

16. P. A. Iles and S. I. Soclof, "Effect of Impurity Doping Concentration on Solar Cell Output", Record of Eleventh Photovoltaic Specialists Conf., pp. 19-24, 1975.

17. P. M. Dunbar and J. R. Hauser, "Theoretical Effects of Surface Diffused Region Lifetime Models on Silicon Solar Cells", Solid-State Electron, vol. 20, pp. 697-701, August 1977.

18. F. A. Lindholm and C. T. Sah, "Fundamental Electronic Mechanisms Limiting the Performance of Solar Cells", IEEE Trans. Electron Devices, vol. ED-24, pp. 299-304, April 1977.

19. H.P.D. Lanyon and R. A. Tuft," Bandgap Narrowing in Heavily Doped Silicon, in IEDM Technical Digest, pp. 316-319, Dec. 1978.

20. A. Sinha and S. K. Chattopadhyaya, "Effect of Back Surface Field on Photocurrent in a Semiconductor Junction", Solid-State Electron, vol. 21, pp. 943-951, July 1978.

Figure Captions

Fig. 1 Schematic diagram of a p^+-n-n^+ BSF solar cell.

Fig.2 Schematic diagram of MOS-BSF and OCI-BSF cell structures. (a) p_+-n-n_+ MOS-BSF cell, (b) p^+-n-n^+ OCI-BSF cell, (c) n^+-p-p^+ MOS-BSF cell, (d) concentration profile of minority carriers in the base.

Fig. 3. Effective surface recombination velocity S_{eff} versus surface recombination velocity S_p for SiO_2 thickness of 1000 Å.

Fig. 4 Open-circuit voltage V_{oc} versus surface recombination velocity S_p for SiO_2 thickness of 1000 Å, J_{sc} = 35 mA/cm^2 and W_B = 250μm.

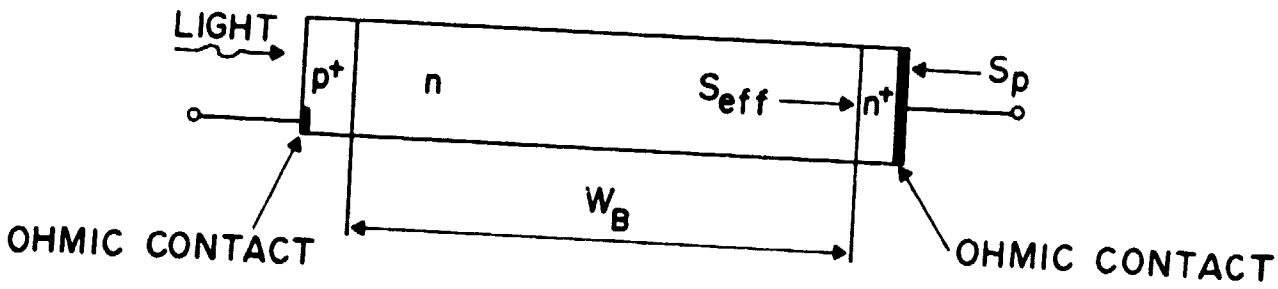

FIGURE 1

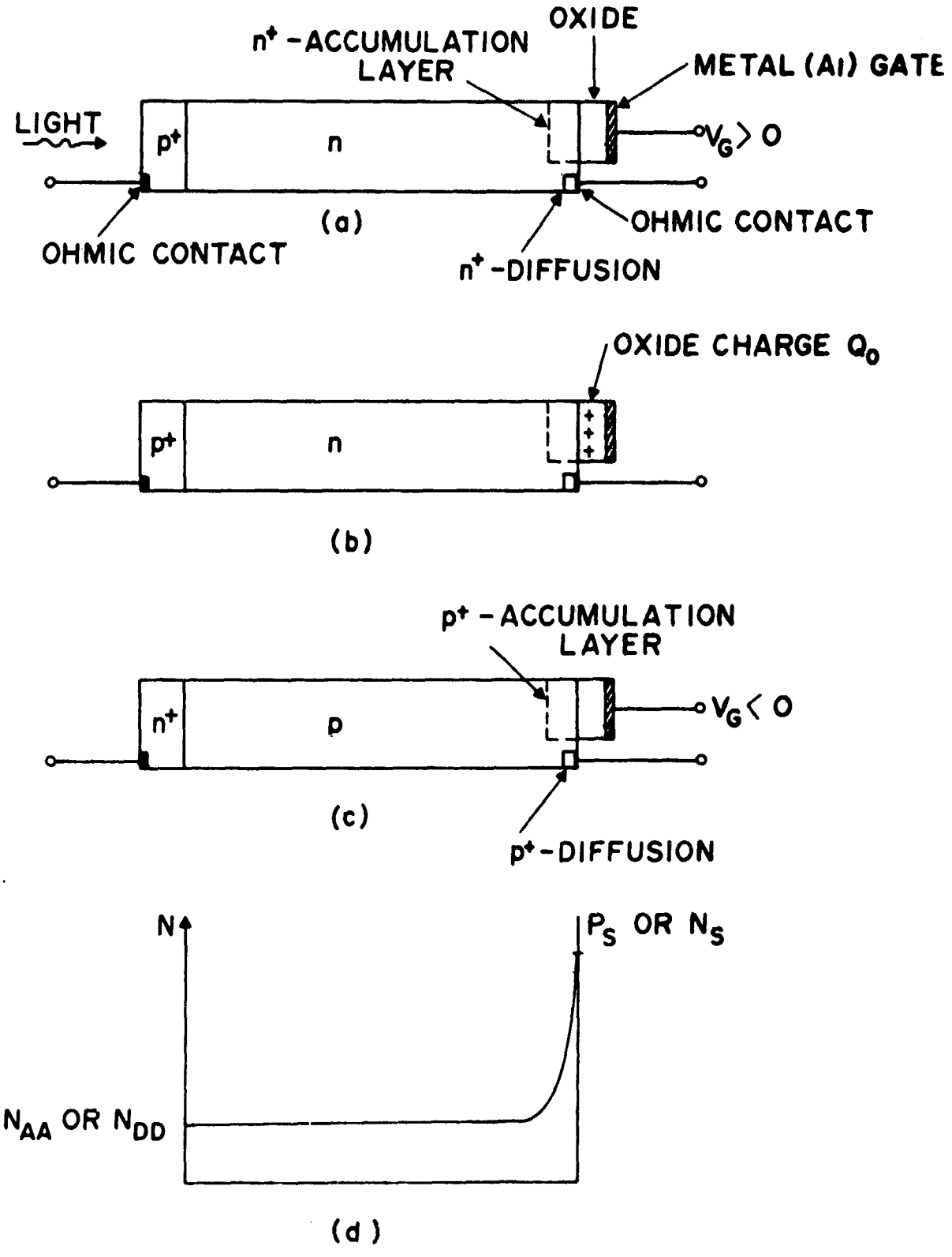
OXIDE
n+ -ACCUMULATION LAYER
METAL (Al) GATE
LIGHT
p+
n
VG > O
(a)
OHMIC CONTACT
OHMIC CONTACT
n+ -DIFFUSION
OXIDE CHARGE Q0
p+
n
(b)
p+ -ACCUMULATION LAYER
n+
p
VG < O
(c)
p+ -DIFFUSION
N
PS OR NS
NAA OR NDD
(d)

FIGURE 2

FIGURE 3

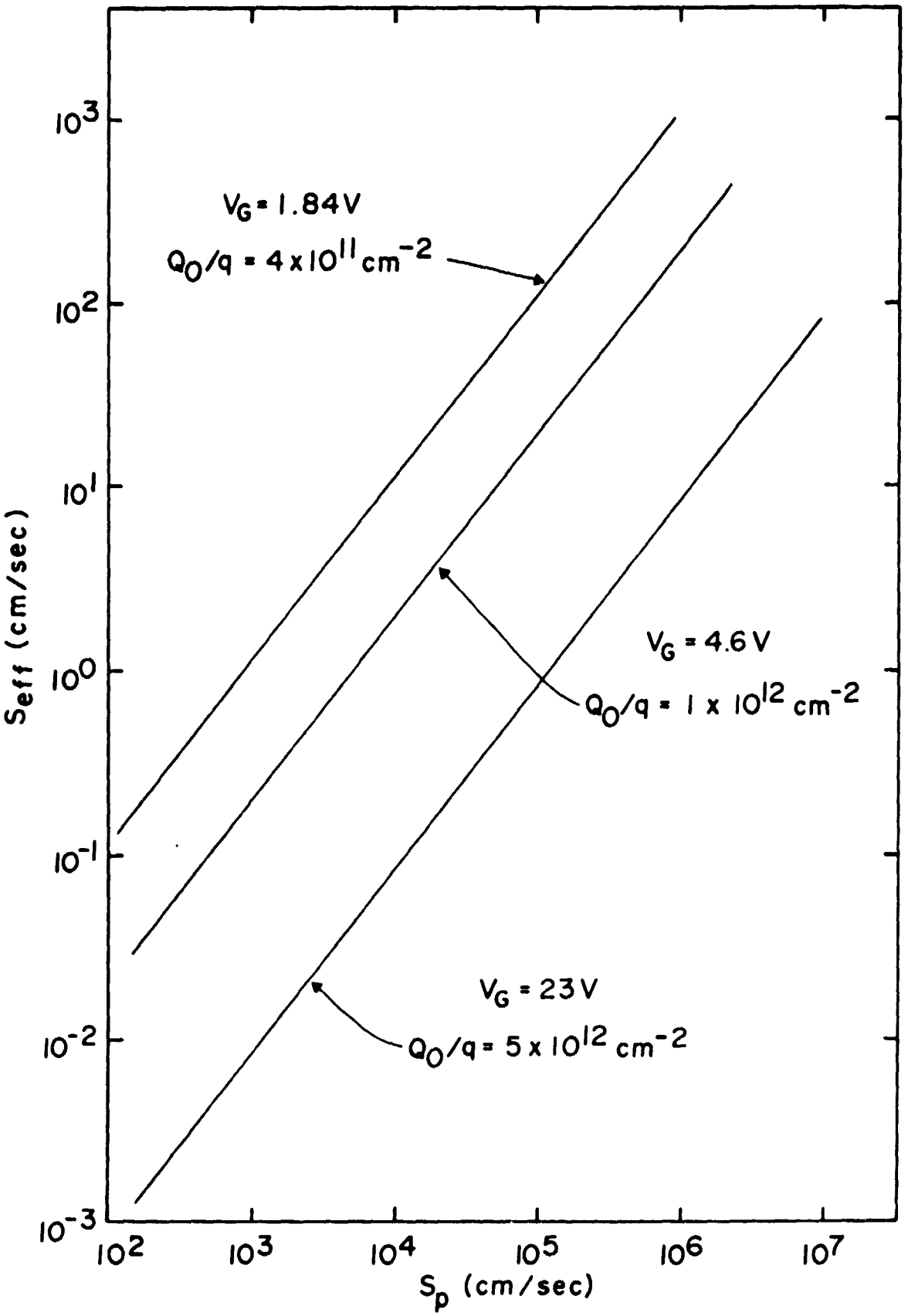
10^3
10^2
10^1
10^0
10^{-1}
10^{-2}
10^{-3}
S_{eff} (cm/sec)
V_G = 1.84V
$Q_O/q = 4 \times 10^{11}$ cm^{-2}
V_G = 4.6 V
$Q_O/q = 1 \times 10^{12}$ cm^{-2}
V_G = 23 V
$Q_O/q = 5 \times 10^{12}$ cm^{-2}
10^2
10^3
10^4
10^5
10^6
10^7
S_p (cm/sec)

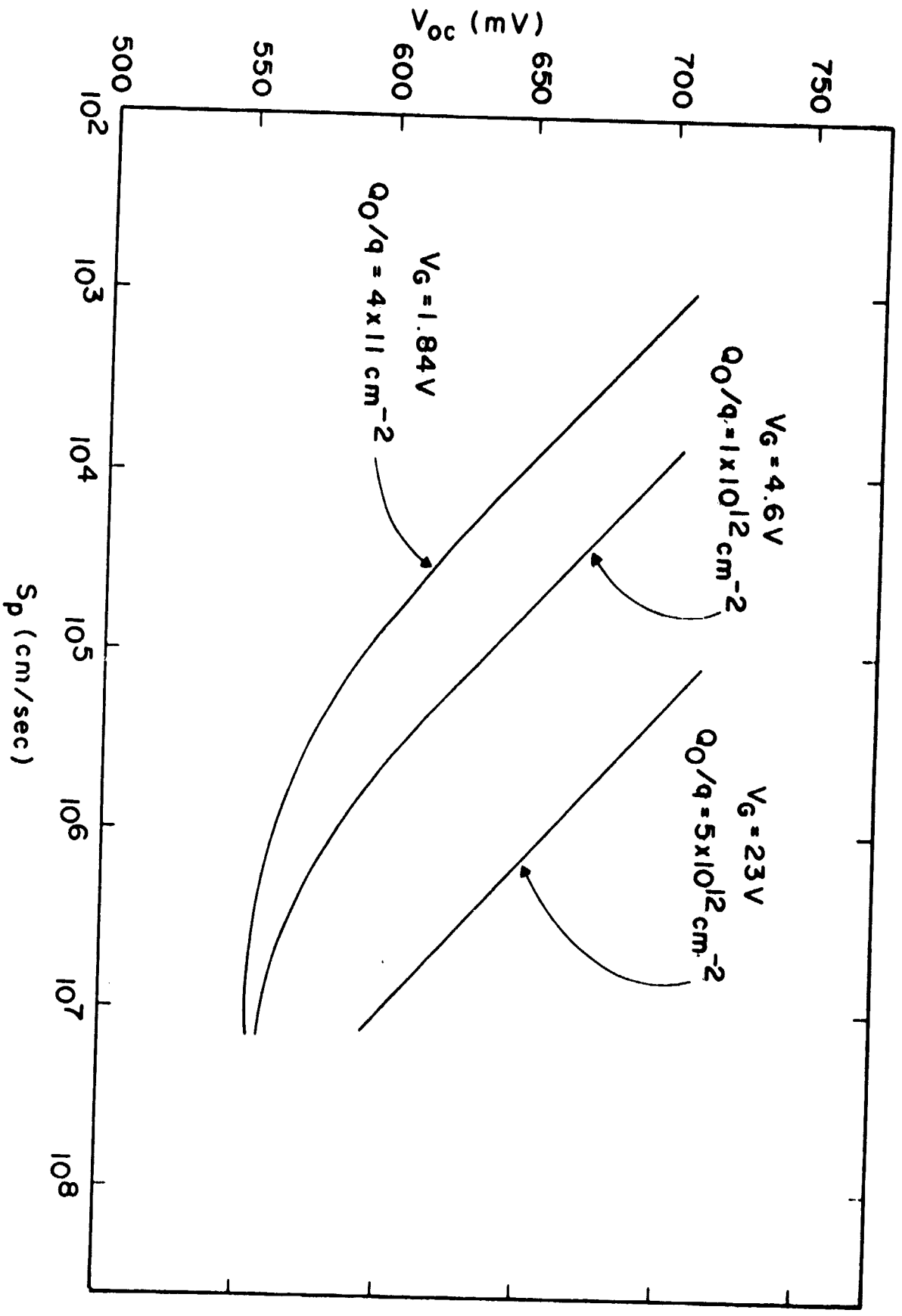
V_{oc} (mV)
500
550
600
650
700
750
10^2
10^3
10^4
10^5
10^6
10^7
10^8
S_p (cm/sec)
V_G = 1.84V
Q_O/q = 4x11 cm^{-2}
V_G = 4.6V
Q_O/q = 1x10^{12} cm^{-2}
V_G = 23V
Q_O/q = 5x10^{12} cm^{-2}

FIGURE 4

CHAPTER 7

DESIGN OF HIGH EFFICIENCY HLE SOLAR CELLS FOR SPACE AND TERRESTRIAL APPLICATIONS

1. INTRODUCTION

The purpose of this paper is to discuss design approaches for silicon HLE solar cells. Design of cells for radiation and terrestrial environments are considered. Two main types of HLE cells receive attention: (a) the oxide-charge-induced (OCI) HLE cell, and (b) a new HLE cell having a wide p-epitaxial emitter for which the appropriate choices of emitter width and doping levels in the emitter and base are made to yield both high V_{OC} and high J_{SC}.

SYMBOLS

D_a	ambipolar diffusivity (cm^2/sec)
D_n, D_p	electron and hole diffusivities (cm^2/sec)
Q_0	oxide charge density (C/cm^2)
J_{SC}	short circuit current density (A/cm^2)
J_{n0}, J_{p0}	dark electron and hole saturation current density (A/cm^2)
L_n, L_p	electron and hole diffusion length (cm)
Δn,Δp	excess electron and hole concentration (cm^{-3})

n_i	intrinsic carrier concentration (cm^{-3})
n_s, P_s	electron and hole surface concentration (cm^{-3})
$n_s(Q_0)$	oxide charge dependent electron surface concentration (cm^{-3})
N_{DD}, N_{DD}^+	donor concentration in n and n^+ material (cm^{-3})
N_{AA}, N_{AA}^+	acceptor concentration in p and p^+ material (cm^{-3})
q	electronic charge (Coulombs)
S_p	hole surface recombination velocity (cm/sec)
S_{eff}	effective surface recombination velocity (cm/sec)
T	temperature (^oC, ^oK)
V_A	applied voltage (Volts)
V_{OC}	open circuit voltage (Volts)
$(V_{OC})_B$, $(V_{OC})_E$	open circuit voltage established by base and emitter (Volts)
W_E	emitter thickness (cm)
X_j	junction depth (cm)
ρ	resistivity (Ω cm)
τ_n, τ_p	lifetime of minority electrons and holes (sec)
p, p^+	associated with p and p^+ region
n, n^+	associated with n and n^+ region
BOL	beginning-of-life
EOL	end-of-life
E, B	associated with emitter and base

II. OCI-HLE CELL

Fig. 1(a) shows the cross-section of an OCI silicon HLE solar cell. The principles of operation of this cell, which have previously been discussed [1] are illustrated in Figs. 1(a) and 1(b). A positive charge Q_0, achieved by suitable heat treatment [2,3], induces an electron accumulation and an electric field near the silicon surface which reduces the effective surface recombination velocity for holes S_{eff} to [4]

$$S_{eff} \approx \frac{N_{DD}}{n_s} S_p \quad . \tag{1}$$

By solving the hole continuity equation for the desired case, $W_E < L_p$, and low injection, one determines the hole saturation current J_{PO} to be [4]

$$J_{PO} \approx \frac{qn_i^2}{N_{DD}} \left[\frac{S_{eff} + \frac{W_E}{\tau_p}}{1 + \frac{S_{eff}}{D_p/W_E}} \right] \qquad (2)$$

in which the first term in the numerator accounts for hole recombination at the surface and the second term accounts for hole recombination in the bulk. The current J_{PO} must be small if high V_{OC} is to result.

2.1 Beginning of life - (BOL) Design

For BOL, our experiments [1] show that $S_p < 10^4$ cm/sec can result from the presence of the SiO_2 layer on the illuminated surface. For a wide range of doping levels N_{DD}, the term W_E/τ_p in (2) can be made negligible, and the diffusion velocity D_p/W_E will typically be of the order of 10^4 cm/sec. Thus, if S_{eff} can be made much less than 10^4 cm/sec, then (2) reduces to

$$J_{PO} \approx \frac{qn_i^2}{N_{DD}} S_{eff} \approx qn_i^2 \frac{S_p}{n_s} \quad , \qquad (3)$$

which also holds for high injection provided D_a/W_E and $W_E/(\tau_n + \tau_p)$ are both small compared with $(S_{eff})_{high\ injection} = (n_i/n_s) \exp qV_A/2kT$, as can be shown by solving the ambipolar transport equation for high injection [5]. To show that $S_{eff} < 10^4$ cm/sec is possible, we indicate in Fig. 2, for different values of N_{DD} and Q_0, the resulting values of n_s and S_{eff}. The functional dependence $n_s(Q_0)$ is found from standard MOS theory [6].

Because S_{eff} can be small, we consider now the value of J_{PO} for the limiting case $S_{eff} = 0$. Fig. 1(b) shows the minority hole density in the dark cell, resulting from an applied voltage, for the desired condition, $L_p > W_E$:

$$J_{PO} \approx qn_i^2 \, W_E (N_{DD}\tau_p)^{-1} \quad . \qquad (4)$$

To estimate J_{PO}, we use the empirical data of Kendall [7], which gives, for $N_{DD} \geq 5 \times 10^{16} cm^{-3}$,

$$\tau_p N_{DD} \approx 3 \times 10^{12} \ sec/cm^{-3} \quad . \qquad (5)$$

Thus, at $T = 25^{\circ}C$,

$$J_{pO} \simeq 7 \times 10^{-12} W_E \quad . \tag{6}$$

Thus, if $J_{SC} \simeq 35$ mA/cm^2(AMO), which was seen in OCI-HLE cells, the open-circuit voltage limit, $(V_{OC})_E = kT/q \, \ell n(J_{SC}/J_{pO})$, established by the emitter current J_{pO} is, for example, 800 mV, 780 mV, and 718 mV for $W_E = 2$ μm, 5 μm, and 50 μm, respectively, independent of N_{DD} (provided low-injection levels are maintained). From a design viewpoint, this demonstrates that $(V_{OC})_E > 700$ mV can be achieved for a wide variety of choices of N_{DD} and W_E provided only that $L_p > W_E$.

2.2 End-of-Life (EOL) Design

Radiation damage increase S_p and Q_0[8]; it will also reduce τ_p[9,10]. As a design approach, we choose W_E small compared with anticipated degraded diffusion length to minimize bulk recombination; that is, we require $W_E < L_p$ (after irradiation). Then (2) still applies, and J_{pO} is determined by the velocities S_{eff}, W_E/τ_p, and D_p/W_E. As a worst-case limit, we consider the case $S_{eff} = \infty$. Then the transit time t_t for holes to cross the emitter is

$$t_t = W_E^2/2D_p \tag{7}$$

which, for example, is of the order of 10^{-9}sec for $W_E \simeq 2$ μm. Thus,if τ_p after irradiation is larger than 10^{-9} sec, the emitter will be transparent to holes and (2) reduces to

$$J_{pO} = \frac{qn_i^2}{N_{DD}} \frac{D_p}{W_E} \quad . \tag{8}$$

This worst-case dependence suggests that N_{DD} should be large enough, both to assure small lateral series resistance and to decrease J_{pO}, but small enough to avoid heavy-doping degradation. For example, consider a design with $W_E = 2$ μm, and $N_{DD} = 10^{18}$ cm^{-3}. For $T = 25^{\circ}C$ and $J_{SC} \simeq 25$ mA/cm^2, $(V_{OC})_E > 640$ mV. For electron fluences up to 10^{15} cm^{-2}, $J_{SC} \simeq 25$ mA/cm^2 is expected if prior to radiation $J_{SC} \simeq 35$ mA/cm^2[10].

2.3 Examples of V_{OC} established by the emitter for BOL and EOL

We have previously discussed $(V_{OC})_E$ for two limiting cases: $S_{eff} = 0$,

which corresponds to the BOL condition, and $S_{eff} = \infty$, which corresponds to the EOL condition. We now remove these limiting-case assumptions by considering intermediate values of S_{eff}, as determined by (1) and the condition that 10^3 cm/sec $\leq S_p \leq 10^7$ cm/sec. The lower bound on S_p is easily achieved, as is indicated by our experiments for a surface passivated by SiO_2 [1]. The upper bound is a theoretical limit for a silicon surface [11].

In Fig. 3 we plot $(V_{OC})_E$ as a function of S_p for two values of emitter widths $W_E = 2.5$ μm and 15 μm and for emitter doping densities of $N_{DD} = 10^{17}$ cm^{-3} and 10^{18} cm^{-3}. Three values of oxide charge densities are considered: (a) $Q_0/q = 4 \times 10^{11}$ cm^{-2}, which is the order of magnitude obtained in thermally grown dry oxides followed by oxygen heat treatment at about 700 C [2,3] before the irradiation; and $Q_0/q = 1 \times 10^{12}$ cm^{-2} and 5×10^{-12} cm^{-3}, which is the range of values expected after irradiation [8]. As shown in Fig. 3 for BOL with $S_p \approx 10^3$ cm/sec, the emitter recombination is no barrier for achieving $(V_{OC})_E \gtrsim 700$ mV for variety of emitter doping levels and thicknesses. After irradiation, for EOL, S_p is expected to increase significantly [8], but will not be larger than the order of 10^6 cm/sec [11]. But Q_0/q will also increase, as mentioned above, which will increase n_s [6], and $S_{eff} \approx N_{DD} S_p/n_s (Q_0)$ will depend on the ratio $S_p/n_s (Q_0)$ after the irradiation. It follows from Fig. 3, consistent with our previous worst-case calculation, that $(V_{OC})_E > 650$ mV is still possible at EOL, if $W_E < (L_p)_{EOL}$.

2.4 V_{OC} established by the base for BOL and EOL

As shown in Fig. 1(b) for the dark case with applied voltage V_A, the quasi-neutral saturation current J_0 in low injection, neglecting heavy-doping effects [12], is $J_0 = J_{p0} + J_{n0}$, and the base saturation current is

$$J_{n0} = \frac{q n_i^2 D_n}{N_{AA} L_n} \quad . \tag{9}$$

To minimize J_{n0}, note that, for $N_{AA} \gtrsim 10^{17}$ cm^{-3}, $D_n/N_{AA}L_n$ is a decreasing function of N_{DD} [13], provided heavy doping effects are negligible. As a result, the open-circuit voltage limited by the base $(V_{OC})_B$ is an increasing function of N_{DD} until $N_{AA} \approx 10^{19}$ cm^{-3} ($\rho_{base} \approx 0.01$ Ωcm) which is a doping level at which the heavy doping effects in p-type material become important [12], as shown in

Fig. 4. The broken line in Fig. 4 shows an experimental dependence of V_{OC} on N_{AA} [14] which peaks at $N_{AA} \simeq 5 \times 10^{17}$ cm^{-3}. This is a result of the increasing importance of the emitter current J_{pO}, for base dopings larger than about 5×10^{17} cm^{-3}, in conventional cell where the emitter current is not suppressed by an HLE structure such as that present in the proposed device.

3. Design concepts for space and terrestrial applications

Based on the foregoing analysis we present design concepts for two different types of space cells and for a terrestrial cell.

1) n^+-n-p OCI-HLE (diffused HLE) space cell

Fig. 5 shows a cell designed for space applications. The p-type base doping is $N_{AA} \simeq 5 \times 10^{17}$ ($\rho \simeq 0.1$ Ωcm) which appears to be an optimum value which gives L_n in a range of 85-150 μm in a finished cell [15]. This long diffusion length, which will assure collection of most of the generated minority electrons, provides a high value of the short circuit current J_{SC}. The epitaxial emitter is narrow, about 2 μm, and highly doped, $N_{DD} \simeq 10^{17}$ to 10^{18} cm^{-3}, to assure low series resistance. The thinness of the emitter offsets, to a large degree, the effects of significant degradation of lifetime in the n-type material after the irradiation [9]. The H-L emitter junction can be achieved using either OCI induced or diffused n^+ layer [16].

The following conclusions about this structure can be made based on the discussion in the previous sections:

a) $(V_{OC})_E > 650$ mV at EOL, if $t_t < (\tau_p)_{EOL}$.

b) $(V_{OC})_B$ at EOL will depend on the radiation damage [10]. Since the base is the same as in the conventional n on p cell, results obtained for the conventional cell radiation damage [10] also apply here.

c) $(J_{SC})_{EOL} = (J_{SC})_{\substack{\text{conventional} \\ \text{base}}} + (J_{SC})_E$.

d) For an OCI structure, $S_{eff} \simeq N_{DD}\, S_p/n_s$, where both S_p and n_s increase with radiation, thus tending to keep S_{eff} low. S_{eff} controls $(J_{SC})_E$ and J_{pO}.

e) For BOL, with $S_p \simeq 10^3$ cm/sec, $(V_{OC})_E > 700$ mV, and $(V_{OC})_B$ depends on minimizing $D_n/L_n\, N_{AA}$. $(V_{OC})_B$ of the order of 700 mV can be expected for $\rho_{base} \simeq 0.1$ Ωcm with $L_n > 75$ μm.

f) For $Q_0/q > 10^{12}$ cm^{-2}, heavy doping effects in the accumulation layer may become important (Fig. 2). However, since the accumulation layer is very narrow, these effects are expected to be very small [17].

g) A structure with a diffused n^+-region offers larger flexibility in choosing N_{DD} because of the low shunting resistance of the n^+-diffused layer.

2) A wide-emitter p^+-p-n^+ space cell

We propose a new silicon solar cell structure [18] which is projected to have both high J_{SC}(45 mA/cm^2) and high V_{OC}(700 mV) and consequently high η (20%, AM0). The new structure is projected to have good performance in radiation as well as non-radiation environments.

The structure is shown in Fig. 6. The qualitative sketches showing the minority carrier distributions in Fig. 1 are valid for this case, too, with hole and electron profiles reversed.

We emphasize some special features of this structure:

a) The surface is passivated with SiO_2 on top of which a suitable antireflection (AR) coating is deposited. The H-L emitter junction is achieved by a thin ($\sim$0.1 μm) p^+-diffused layer resulting in [4]

$$S_{eff} \simeq S_n \frac{N_{AA}}{(N^+_{AA})_{eff}} \qquad (10)$$

where $(N^+_{AA})_{eff} \simeq 10^{19}$ cm^{-3} is the effective doping in the p^+-diffused layer for $N^+_{AA} \simeq 10^{20}$ cm^{-3} at the surface. An electron recombination velocity at the Si-SiO_2 interface on the order of 10^3 or less can be easily achieved [1]. Therefore, for $N_{AA} = 5 \times 10^{17}$ cm^{-3}, S_{eff} is of the order of 10 cm/sec or less; thus $S_{eff} \simeq 0$ is a reasonable approximation.

b) As a result of $S_{eff} \simeq 0$, and the choice of a 50 μm wide emitter region, about 90% [19] of all available optically generated minority electrons will be collected. Using a 5% loss AR coating and 4% metal coverage the projected AM0 $J_{SC} \simeq 45$ mA/cm^2. P-type material is chosen as a region from which the J_{SC} is collected due to smaller sensitivity to the radiation than seen in n-type material [9].

c) The doping level in the n^+-base is optimized to be about 10^{18} cm^{-3}, which is the onset level for heavy-doping effects [17]. The doping

level in the emitter ($\sim 5 \times 10^{17}$ cm^{-3}) is chosen to minimize $N_{AA}\tau_n$ [13].

d) Using published data for lifetimes for holes and electrons [7,13], we can calculate by use of Eqs. (2) and (9), for structure shown in Fig. 6, that the saturation current $J_0 \lesssim 7 \times 10^{-14}$ A/cm^2, implying $V_{OC} \simeq 700$ mV for $J_{SC} = 45$ mA/cm^2 at 25 C, and implying $\eta \simeq 20\%$ AMO.

e) Significant differences exist between this new cell and a previously proposed epitaxial p^+-p-n cell [20]; these are discussed in detail in Ref. 18.

f) An alternative related structure (p^+-p-n-n^+) can be made, which employs an n-n^+ low-high junction back-surface-field base [4]. This structure will have higher J_{SC} at BOL due to improved collection of minority holes from the n-region of the base.

3) n^+-n-p OCI-HLE terrestrial cell (Fig. 1)

There are two approaches to minimize the base current in this cell, Fig. 7:

a) Choose $\rho_{base} \simeq 0.1$ Ωcm ($N_{AA} \simeq 5 \times 10^{17}$ cm^{-3}). In this case $L_n \gtrsim 70$ μm is required for $(V_{OC})_B \simeq 700$ mV 25°C and $J_{SC} = 35$ mA/cm^2. Such values for L_n can be achieved in finished cells using a low temperature fabrication process [13,15]. Epitaxial growth of the emitter and a high-temperature oxidation required for low S_p [1] may decrease L_n below the 70 μm; this would result in $(V_{OC})_B < 700$ mV. The largest V_{OC} seen experimentally for a cell with $\rho_{base} \simeq 0.1$ Ωcm is 643 mV AMO, at 25°C.

b) A second approach is to use a highly doped p-type (5×10^{18} - 10^{19}cm^{-3}) base. Note that for $N_{AA} = 5 \times 10^{18}$ cm^{-3}, for example, $L_n \simeq 2$ μm is sufficient to achieve $(V_{OC})_B$ of 700 mV. Such values are expected even after the high-temperature fabrication steps. In this second approach, $W_E \simeq 50$ μm, since the base will contribute negligibly to J_{SC}. Such a wide emitter is required to collect about 90% of generated minority holes. In approach (a), W_E can range from about 10 to 50 μm. The largest V_{OC} seen experimentally for a cell with $\rho_{base} \simeq 0.024$ Ωcm ($N_{AA} \simeq 2.5 \times 10^{18}$ cm^{-3}) is 647 mV AMO, at 25°C.

c) Emitter doping can be chosen from range of about 5×10^{16} cm^{-3} to about 5×10^{17} cm^{-3}.

CONCLUDING REMARKS

First order analysis of HLE solar cells for BOL and EOL conditions is presented. Based on this analysis and on experimentally measured material parameters, design concepts for both space and terrestrial cells are discussed. The proposed structures include: n^+-n-, OCI-HLE space cell, wide emitter p^+-p-n^+ space cell, and n^+-n-p OCI-HLE terrestrial cell . All structures are projected to yield both high V_{OC} and J_{SC}.

REFERENCES FOR CHAPTER 7

1. Neugroschel, A., Lindholm, F. A., Pao, S. C, and Fossum, J. G., "Emitter Current Suppression in a High-Low-Junction Emitter Solar Cell Using An Oxide-Charge-Induced Electron Accumulation Layer," Appl. Phys. Letters, vol. 33, July 15, 1978, pp. 168-170.

2. Deal, B. E., Sclar, M., Grove, A. S., and Snow, E. H., "Characteristics of the surface-state charge (Q_{ss}) of thermally oxidized silicon, J. Electrochem. Soc., vol. 114, March 1967, pp. 266-274.

3. Fu, H. S. and Sah, C. T., "Theory and experiments on surface 1/f noise", IEEE Trans. Electron Devices, vol. ED-19, Feb. 1972, 273-285.

4. Godlewski, M. P., Baraona, C. R., and Brandhorst, H. W., "Low-high junction theory applied to solar cells", in Record of Tenth IEEE Photovoltaic Specialist Conf., 1973.

5. Lindholm, F. A., Fossum, J. G., and Burgess, E. L., "Application of the superposition principle to solar-cell analysis", IEEE Trans. Electron Devices, vol. ED-26, March 1979, pp. 165-171.

6. Kingston, R. H. and Neustandter, S. F., "Calculation of the space charge, electric field and free carrier concentration at the surface of semiconductors, J. Appl. Phys., vol. 26, June 1955, pp. 718-720.

7. Kendall, D., Conf. Physics and Application of Lithium Diffused Silicon, NASA-Goddard Space Flight Center, Dec. 1969.

8. Zaininger, K. H. and Holmes-Siedle "A survey of radiation effects in metal-insulator-semiconductor devices", RCA Rev., vol. 28, 1967, pp. 208-241.

9. Cooley, W. C. and Janda, R. J., "Handbook of space-radiation effects on solar-cell power systems", NASA Report SP-3003, 1963.

10. Tada, H. Y. and Carter, J. R., "Solar cell radiation handbook", JPL Publication 77-56, 1977.

11. Heasell, E. L., "Recombination beneath ohmic contacts and adjacent oxide covered regions", Solid-State Electron., vol. 22, Jan. 1979, pp. 89-93.

12. Dunbar, P. M. and Hauser, J. R., "Theoretical effects of surface diffused region lifetime models on silicon solar cells", Solid-State Electron., vol. 20, August 1977, pp. 697-701.

13. Iles, P. A. and Soclof, S. I., "Effect of impurity doping concentration on solar cell output, in Record of Eleventh Photovoltaic Specialist Conf., 1975, pp. 19-24.

14. Godlewski, M. P., Brandhorst, H. W., and Baraona, C. R., "Effects of high doping levels on silicon solar cell performance", in Record of Eleventh Photovoltaic Specialists Conf., 1975, pp. 32-35.

15. Brandhorst, H. W. and Godlewski, M. P., private communication.

16. Lindholm, F. A., Neugroschel, A., Pao, S. C., Fossum, J. G., Sah, C. T., "Design Considerations for Silicon HLE Solar Cells", in Record of Thirteenth IEEE Photovoltaic Specialists Conf., 1978, pp. 1300-1305.

17. Lanyon, H. P. D. and Tuft, R. A, "Bandgap narrowing in heavily doped silicon", IEDM Technical Digest, Dec. 1978, pp. 316-319.

18. Neugroschel, A. and Lindholm, F. A., submitted for publication to IEEE Trans. Electron Devices.

19. Fossum, J. G., "Computer-aided numerical analysis of silicon solar cells", Solid-State Electron., vol. 19, April 1976, pp. 269-277.

20. D'Aiello, R. V., Robinson, P. H., and Kressel, H., "Epitaxial silicon solar cells", Appl. Phys. Letters, vol. 28, 15 Feb., 1976, pp. 231-234.

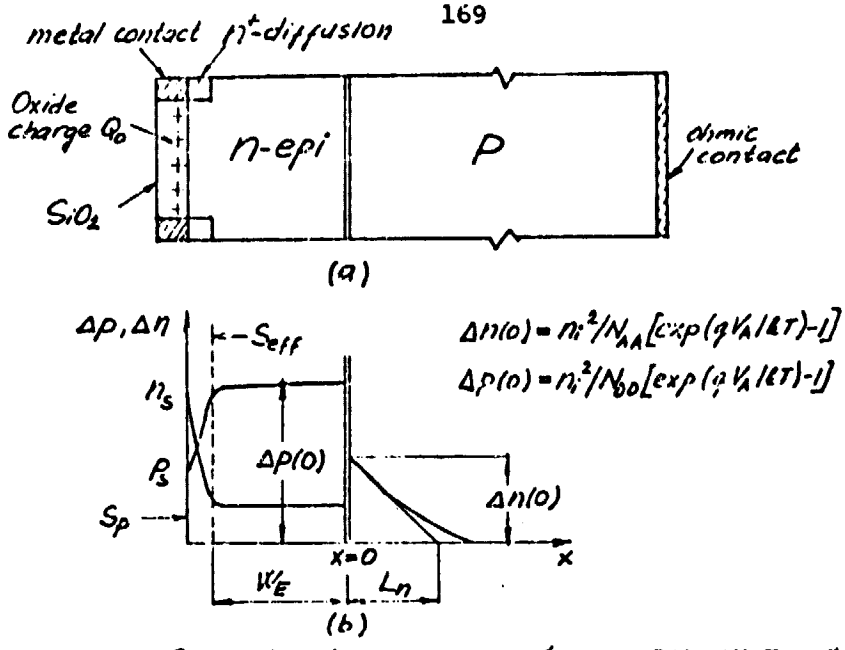

Fig. 1. (a) Schematic diagram of a n^+-n-p OCI-HLE cell.
(b) Qualitative sketches of excess minority carrier distribution in dark with applied voltage V_A.

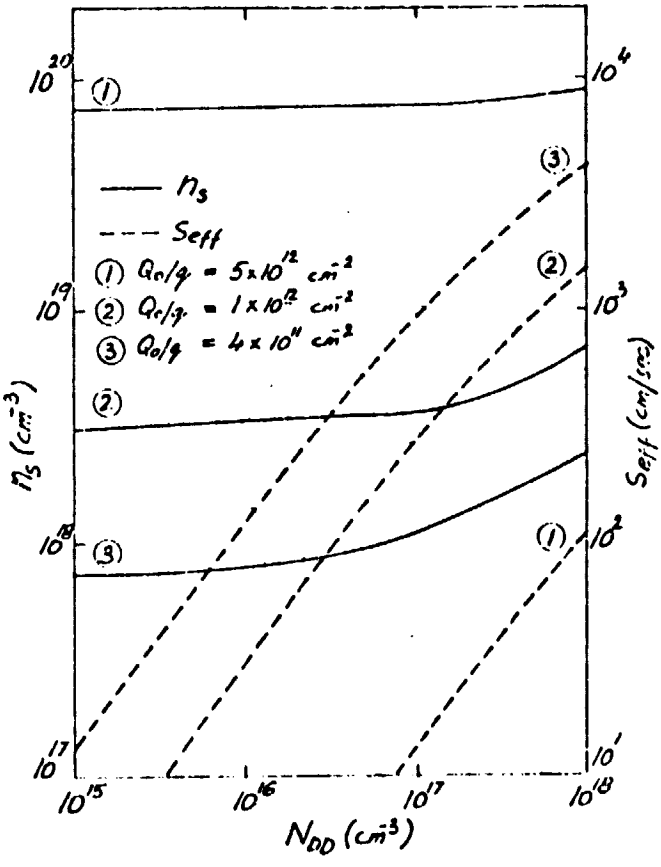

Fig. 2. Dependence of electron surface concentration n_s and effective surface recombination velocity S_{eff} (for $S_p = 10^4$ cm/sec) on emitter doping.

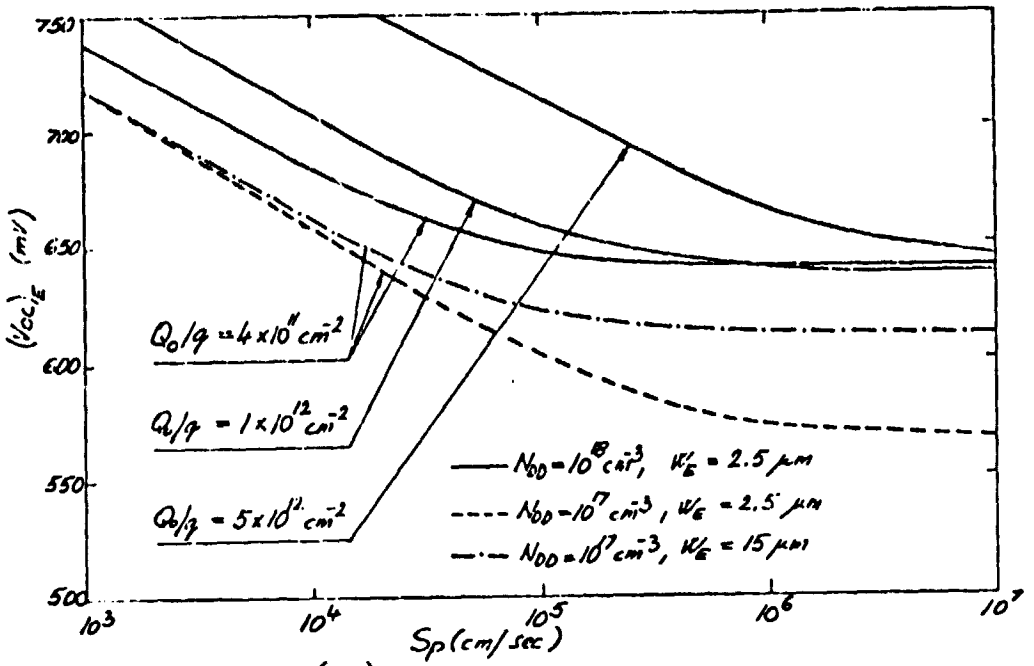

Fig. 3. Dependence of $(V_{OC})_E$ on Sp.

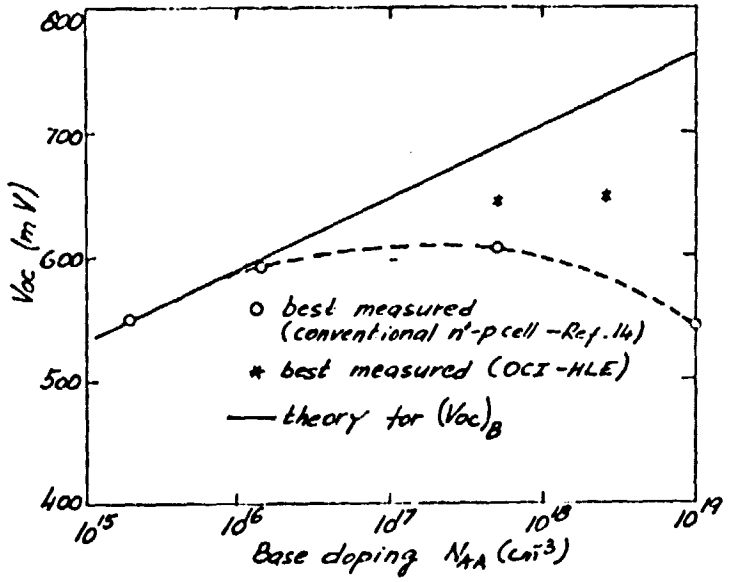

Fig. 4. Experimental and theoretical dependence of V_{OC} on base doping. Best results obtained on OCI-HLE cells are 643 mV for 0.1 Ωcm base resistivity and 647 mV for 0.024 Ωcm base resistivity (measured at NASA Lewis, at 25°C, AMO).

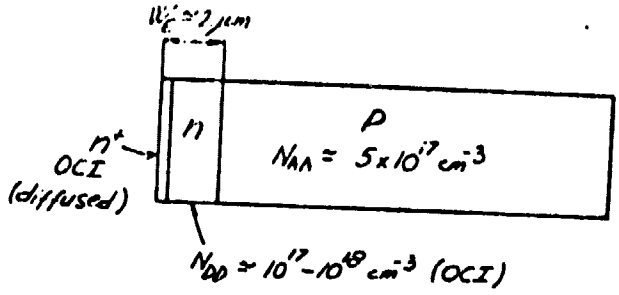

Fig. 5. Schematic diagram of a n^+-n-p OCI-HLE (diffused HLE) space cell.

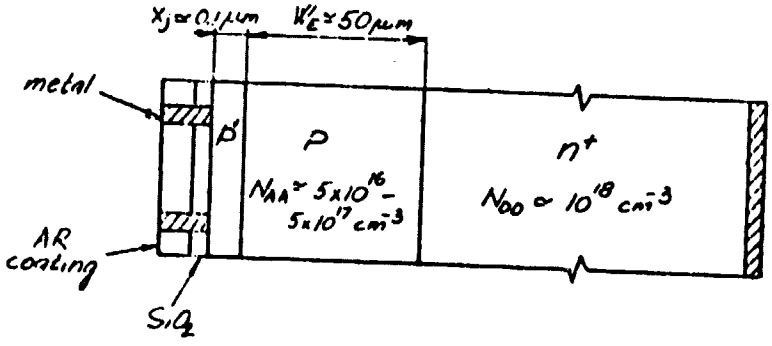

Fig. 6. Schematic diagram of a p^+-p-n^+ space cell.

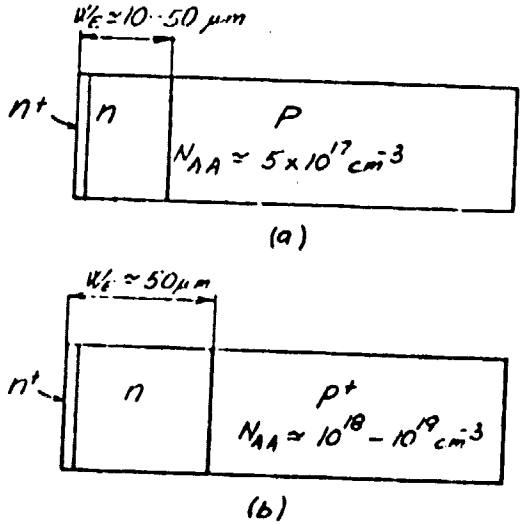

Fig. 7. Schematic diagrams of an OCI-HLE terrestrial cells.
(a) n^+-n-p cell
(b) n^+-n-p^+ cell

CHAPTER 8

SUMMARY

The project "Studies of silicon p-n junction solar cells", sponsored by NASA Lewis Research Center started in June 1974 and ran through December 1979. The project produced two M. S. Theses and three Ph.D. Theses. It also yielded 15 journal papers and 12 conference presentations. All this would have been impossible without the close cooperation of H. W. Brandhorst, Jr., and M. P. Godlewski (Technical Monitor) of NASA Lewis. We also profited from interactions with other NASA Lewis people including C. A. Baraona, D. T. Bernatowicz, R. E. Hart, Jr., C. K. Swartz, and I. Weinberg.

This report summarizes our progress during the period of September 1977 - September 1979. It contains the most significant results of both theoretical and experimental studies done in this period, as follows:

(a) Development and fabrication of an OCI-HLE cell yielding reproducibly V_{OC} = 647 mV (AM0, 25°C), which is the largest V_{OC} observed at NASA Lewis in Si p-n junction solar cells up to date.

(b) Determination of bandgap narrowing as a function of doping density in the emitter in a range of 3×10^{19} cm^{-3} to 2×10^{20} cm^{-3}.

(c) Development and demonstration of methods for measuring very long diffusion lengths (~500 μm) in solar cells and associated

dark recombination currents.

(d) Development of a comprehensive analytic theory for the limit placed on V_{OC} by a heavily-doped emitter region subject to the condition that most minority carriers in the forward-biased nonilluminated emitter recombine at the surface rather than in the bulk.